

Incom NIH SBIR 2024 Support Slides

Bill Worstell

PicoRad->MGH->Incom

6/27/2024

Project Summary

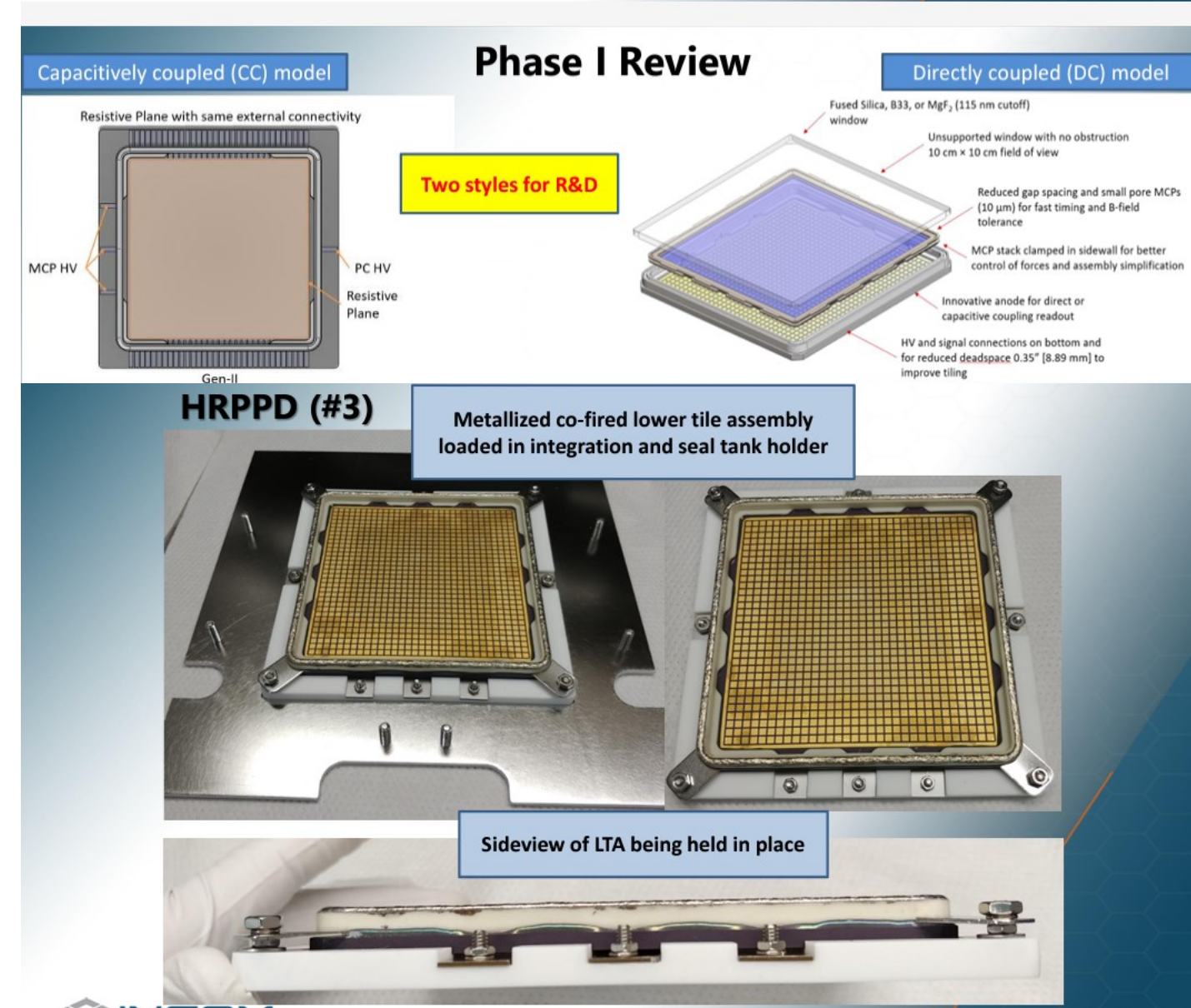
We propose developing a novel, cost-effective Time-of-Flight Positron Emission Tomography (TOF-PET) detector integrating a BGO scintillator with a directly deposited photocathode within a High-Resolution/Rate Picosecond Photon Detector (HRPPD) assembly featuring very small microcapillary arrays for extremely high time resolution. This innovative approach aims to enhance the performance and reduce the costs associated with Total Body TOF-PET systems.

Specific Aims

- 1. Design and Fabrication of the TOF-PET Detector:** Develop and fabricate a TOF-PET detector integrating a monolithic BGO scintillator block with a directly deposited bialkali photocathode inside an HRPPD assembly.
- 2. Optimization of Cherenkov Signal Coupling:** Maximize the Cherenkov signal optical coupling yield and optimize the temporal modulation transfer function for optics using specular reflectors on the far surfaces of the BGO block to enhance the detection efficiency, precision timing, and event positioning accuracy.
- 3. Preliminary Studies and Testing:** Conduct preliminary studies at Incom using a monolithic BGO block provided by MGH and a photocathode applied and tested at Incom to evaluate the performance and validate the design principles.

https://science.osti.gov/-/media/np/pdf/sbir-sttr/SBIR-STTR-2022/day-1/Foley_2022-08-23_Phase_II_Year_One_HRPPD_Development.pdf

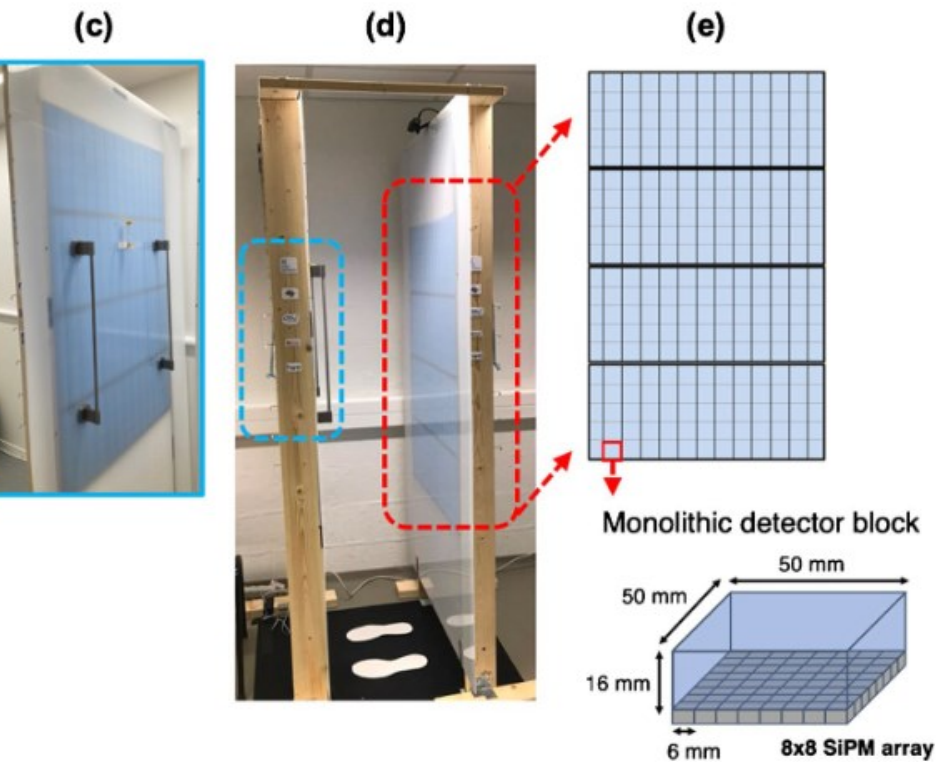
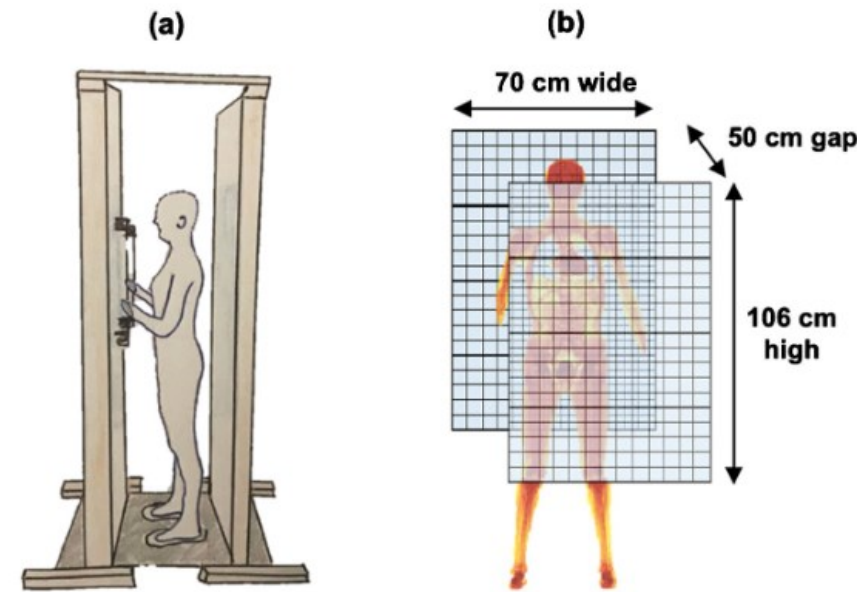
Phase I Review



Background and Significance

Total Body TOF-PET systems have demonstrated significant technical advantages due to their exceptionally high sensitivity. However, their widespread adoption has been limited by the high costs of scintillators, photodetectors, and data acquisition electronics [1]. BGO is a cost-effective scintillator for TOF-PET applications, with the cost of BGO estimated to be about three times lower than for commonly used LYSO:Ce per unit volume, with BGO having a much lower melting temperature (thereby allowing for the use of different lower cost crucibles and requiring less energy costs) and with BGO having lower raw material costs relative to LYSO:Ce [2].

Fig. 2 (a) Artist view of the walk-through TB-PET. (b) Flat panel dimensions and design. (c) One side of the mock-up with the handlebars installed to reduce the body motion. (d) Side view of the WT-TB-PET mock-up used for patient throughput measurements. Prints of feet are used to let the patient position themselves between the flat panels. (e) The four blue modules on each panel side can manually be adjusted to the right height



[1] Vandenberghe, Stefaan, Florence M. Muller, Nadia Withofs, Meysam Dadgar, Jens Maebe, Boris Vervenne, Maya Abi Akl et al. "[Walk-through flat panel total-body PET: a patient-centered design for high throughput imaging at lower cost using DOI-capable high-resolution monolithic detectors.](#)" *European journal of nuclear medicine and molecular imaging* 50, no. 12 (2023): 3558–3571.

[2] Gundacker, S., Borghi, G., Cherry, S.R., Gola, A., Lee, D., Merzi, S., Penna, M., Schulz, V. and Kwon, S.I., 2023. [On timing-optimized SiPMs for Cherenkov detection to boost low cost time-of-flight PET](#). *Physics in Medicine & Biology*, 68(16), p.165016.

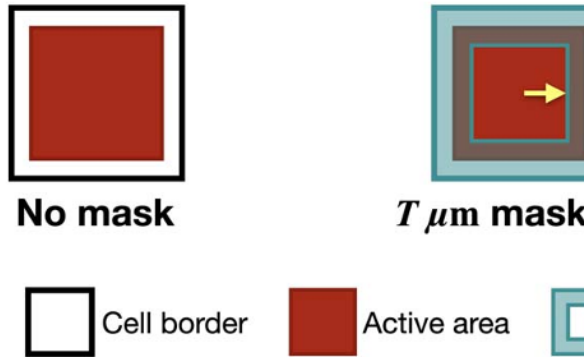


Figure 2. Illustration of the SPADs (cells) with no mask (left) and masking (right) with an overlap of $T \mu\text{m}$ thickness. The SPAD pitch is $40 \mu\text{m}$ and the SiPMs have an active area of $3 \times 3 \text{ mm}^2$.

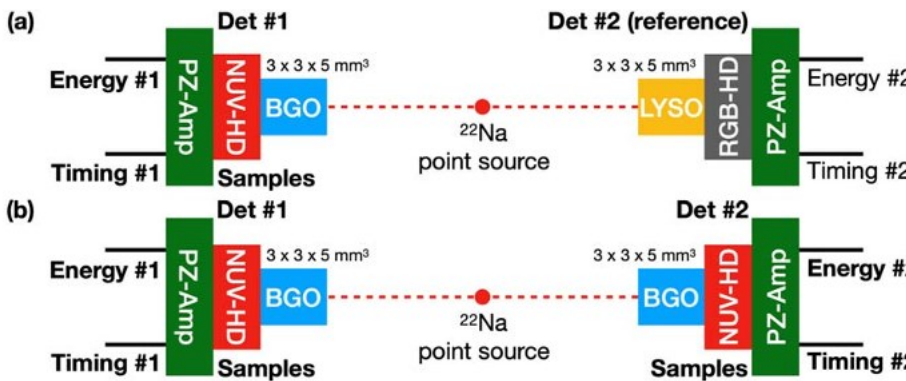


Figure 3. Experimental setup for (a) characterizing different SiPMs and (b) measuring CTR between two selected SiPMs coupled to BGO.

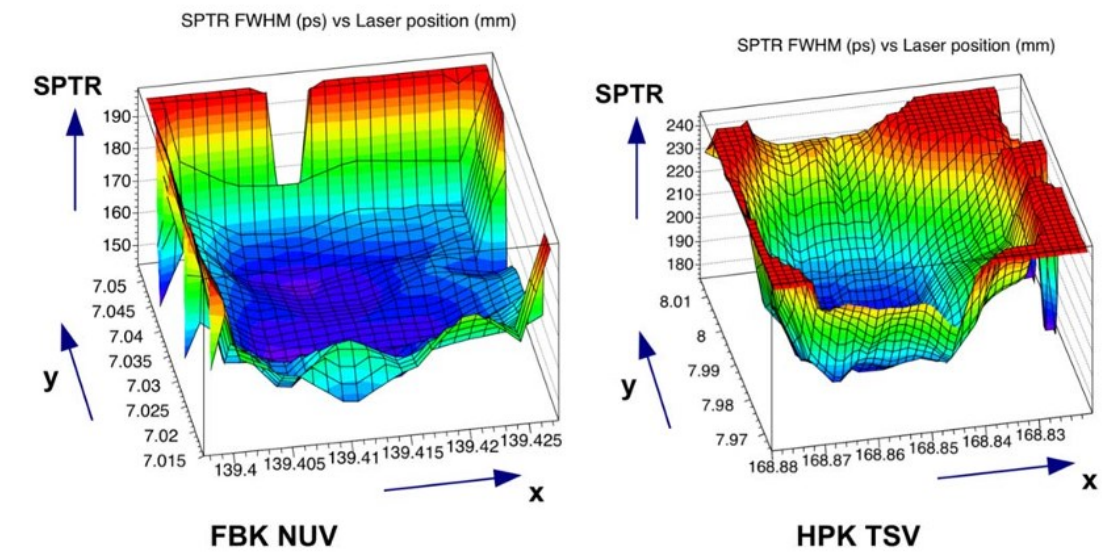


Figure 1. S PTR measured with a focused laser beam ($\sim 1 \mu\text{m}$), reveals worse S PTR at the edges of the single photon avalanche diode

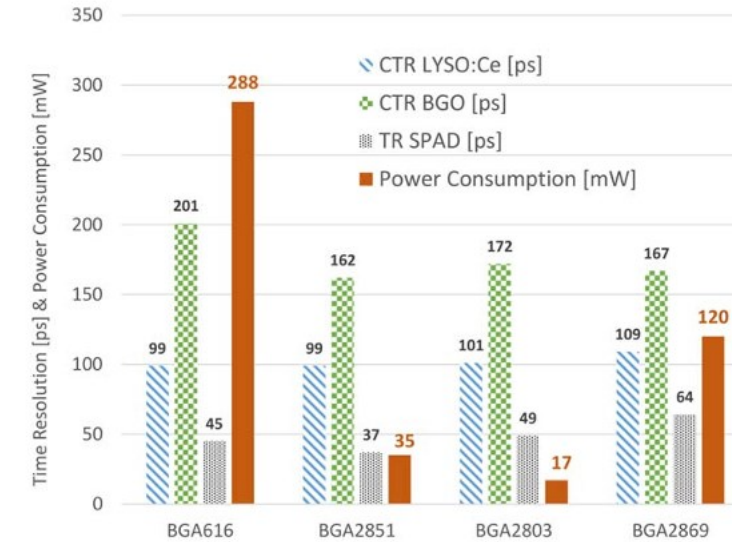


Figure 4. Overview of the CTR achieved with LYSO:Ce ($3 \times 3 \times 3 \text{ mm}^3$) and BGO ($2 \times 2 \times 3 \text{ mm}^3$) with the studied amplifiers (Krake *et al* 2022). Along the CTR values the electronic noise contribution to the single SPAD signals (TR_{SPAD}) and the power consumption per amplifier are given as well. The BGA616 type was already tested in literature (Gundacker *et al* 2019). The obtained CTR of 99 ps with LYSO:Ce compares well to literature values of 106 ps using similar crystals and SiPMs (Gundacker and Heering 2020). The SiPMs used for the TR_{SPAD} measurements and with LYSO:Ce were from Hamamatsu (HPK) type S14160-3050HS ($3 \times 3 \text{ mm}^2$ active area and $50 \mu\text{m}$ SPAD pitch), whereas BGO measurements were performed with Broadcom SiPMs AFBR-S4N33C013 ($3 \times 3 \text{ mm}^2$ active area and $30 \mu\text{m}$ SPADs).

[3] Kwon, S.I., Roncali, E., Gola, A., Paternoster, G., Piemonte, C. and Cherry, S.R., 2019. [Dual-ended readout of bismuth germanate to improve timing resolution in time-of-flight PET](#). *Physics in Medicine & Biology*, 64(10), p.105007.

[2] Gundacker, S., Borghi, G., Cherry, S.R., Gola, A., Lee, D., Merzi, S., Penna, M., Schulz, V. and Kwon, S.I., 2023. [On timing-optimized SiPMs for Cherenkov detection to boost low cost time-of-flight PET](#). *Physics in Medicine & Biology*, 68(16), p.165016.

Table 2. Overview of the best S PTR measured with black painted PbF₂ and the intrinsic S PTR, which is the measured S PTR corrected for electronic noise. The relative PDE, calculated from the geometric fill factor is given as well. Breakdown of the SiPMs are 32 V for FBK NUV-HD-CHK, 28 V for FBK NUV-HD, 26.5 V for Broadcom and 38 V for HPK. Statistical error-bars are within ± 2 ps.

SiPM	bias [V]	S PTR [ps] measured with PbF ₂	S PTR [ps] without elec. noise	relative PDE [%]
NUV-HD-CHK LF2	38	73.0	65.1	100
NUV-HD-CHK LF2 M0	38	60.7	49.9	100
NUV-HD-CHK LF2 M1	38	58.5	46.7	89.4
NUV-HD-CHK LF2 M3	38	52.3	41.9	70.3
NUV-HD-CHK LF	38	74.4	64.5	100
NUV-HD-CHK LF M0	38	65.7	56.4	100
NUV-HD-CHK LF M1	38	62.9	51.5	89.4
NUV-HD-CHK LF M3	38	53.8	42.0	70.3
NUV-HD SF	38	72.7	68.5	100
Broadcom AFBR-S4N33C013	38	69.5	65.3	-
HPK S14160-3050HS	46	127.4	125.9	-

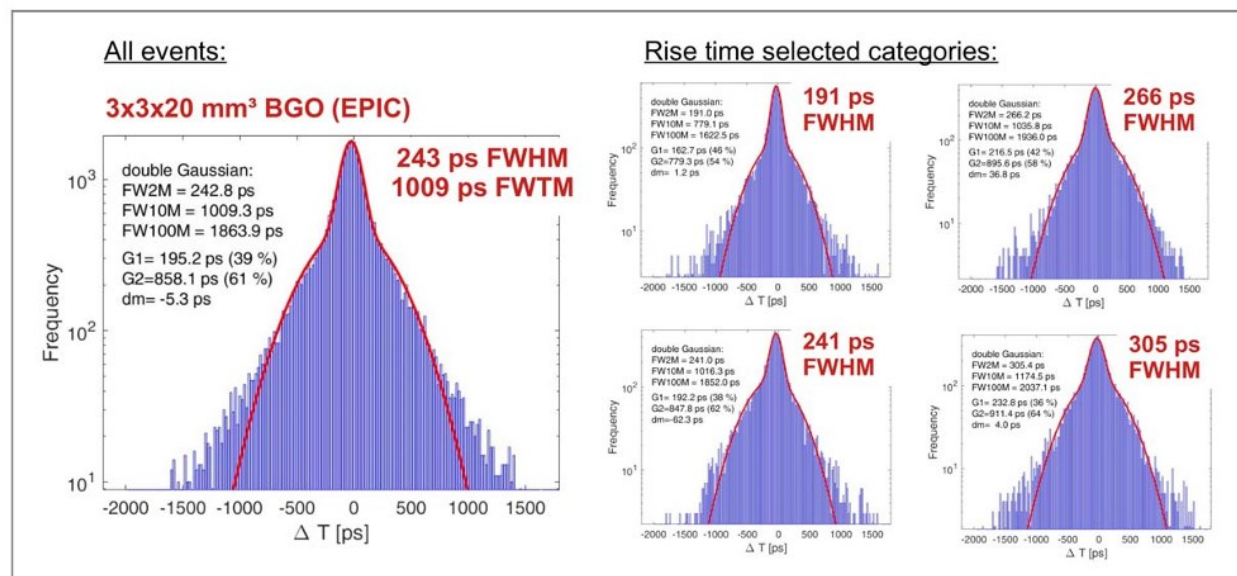


Figure 9. Coincidence time resolution measured with NUV-HD-CHK and 1 μ m masking coupled to BGO of $3 \times 3 \times 20$ mm³ size wrapped in Teflon. A CTR of 243 ps FWHM can be achieved in this configuration. If selecting to the rise times of the timing signal, the best 25% of coincident events show a CTR of 191 ps FWHM.

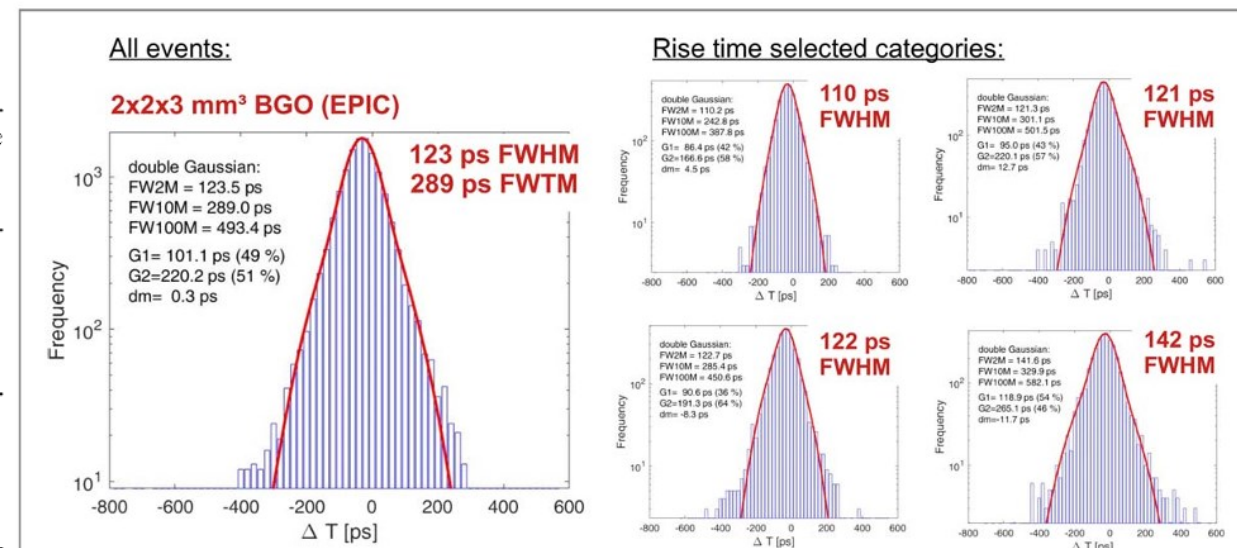


Figure 10. Coincidence time resolution measured with NUV-HD-CHK and 1 μ m masking coupled to BGO of $2 \times 2 \times 3$ mm³ size wrapped in Teflon. A CTR of 123 ps FWHM can be achieved in this configuration. If selecting to the rise times of the timing signal, the best 25% of coincident events show a CTR of 110 ps FWHM.

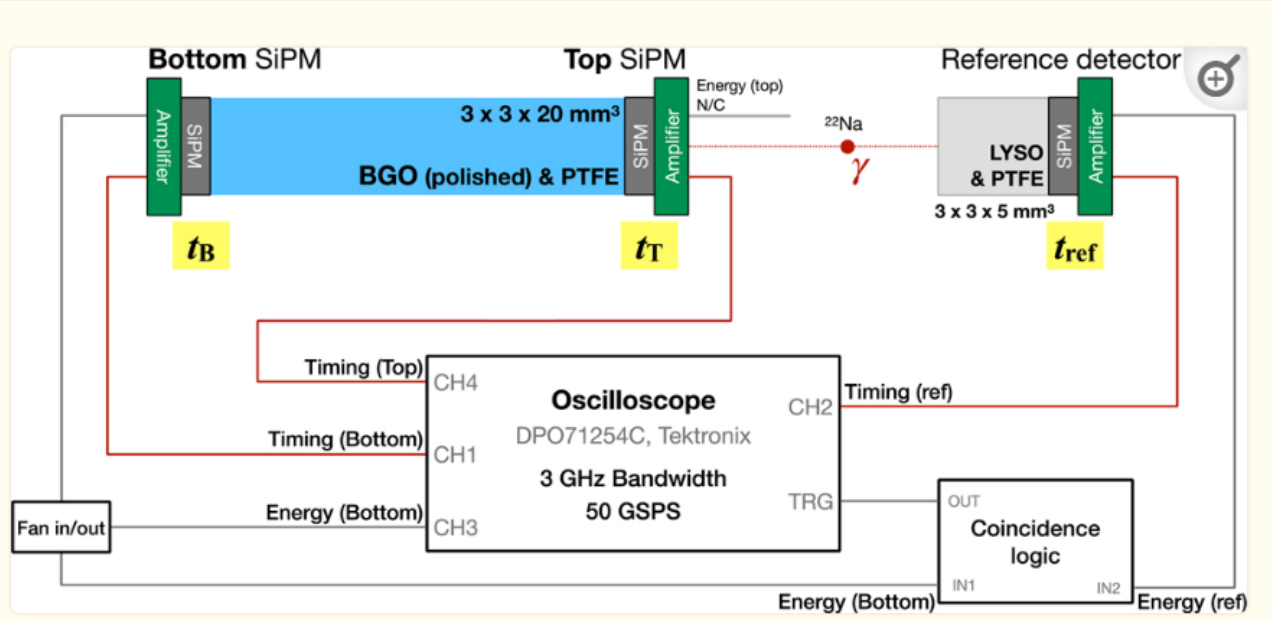


Figure 2.

Experimental setup for dual-ended readout of BGO and a reference detector.

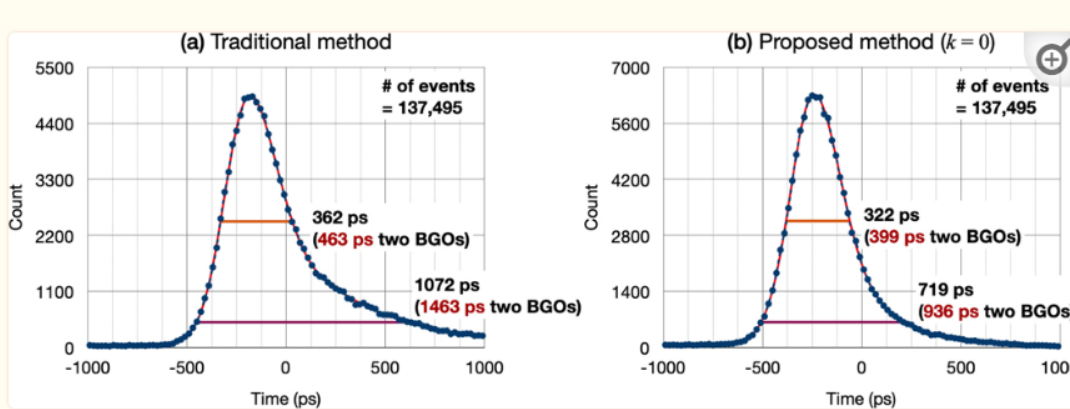


Figure 8.

FWHM and FWTM of coincidence timing spectra from experimental data using only trigger times from the bottom SiPM (a) and the proposed method ($k=0$) (b).

[3] Kwon, S.I., Roncali, E., Gola, A., Paternoster, G., Piemonte, C. and Cherry, S.R., 2019. Dual-ended readout of bismuth germanate to improve timing resolution in time-of-flight PET. *Physics in Medicine & Biology*, 64(10), p.105007.

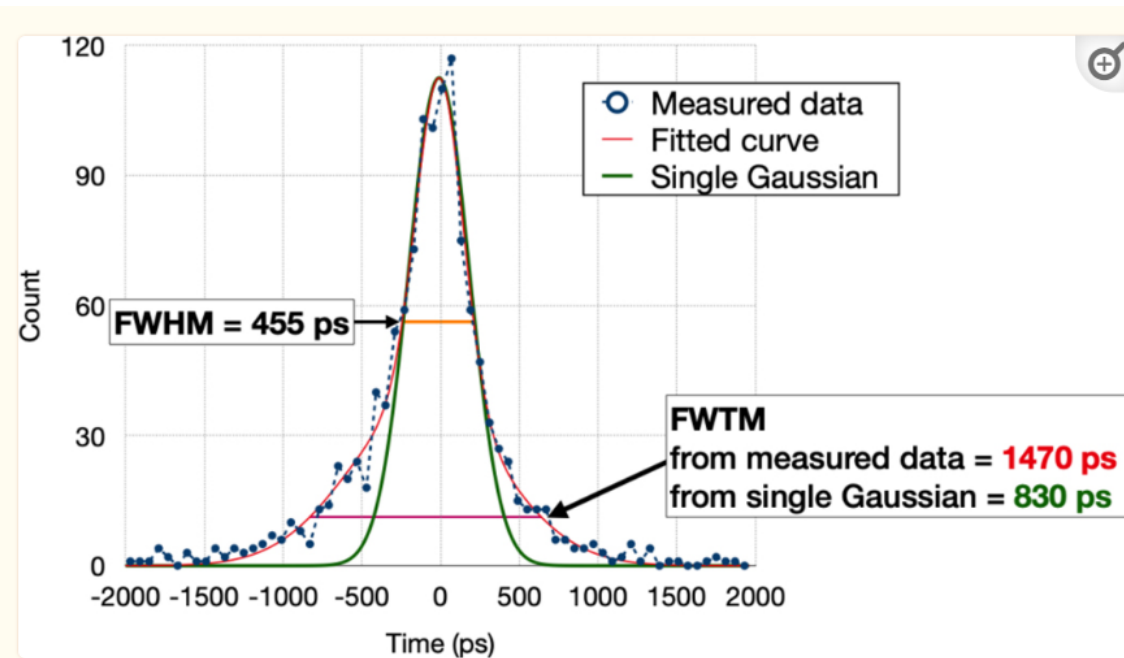


Figure 1.

Measured coincidence timing spectrum between two single-ended BGO detectors and single Gaussian fit (green). For the observed FWHM (455 ps), BGO has much larger FWTM (1470 ps) than that predicted by a single Gaussian fit (830 ps).

[4] Gonzalez-Montoro, A., Gonzalez, A.J., Pourashraf, S., Miyaoka, R.S., Bruyndonckx, P., Chinn, G., Pierce, L.A., and Levin, C.S. (2021). Evolution of PET detectors and event positioning algorithms using monolithic scintillation crystals. *IEEE Transactions on Radiation and Plasma Medical Sciences*, 5(3), pp.282-305

Current state of the art BGO TOFPET detectors mostly have used segmented scintillators, usually rectangular scintillator crystal arrays read out (sometimes on both ends) with arrays of SiPMs[3]. Recent advancements in the field have highlighted the potential of using monolithic detectors with advanced positioning algorithms to enhance the performance of PET systems by Gonzalez-Montoro et al.; this team earlier reviewed the evolution of PET detectors and event positioning algorithms, demonstrating the improvements achieved using monolithic scintillation crystals [4]. This work. developed calibration methods and algorithms for (semi-)monolithic detectors, enabling their application in clinical PET.

.

[5] González-Montoro, A., Sanchez, F., Bruyndonckx, P., Cañizares, G., Benlloch, J.M. and González, A.J., 2019. [Novel method to measure the intrinsic spatial resolution in PET detectors based on monolithic crystals](#). *Nuclear Instruments and Methods in Physics Research Section A: Accelerators, Spectrometers, Detectors and Associated Equipment*, 920, pp.58-67.

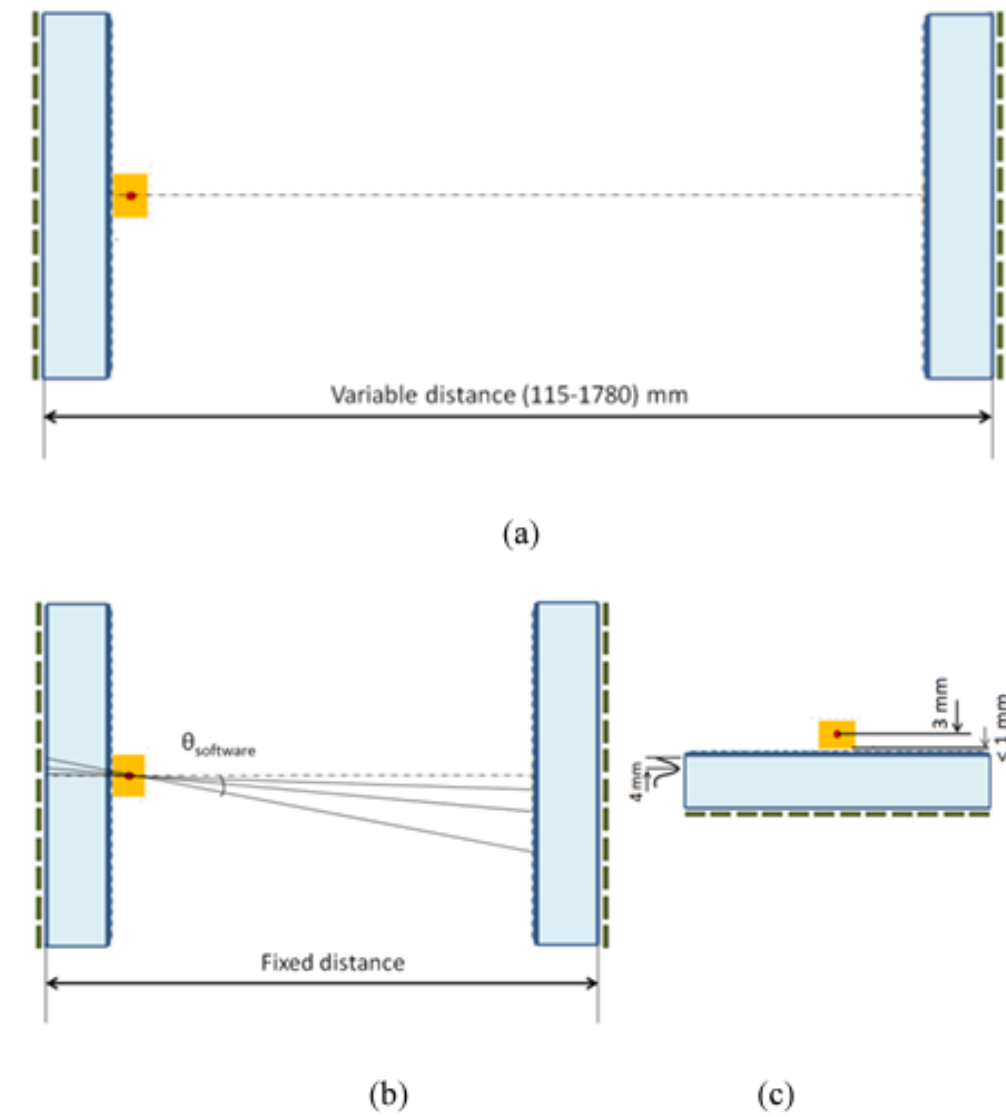


Fig. 2. Sketch of the experimental setups. Both detectors included a monolithic LYSO crystal with black painted lateral walls and were read out using an array of 16×16 SiPMs. (a) Distant detectors method showing the small size source of ^{22}Na in front of the detector under study. (b) Software Collimation method. (c) Sketch showing the distance from the source to the scintillator active volume. It is also depicted the most probable DOI, about 4 mm, in a 10 mm thick LYSO crystal.

The different detectors considered in this study all use a polished front surface (opposite of the photodetector) coupled with optical grease to a specular reflector. We test three different lateral surfaces. The first is the exact same as the front surface (polished grease ESR), which is often found in pixelated detectors to maximize internal reflection. The second is a rough surface coated with black paint (rough black) to minimize reflections. It is modeled as a rough surface coupled with a material of refractive index 1.5 to a perfectly absorbing ‘reflector’. This type of surface is often used in monolithic detectors to minimize side reflections and therefore reduce edge effects. The third lateral surface is a bare rough surface, so a rough surface coupled to air (rough bare). Finally, for the back surface we test both a rough and polished surface, both of them coupled with optical grease to the photodetector. Figure 1 shows the angular distribution of reflectance for the obtained LUTs.

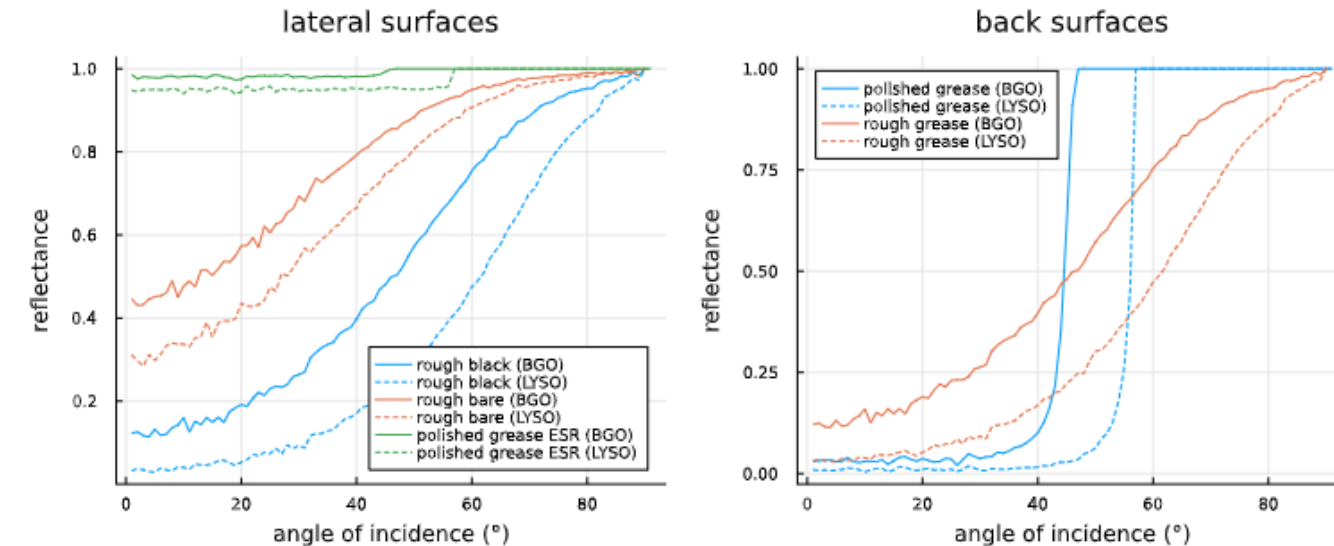


Figure 1: Angular distribution of reflectance of the surface look-up tables used throughout our simulations.

Photon detection efficiency: As shown in Figure 1, not all photons reaching the back surface will be transmitted through to the actual SiPM surface. This results in the ‘rejection’ of a certain percentage of optical photons prior to any non-idealities unique to the photodetector itself. Of those transmitted photons, only a certain percentage will actually trigger an avalanche and therefore be detected, which is determined by the photon detection efficiency (PDE) of the SiPM in question. In our simulations, we additionally take into account this (energy dependent) PDE of the SiPMs, for which we base ourselves on the Broadcom NUV-MT SiPMs (AFBR-S4N66P024M 2×1 NUV-MT Silicon Photomultiplier Array

We base ourselves on the Broadcom NUV-MT SiPMs (AFBR-S4N66P024M 2×1 NUV-MT Silicon Photomultiplier Array

Figure 2: Photon detection efficiency (PDE) wavelength dependency of Broad-om NUV-MT SiPMs and Cerenkov/scintillation spectra of BGO and LYSO.2022). These have a maximum PDE of 63% at a wavelength of 420 nm, and maintain over 40% PDE down to 300 nm. This makes them a good choice forCerenkov photon detection, given that the Cerenkov emission spectrum scales with $1/\lambda^2$ and is therefore concentrated at lower wavelengths. Figure 2 shows the PDE overlaid with the Cerenkov and scintillation spectra of BGO and LYSO.

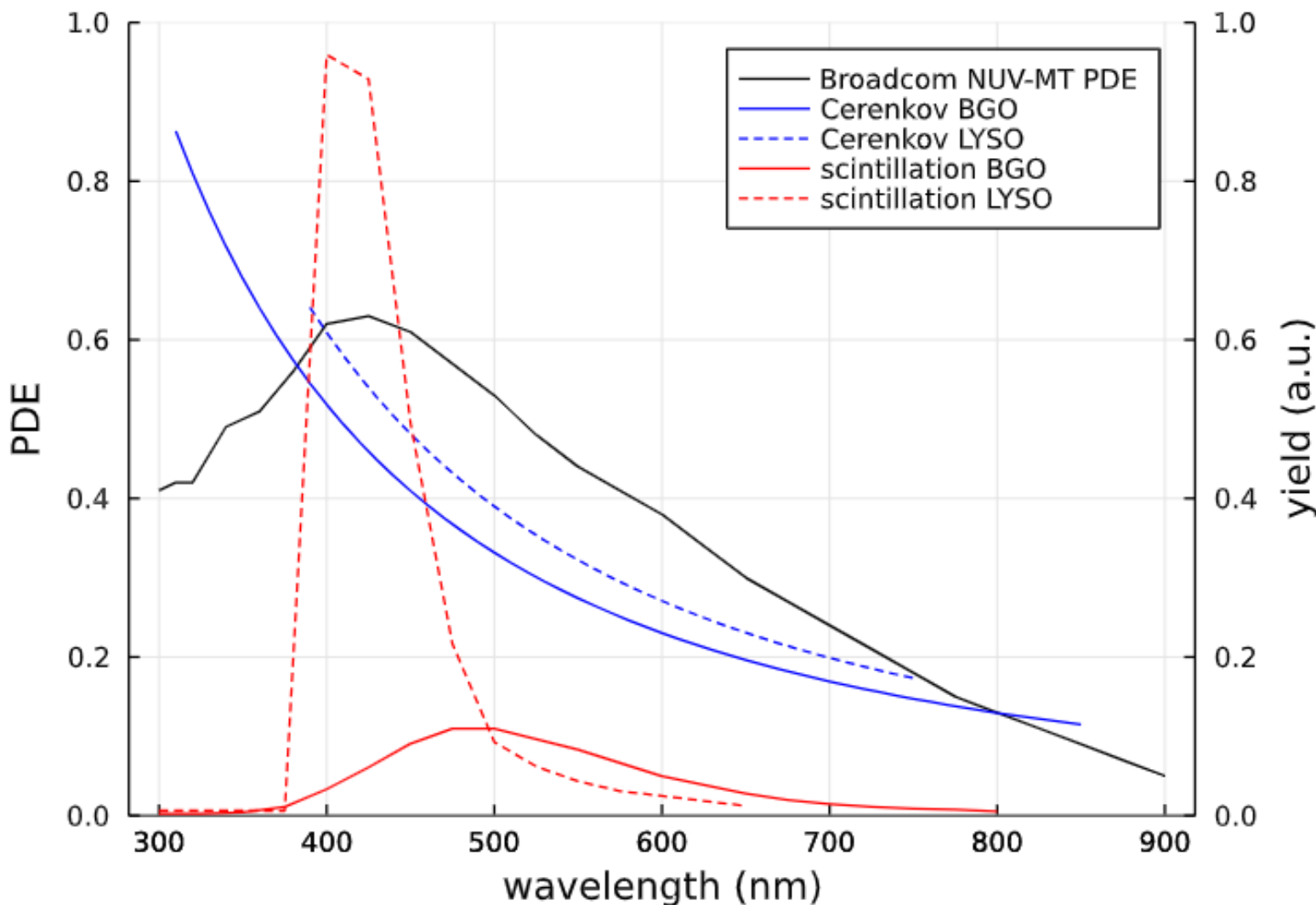


Figure 2: Photon detection efficiency (PDE) wavelength dependency of Broad-com NUV-MT SiPMs and Cerenkov/scintillation spectra of BGO and LYSO.

Maebe, J., and Vandenberghe, S. (2023). [Effect of detector geometry and surface finish on Cerenkov based time estimation in monolithic BGO detectors](#). Physics in Medicine & Biology, 68(2), p.025009...

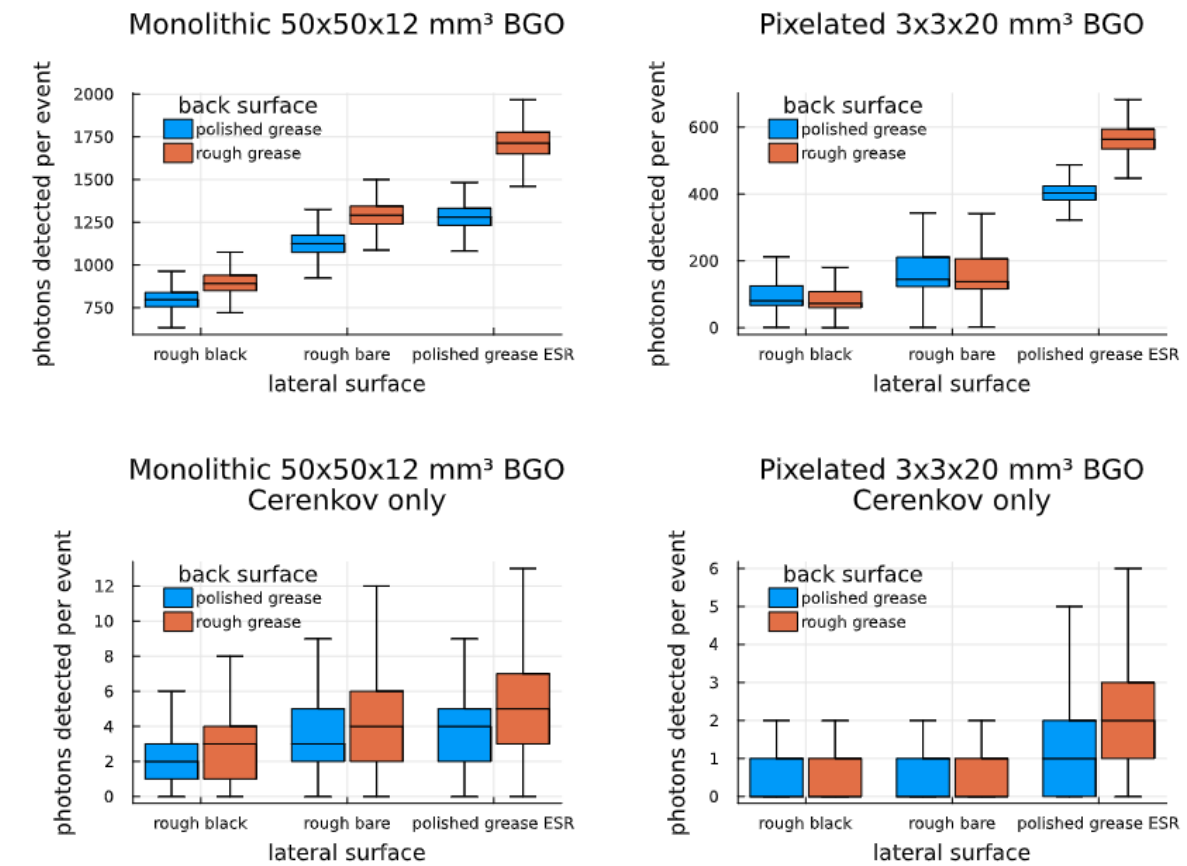


Figure 3: Comparison of photon collection efficiency for different surface finishes in monolithic and pixelated BGO detectors. The top row consider boths scintillation and Cerenkov photons, whereas the bottom row looks only at Cerenkov photons in BGO.

Figure 3 shows the photon collection efficiency (optical photons detected per event) of BGO and LYSO for two detector geometries, 50x50x12 mm³ monolithic and 3x3x20 mm³ pixelated, with different lateral and back surface finishes. Only events with full (511 keV) energy deposit in the crystal are considered, including both scatter + photoelectric and purely photoelectric events. Note that the PDE of the SiPMs is already included in these results. As was observed in Figure 1, a rough back surface allows detection of more high incidence angle photons, at the cost of reduced transmission at lower incidence angles. Since scintillation photons are emitted isotropically in 3 dimensions, the angular distribution relative to the photodetector surface normal is proportional to the radius of the corresponding circle on the unit sphere. This results in more emission of high incidence angle photons. For monolithic detectors, or when using reflective side surfaces, the rough back surface results in a net gain of photon collection efficiency since many of these high angle photons do in fact make it all the way to the photodetector surface. For the monolithic BGO detector with reflective side surfaces, the rough back surface leads to a 34% increase in photon collection efficiency compared to a polished back surface. We also observe that the differences are larger in BGO than in LYSO, since the higher index of refraction of BGO (2.15 compared to 1.82 for LYSO) leads to a larger mismatch with the optical grease.

Maebe, J., and Vandenberghe, S. (2023). [Effect of detector geometry and surface finish on Cerenkov based time estimation in monolithic BGO detectors](#). Physics in Medicine & Biology, 68(2), p.025009...

Figure 4 shows the same results but for different monolithic BGO detector sizes. The overall trends remain the same, with the larger and thinner detectors generally showing higher photon collection efficiencies. For these detectors, there is a smaller probability of losing photons to the lateral surfaces

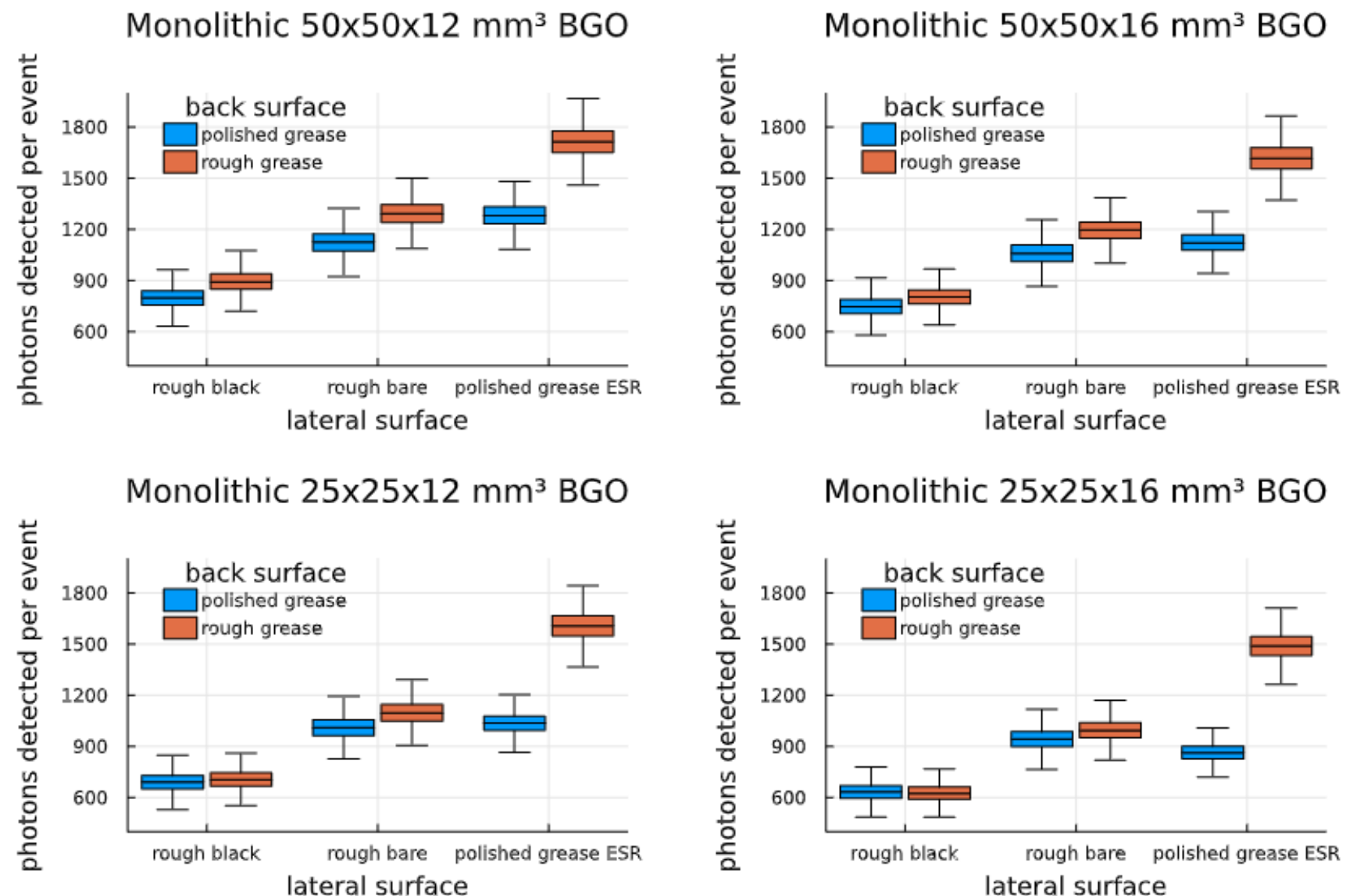


Figure 4: Effect of surface finish on photon collection efficiency in different monolithic BGO detector sizes.

In Figure 5 we take a look at the photon detection delays, which is the time between the gamma photon passing through the front surface of the detector and the detection of the n-th optical photon. A higher photon collection efficiency generally results in earlier photon detections. This is most obvious for the pixelated detectors, which overall had the lowest photon collection efficiencies. On the other hand, when there were many photons detected to begin with, as is the case for monolithic LYSO, further enhancing the photon collection efficiency has little to no effect. The absolute values of the photon detection delays however do not have any direct impact on the coincidence time resolution (CTR), since these cancel out for two identical detectors in coincidence. More important is the spread on the detection delays, especially in those cases where we rely on single photon detection per SiPM, as is the case for monolithic BGO. We see here that the rough back surface results in earlier photon detections with less variation, with the best results being obtained when combined with reflective lateral surfaces. How fast the photons are coming in one after another (i.e. the slope in Figure 5) may also have an effect on the CTR. This is primarily relevant when there are sufficient detections per SiPM for the signals to quickly pile up (e.g. for pixelated detectors), increasing the slope dV/dt of the SiPM signal and therefore reducing noise on the leading edge discrimination (Jarron et al., 2009).

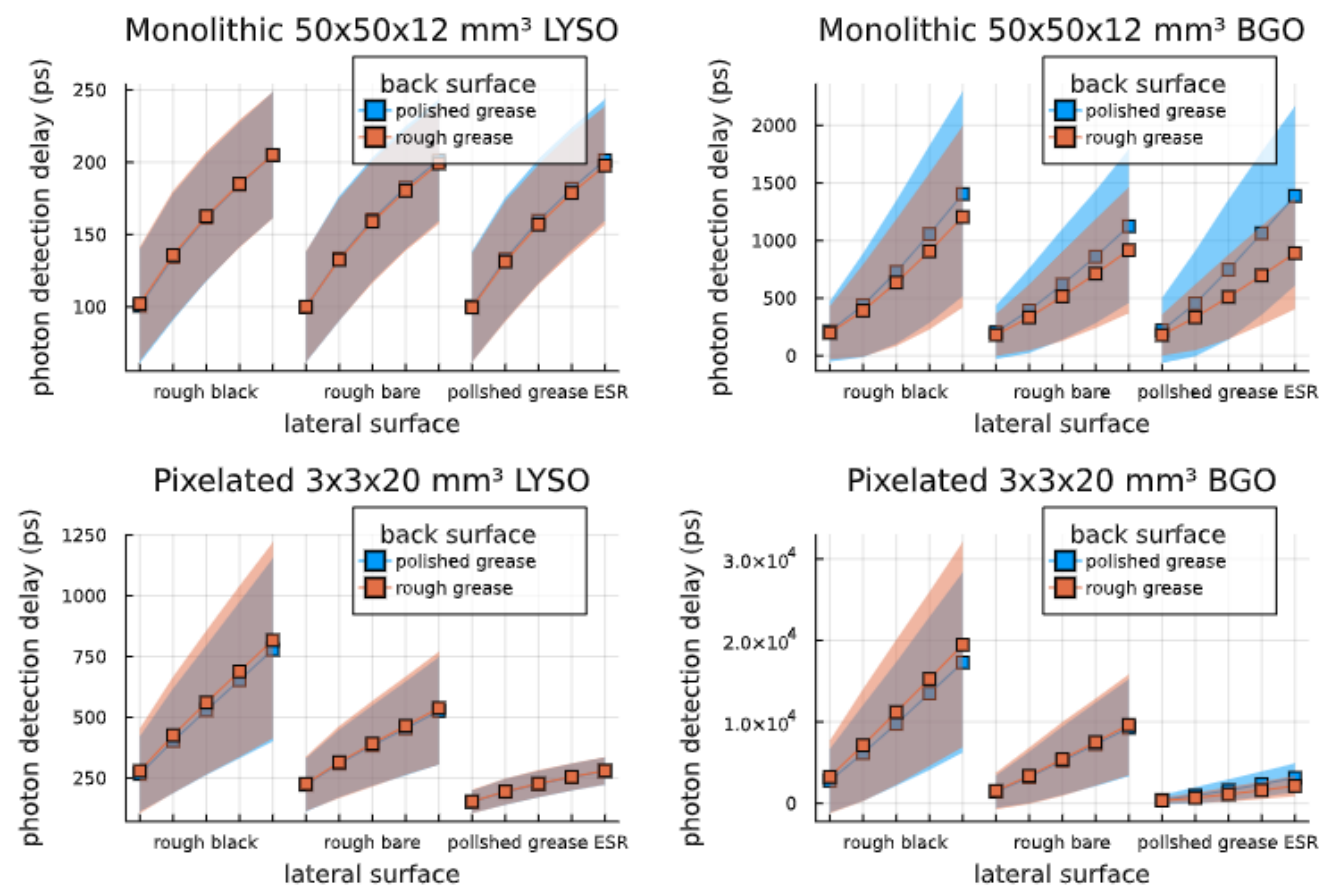


Figure 5: Time delay between the gamma photon passing through the front surface of the detector and the detection of the n-th photon (increasing left to right from $n=1$ to $n=5$). Values are averaged over all events of a specific configuration, with confidence intervals showing the standard deviation ($\pm\sigma$).

We estimate the CTR of the monolithic detectors by simulating the SiPM signals and predicting the gamma arrival time based on leading edge discrimination. For the $50 \times 50 \text{ mm}^2$ detectors we use an 8×8 readout of $6 \times 6 \text{ mm}^2$ SiPMs, and for the $25 \times 25 \text{ mm}^2$ detectors a 4×4 readout of the same $6 \times 6 \text{ mm}^2$ SiPMs. Leading edge discrimination is performed on each individual SiPM waveform, resulting in a matrix of 8×8 or 4×4 timestamps. We use a leading edge discrimination threshold of 0.5 photoelectron pulse amplitudes in order to detect individual Cerenkov photons. **Due to the presence of dark counts, the signal amplitude prior to gamma detection is not necessarily centered around 0 and may even be above the 0.5 photoelectron threshold level. This leads to a fraction of the SiPMs recently having triggered prior to the actual gamma event, resulting in 'dead' SiPMs incapable of triggering again for a certain time.** We therefore lose the timing information of those SiPMs. In our simulations this limitation was modelled by considering those SiPMs with a signal amplitude > 0.25 photoelectrons prior to the gamma event as dead, and therefore not being present in the time stamp matrix. The gamma arrival time itself was then predicted as the first SiPM time stamp. Averaging of the first few timestamps was also tested, but consistently underperformed for monolithic BGO.

The TOF kernels are constructed by randomly subtracting different events from one another (to obtain events in coincidence), after which a kernel density estimation fit is performed to obtain a distribution from the TOF histogram. Figure 6 shows such a TOF kernel for a case with long tails (monolithic $50 \times 50 \times 16 \text{ mm}^3$ BGO with rough black sides and a polished detector surface). The kernel density estimation fit is compared to a Gaussian with the same FWHM, showing the non-Gaussian nature of the TOF kernel.

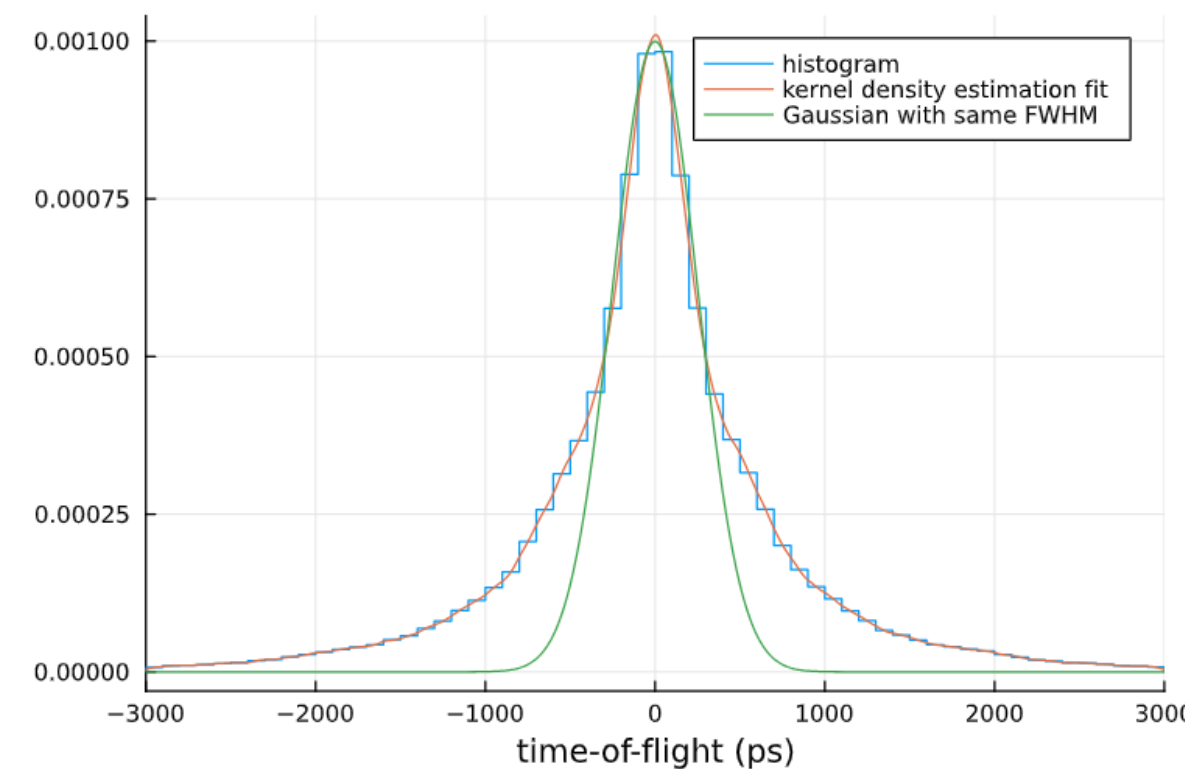


Figure 6: Time-of-flight kernel of monolithic $50 \times 50 \times 16 \text{ mm}^3$ BGO with rough black sides and a polished detector surface. The kernel density estimation fit, which accurately describes the time-of-flight histogram, is compared to a Gaussian kernel with the same FWHM, showing the extent of the tails.

Figure 7 shows the coincidence time resolutions for the different monolithic detector configurations. Here we have used a leading edge discrimination thresh-old of 0.5 photoelectron pulse amplitudes. Since the distributions are not perfectly Gaussian, we report the full width at half maximum (FWHM/FW2M),full width at tenth maximum (FWTM/FW10M) and the full width at twentieth maximum (FW20M). While the FWHM remains in the same range for the different configurations, the FW10M and FW20M show larger differences .That is, the different surface finishes mostly affect the tails of the distribution. The thinner (12 mm) crystals provide a better time resolution, with the rough back surface resulting in lower FW10Ms and FW20Ms (shorter tails), especially when using non-absorbing lateral surfaces. E.g. for monolithic $50 \times 50 \times 12 \text{ mm}^3$ BGO with reflective side surfaces, we see a reduction of 18% in FW10M going from a polished back surface to a rough back surface. Again we also see that for monolithic LYSO, the surface finish has negligible impact on the coincidence time resolution

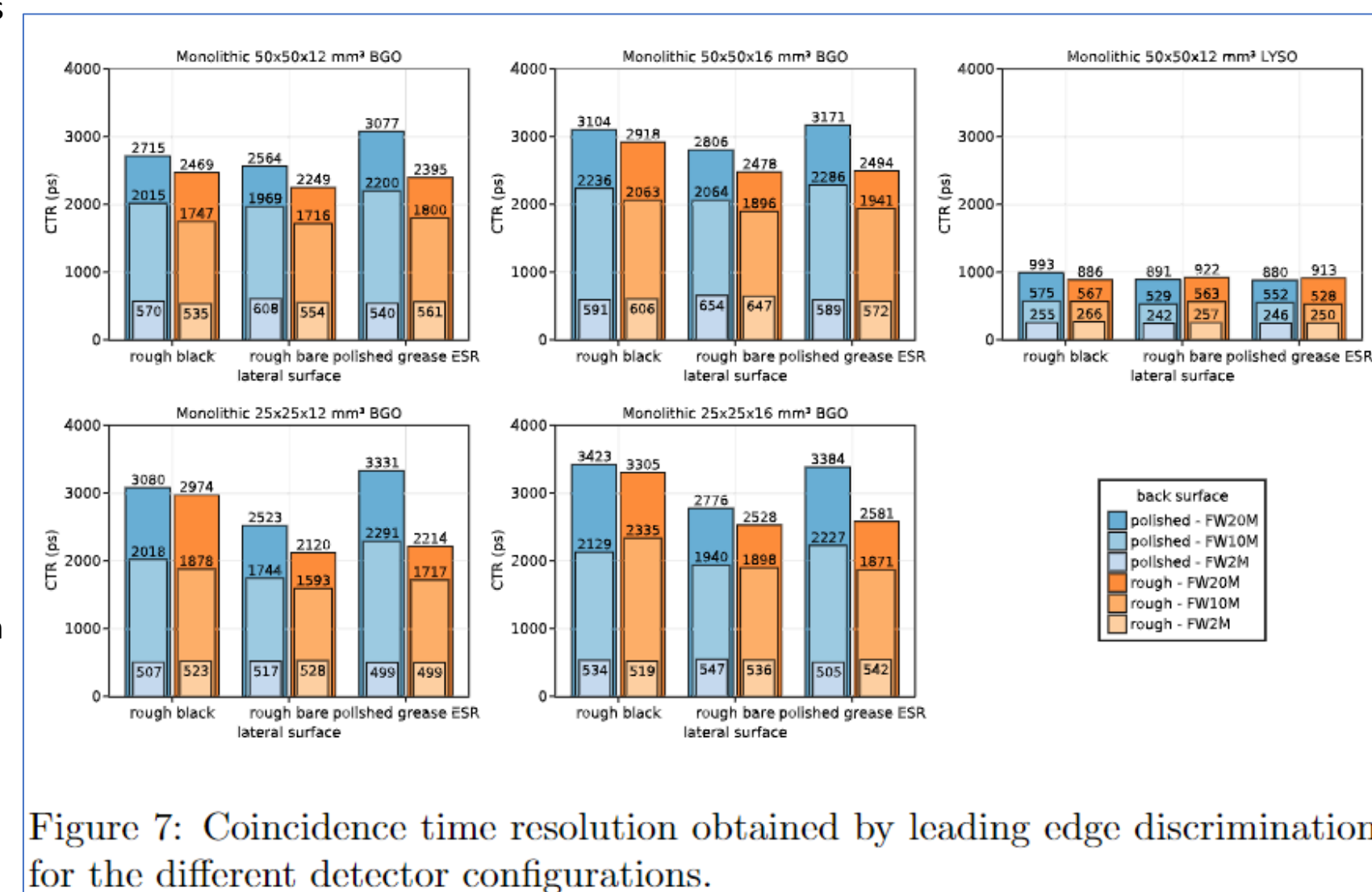


Figure 7: Coincidence time resolution obtained by leading edge discrimination for the different detector configurations.

Maebe, J., and Vandenberghe, S. (2023). [Effect of detector geometry and surface finish on Cerenkov based time estimation in monolithic BGO detectors](#). Physics in Medicine & Biology, 68(2), p.025009...

Discussion In order to benefit from Cerenkov based time estimation, it is important to use SiPMs and readout electronics that are in fact capable of resolving individual photon detections. Note that only a few Cerenkov photons are detected per event for an entire 50x50x12 mm³ monolithic BGO detector (Figure 3), over a total of 64 SiPMs. Given the large spread in Cerenkov emission angles, it is highly improbable that more than one Cerenkov photon will be detected by the same SiPM and we can therefore not rely on fast signal pile-up. Modern SiPMs can easily detect individual photons, and readout electronics have no problem detecting the leading edge of an SiPM signal below a single photoelectron level. The difficulty lies in the generation of dark counts, which can lead to missing Cerenkov photon detections or dark counts being misinterpreted as a Cerenkov photon.

4.1 Effect of dark counts In order to detect (sufficient) Cerenkov photons in monolithic detectors, it is required to set the leading edge threshold below a single photoelectron level. The SiPMs will rarely trigger on Cerenkov photons at higher thresholds, since most SiPMs detect no more than a single Cerenkov photon. While the dark count rate of a single SiPM is not that high (4.4 MHz), we are dealing with 64SiPMs for the 50x50mm² detector configurations. This means that on average, we detect a dark count every ~3.6 ns over the whole detector, which is only an order of magnitude larger than the typical coincidence time resolutions. An SiPM that is triggered by a dark count will be incapable of triggering again for a short time while the signal amplitude drops off. If a Cerenkov photon happens to be absorbed during this timeframe, it will still contribute to the SiPM signal, but no leading edge detection will trigger. These ‘dead’ SiPMs essentially equate to a loss of photon collection efficiency when it comes to timing information. In addition, while most dark count triggers can be rejected based on energy integration, measuring a dark count every ~3.6 ns means that there is a non-negligible probability that a dark count occurs just prior to the gamma event. It would therefore be indistinguishable from a Cerenkov photon, leading to a false datapoint in the timestamp matrix. Dark counts are likely less problematic in pixelated detectors, since the overall dark count rate is lower (only one SiPM per pixel) and all Cerenkov photons are detected by the same SiPM, so that a higher leading edge threshold would still be capable of detecting Cerenkov photons. This is still partially true of monolithic LYSO, where many photons reach the SiPMs sufficiently quick one after another to still obtain valuable time information using thresholds above the single photoelectron level. Therefore, further reductions in dark count generation of SiPMs, and readout electronics better capable of dealing with dark count rejection are especially important for timing in monolithic BGO

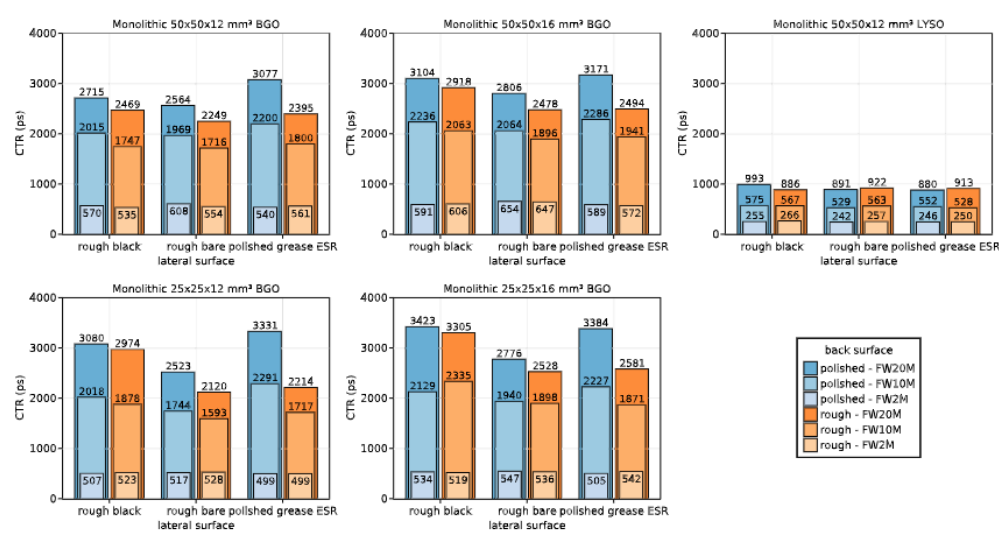


Figure 7: Coincidence time resolution obtained by leading edge discrimination for the different detector configurations.

4.2 Effect of photon collection efficiency The photon collection efficiency of the detectors plays a significant role in timing performance when relying on Cerenkov photons for time-of-flight estimation .We can appreciate this in Figure 7, consistently showing better time resolutions for the higher photon collection efficiencies. The detectors with higher photon collection efficiencies do detect more high incidence angle (for the rough backsurface) or reflected (for the reflective lateral surfaces) photons. These photons have longer (and higher variation in) photon transfer times from the gamma interaction position to the photodetector. Therefore, accurate prediction of the transfer time of an individual photon is more difficult. Nonetheless, these detectors show better overall timing statistics due to the larger amount of photon detections.

Maebe, J., and Vandenberghe, S. (2023). [Effect of detector geometry and surface finish on Cerenkov based time estimation in monolithic BGO detectors](#). Physics in Medicine & Biology, 68(2), p.025009...

Time-of-flight kernels As mentioned, the photon collection efficiency in monolithic BGO primarily has an effect on the tails of the time-of-flight kernel, showing shorter tails for high collection efficiencies. Figure 8 shows the time-of-flight kernel (as was obtained in Figure 7) for a low and high photon collection efficiency configuration of monolithic $50 \times 50 \times 16 \text{ mm}^3$ BGO: absorbing lateral sides with a polished backsurface, and reflective lateral sides with a rough back surface. The longer tails can be attributed to more events with fewer Cerenkov detections. A similar effect can be seen when comparing purely photoelectric with scattered (but still 511 keV) events, showing considerable time resolution degradation for scattered events. The effect is now no longer confined to the tails ,increasing the FWHM from 465 ps for purely photoelectric events to 817 ps for scatter + photoelectric events. This is due to a reduced emission of Cerenkov light. Simulations of the monolithic $50 \times 50 \times 16 \text{ mm}^3$ BGO detector show only 10 Cerenkov photons emitted on average per scatter + photoelectric event, compared to 18 photons for purely photoelectric events. Note that this poses less of a problem for pixelated detectors, where the majority of 511 keV events are purely photoelectric since a scattered gamma photon often exits the crystal before depositing the rest of its energy. For monolithic detectors though, scattered events will not only contribute to a degradation of spatial resolution, but also time resolution.

Maebe, J., and Vandenberghe, S. (2023). [Effect of detector geometry and surface finish on Cerenkov based time estimation in monolithic BGO detectors](#). Physics in Medicine & Biology, 68(2), p.025009...

Identification of scattered events could however allow for image reconstruction with multiple time-of-flight kernels, improving overall image signal-to-noise ratio (Efthimiou et al., 2021). Scatter identification was for example done for LYSO with a deep learning based approach using simulated data (Decuyper, Milan, 2021). The difficulty here lies in using a network trained on simulated data for experimental data. Additionally, BGO has shorter range scatters compared to LYSO, which makes them more difficult to identify. Therefore, the feasibility of such an approach would require further investigation. Another approach for time-of-flight kernel separation would be identifying events with good timing based on the SiPM signal rise time, as was previously done in pixelated BGO detectors (Kratochwil et al., 2020). This would likely require summing of the SiPM signals in monolithic detectors, since most Cerenkov photons are absorbed by different SiPMs and the signal rise time of individual SiPMs is therefore unlikely to vary much. It should nonetheless be possible to implement for monolithic detectors, providing an additional method to improve image signal to noise ratio for a given detector configuration.

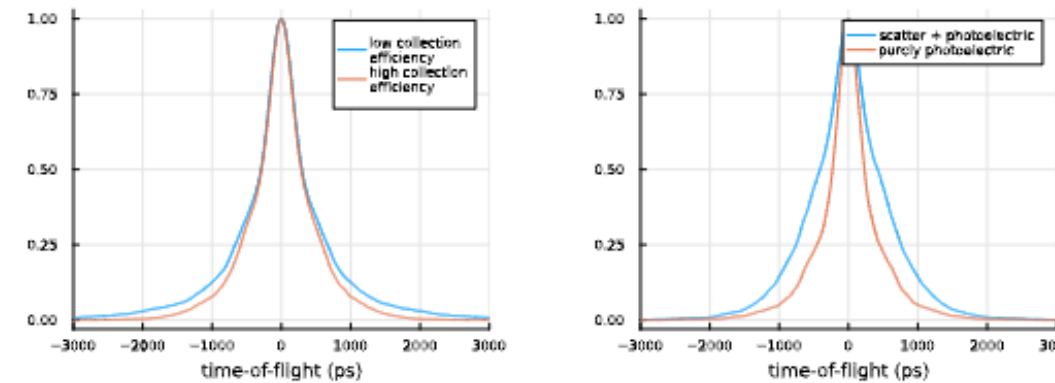


Figure 8: Time-of-flight kernels for monolithic 50x50x16 mm³ BGO. **Left:** two different surface finish configurations, one with low photon collection efficiency (rough black lateral and polished back surface) and one with high photon collection efficiency (polished reflective lateral and rough back surface). **Right:** comparison between purely photoelectric and scatter + photoelectric events for the high photon collection efficiency configuration.

This study shows the importance of optimizing the photon collection efficiency to improve Cerenkov based time estimation in monolithic BGO detectors. Multiple detector configurations were simulated for comparison, including different geometries (pixelated and monolithic), surface finishes (for the lateral and backsides) and scintillation materials (LYSO and BGO). While changing the surface finish had little effect on the time resolution in monolithic LYSO due to already high photon collection efficiencies, it plays an important role in Cerenkov based time estimation for BGO due to much lower photon statistics. Surface finishes that improve photon collection efficiency result in time-of-flight kernels with shorter tails. Commonly used surface finishes in monolithic detectors (normally optimized for spatial resolution) result in inferior time resolution, showing potential benefit in making a switch to other surface finishes that increase photon collection efficiency such as reflective sides and a rough back surface.

Yvon, D., Sharyy, V., Follin, M., Bard, J.P., Breton, D., Maalmi, J., Morel, C. and Delagnes, E., 2020. [Design study of a “scintronic” crystal targeting tens of picoseconds time resolution for gamma ray imaging: the ClearMind detector](#). *Journal of Instrumentation*, 15(07), p.P07029.

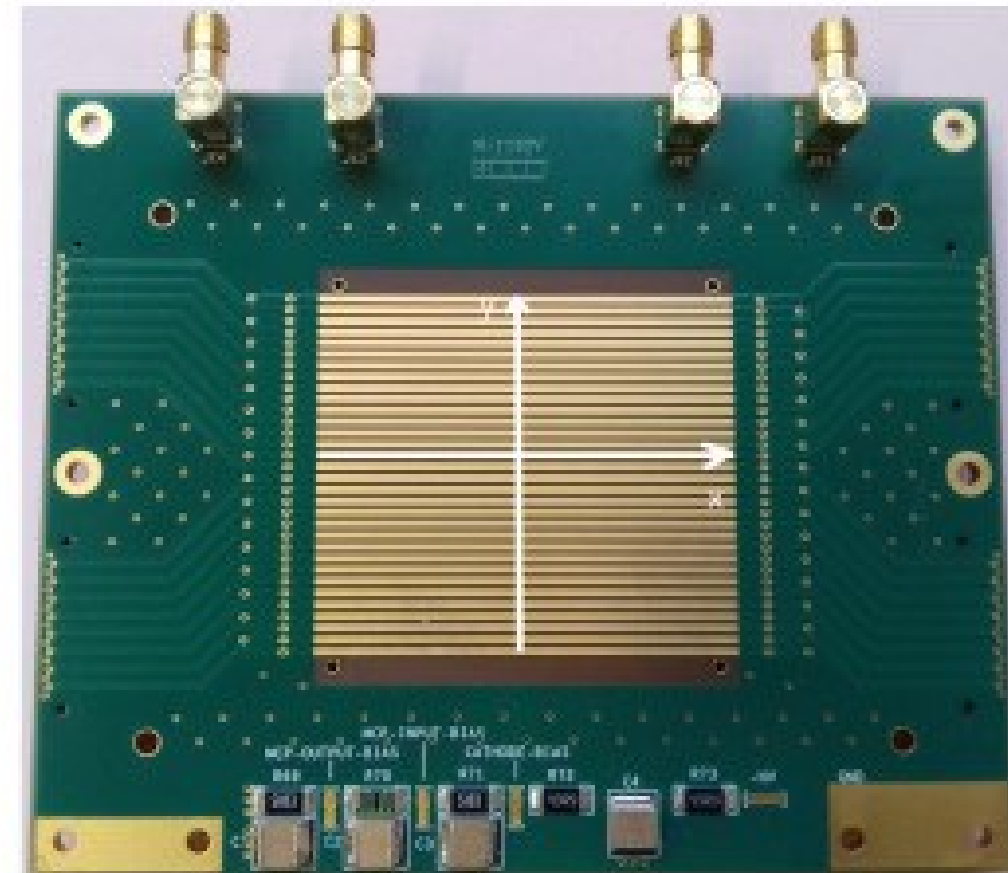
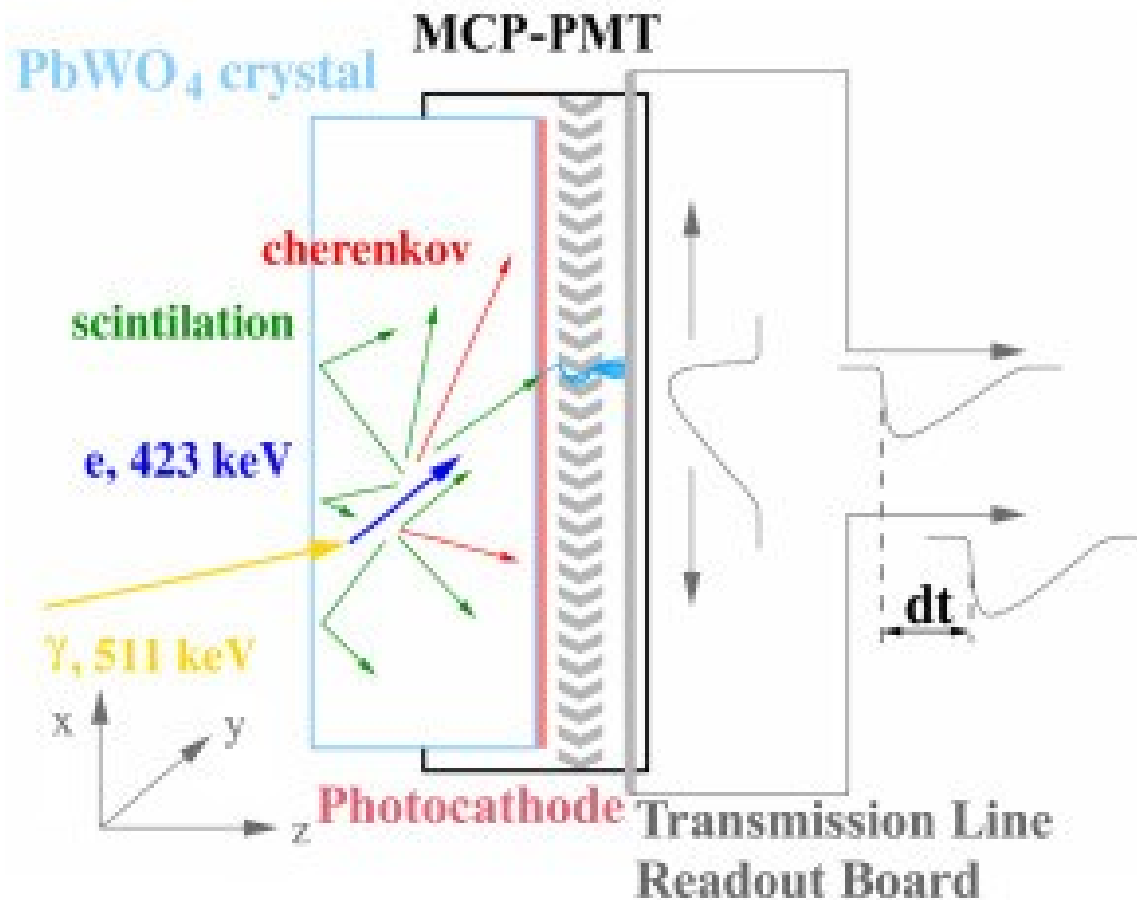


Fig. 1. **Left:** Schematic diagram of the ClearMind detection module. A 511 keV gamma-ray interaction in the crystal produces scintillation and Cherenkov photons that are converted by the [photocathode](#) to [photoelectrons](#). These photoelectrons are then multiplied by the MCP-PMT and induce signals on the transmission lines (TLs). Signals from the left and right ends of each TL are amplified by 40 dB amplifiers and digitized by a SAMPIC module. **Right:** Transmission lines [Printed Circuit Board](#) (PCB). The axis x and y corresponds to the [coordinate system](#) that we use to locate the interaction position.

Yvon, D., Sharyy, V., Follin, M., Bard, J.P., Breton, D., Maalmi, J., Morel, C. and Delagnes, E., 2020. [Design study of a “scintrinsic” crystal targeting tens of picoseconds time resolution for gamma ray imaging: the ClearMind detector](#). *Journal of Instrumentation*, 15(07), p.P07029.

SAMPIC Pulse Left

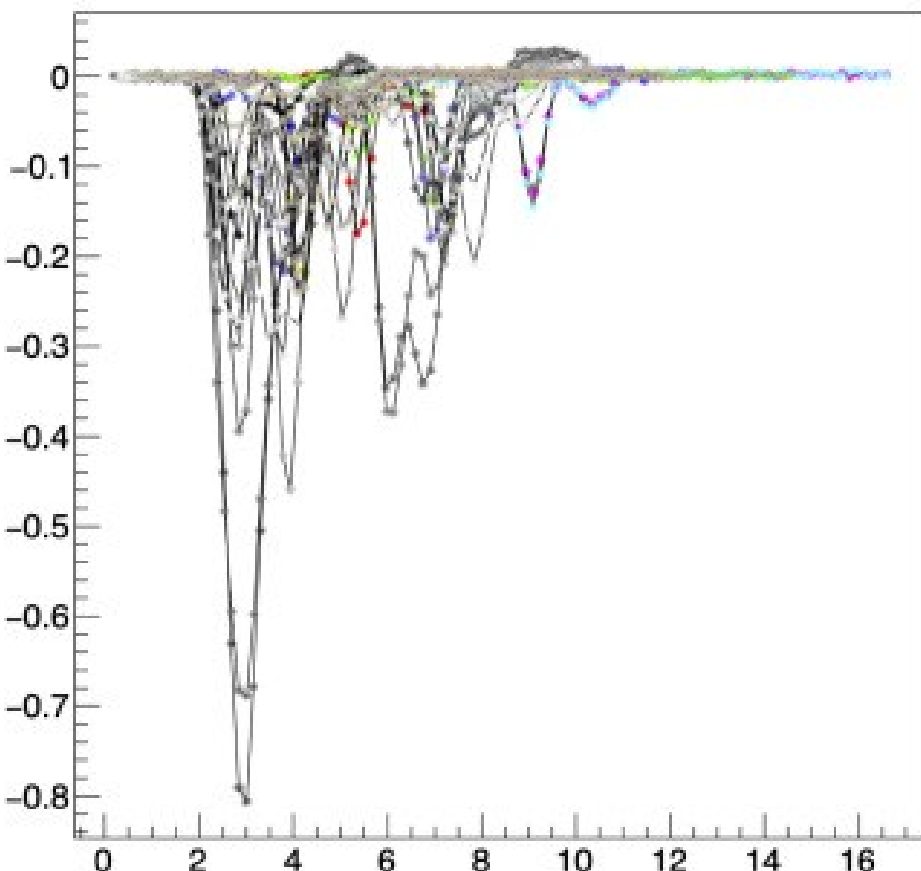


Fig. 2. Set of pulses as registered by the SAMPIC waveshape recorder for a 511 keV energy deposit. For clarity purpose, only the pulses registered on one side of the transmission lines are shown (half of the set).

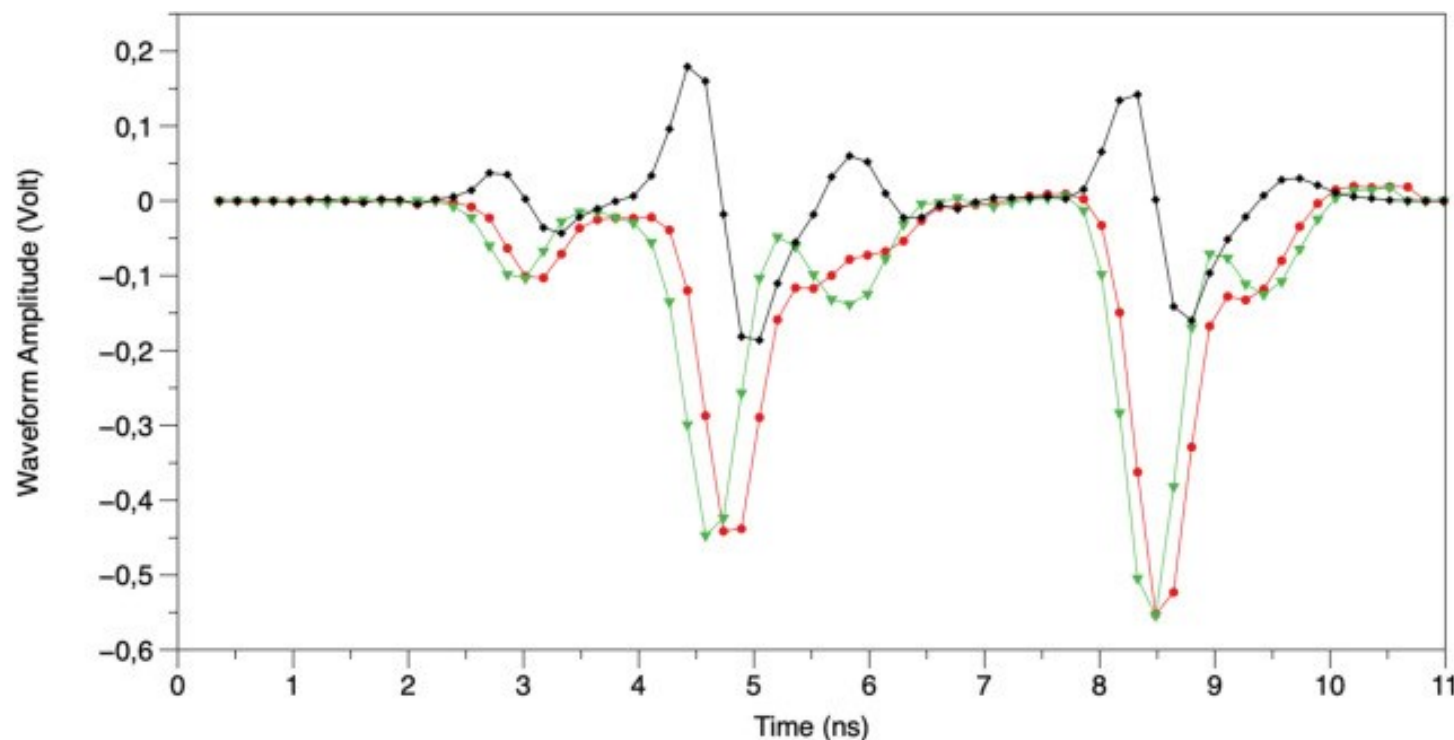


Fig. 3. Waveforms registered on one triggered line l . Red and green lines are the left $F_{l,\text{Left}}(t_j)$ and right $F_{l,\text{Right}}(t_j)$, time shifted, registered pulses shapes. Black line shows the [time difference](#) waveform $F_{l,\text{Left}}(t_j)-F_{l,\text{Right}}(t_j)$. We identify on this line three pulses clusters at 4.6 ns, 6 ns and 8.5 ns. For each of them, the time difference curve shows a bipolar shape, correlated to the position of each photoelectron charge induction along the readout line.

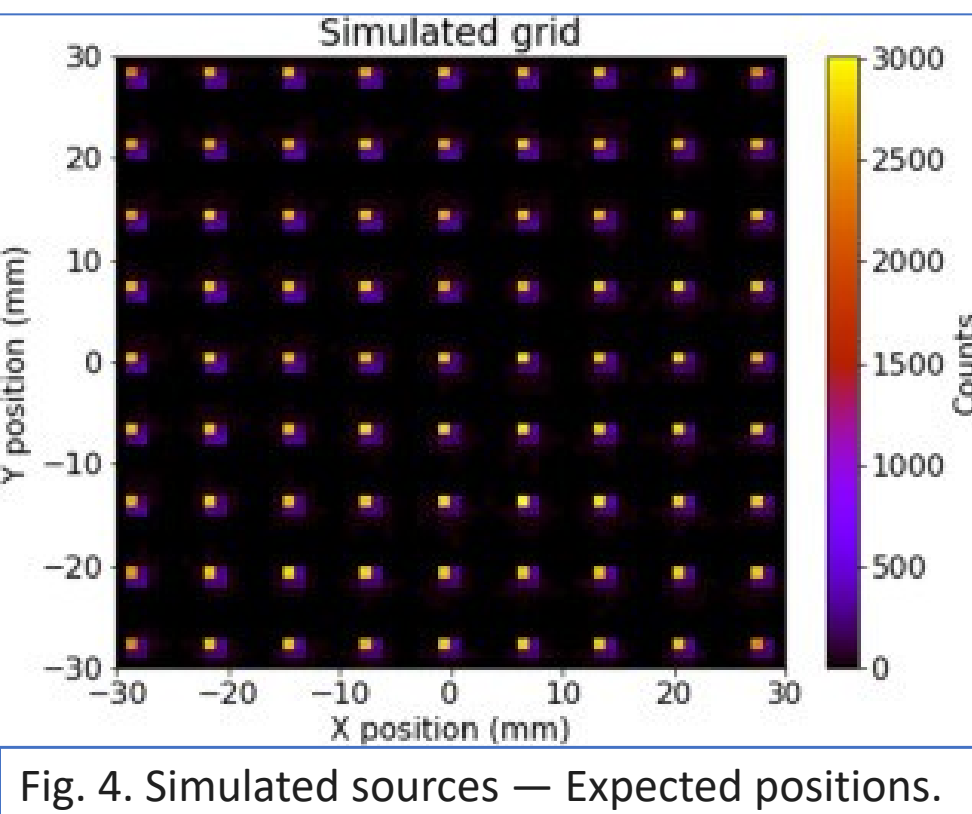


Fig. 4. Simulated sources — Expected positions.

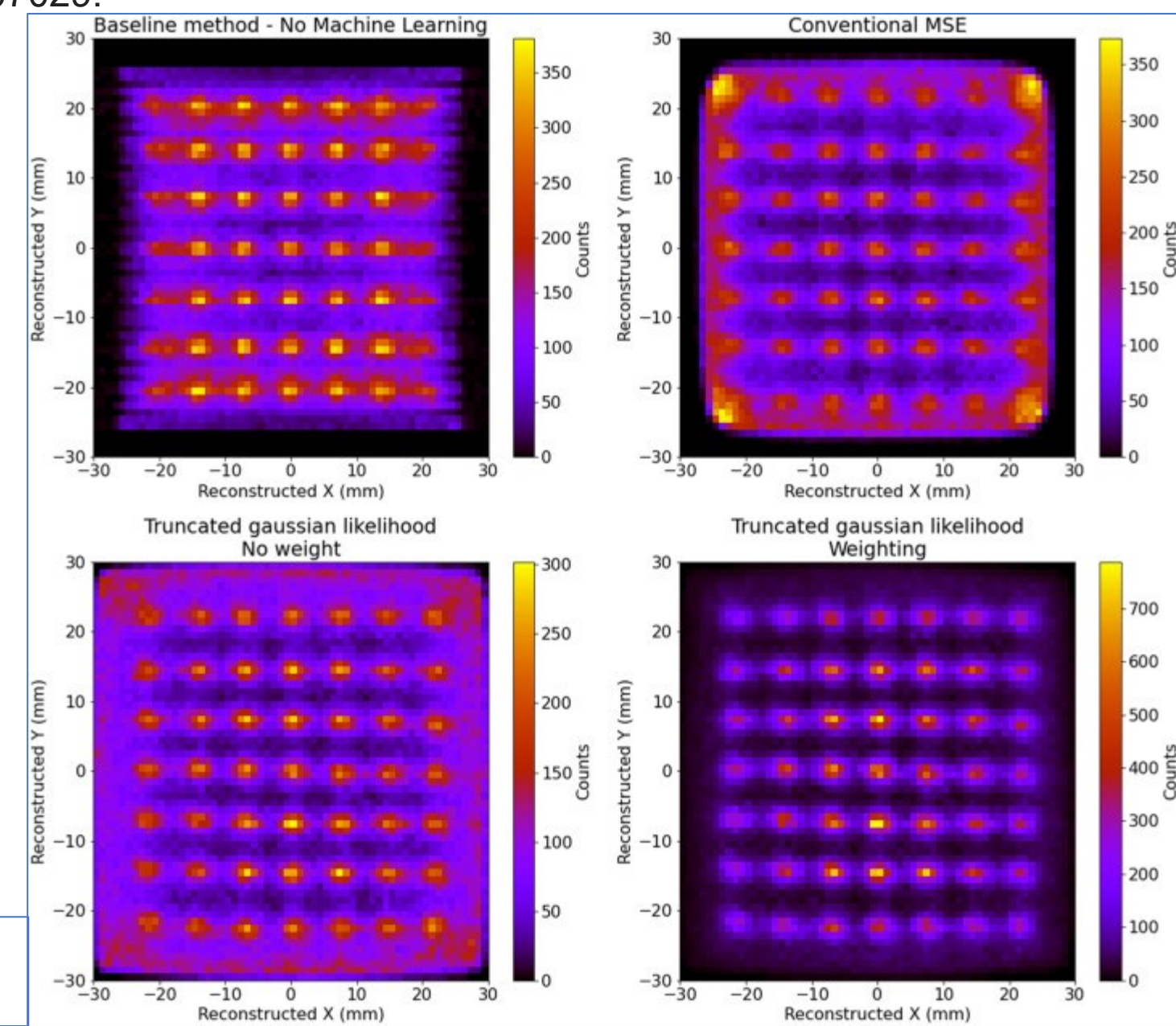


Fig. 5. Grid reconstruction by the different methods.

Yvon, D., Sharyy, V., Follin, M., Bard, J.P., Breton, D., Maalmi, J., Morel, C. and Delagnes, E., 2020. [Design study of a “scintrinsic” crystal targeting tens of picoseconds time resolution for gamma ray imaging: the ClearMind detector](#). *Journal of Instrumentation*, 15(07), p.P07029.

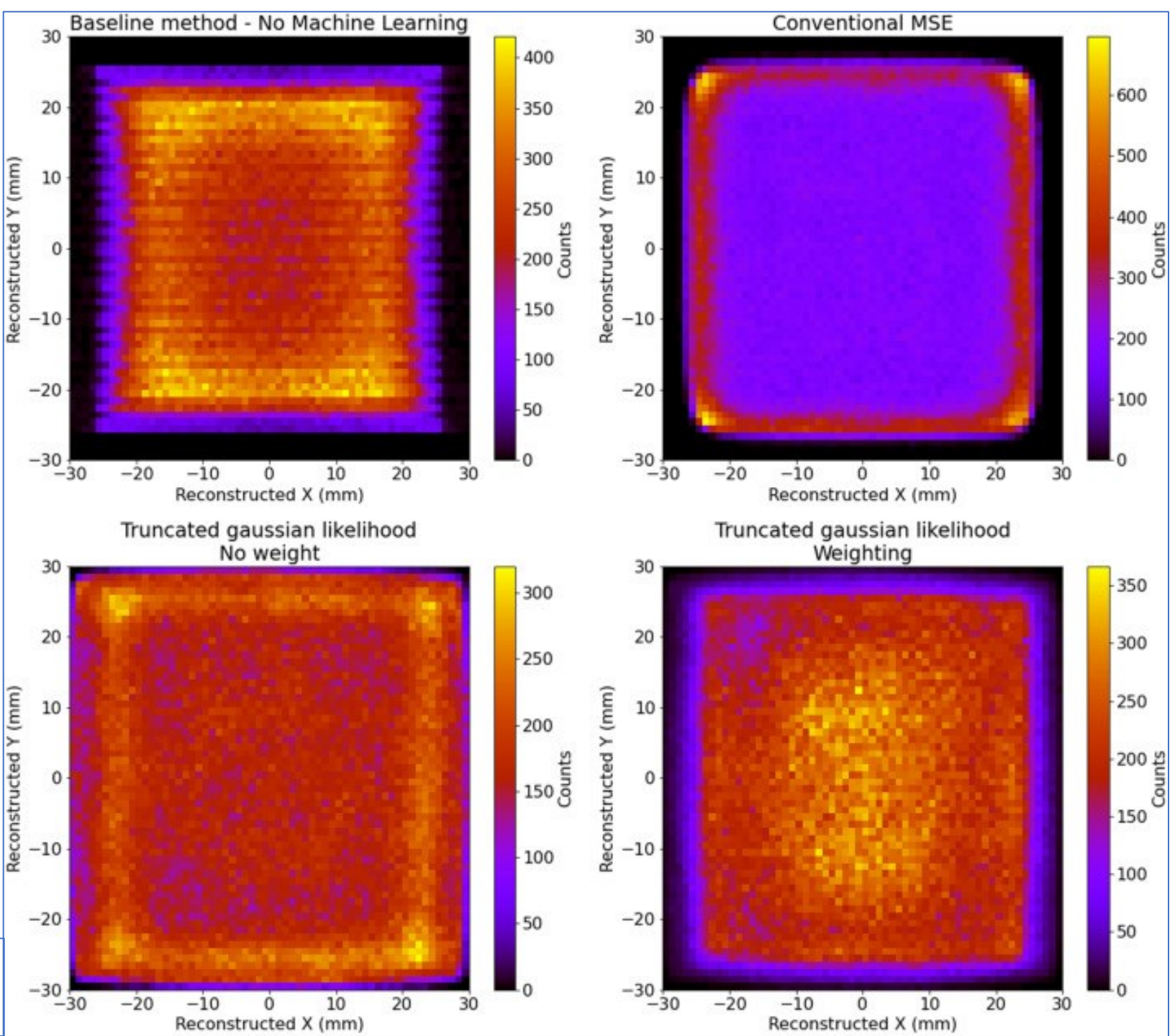
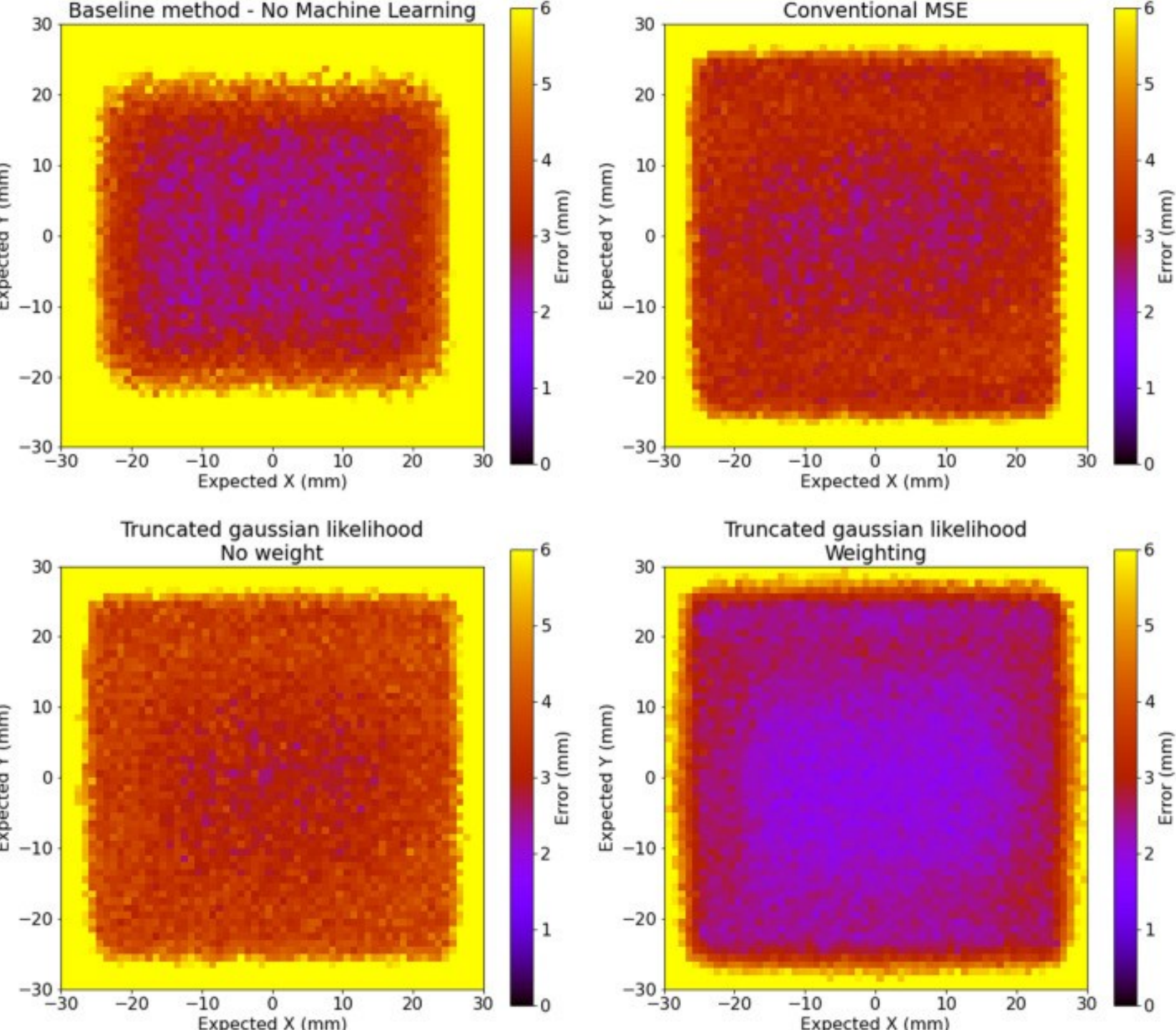


Fig. 6. Reconstruction of the uniform simulation.

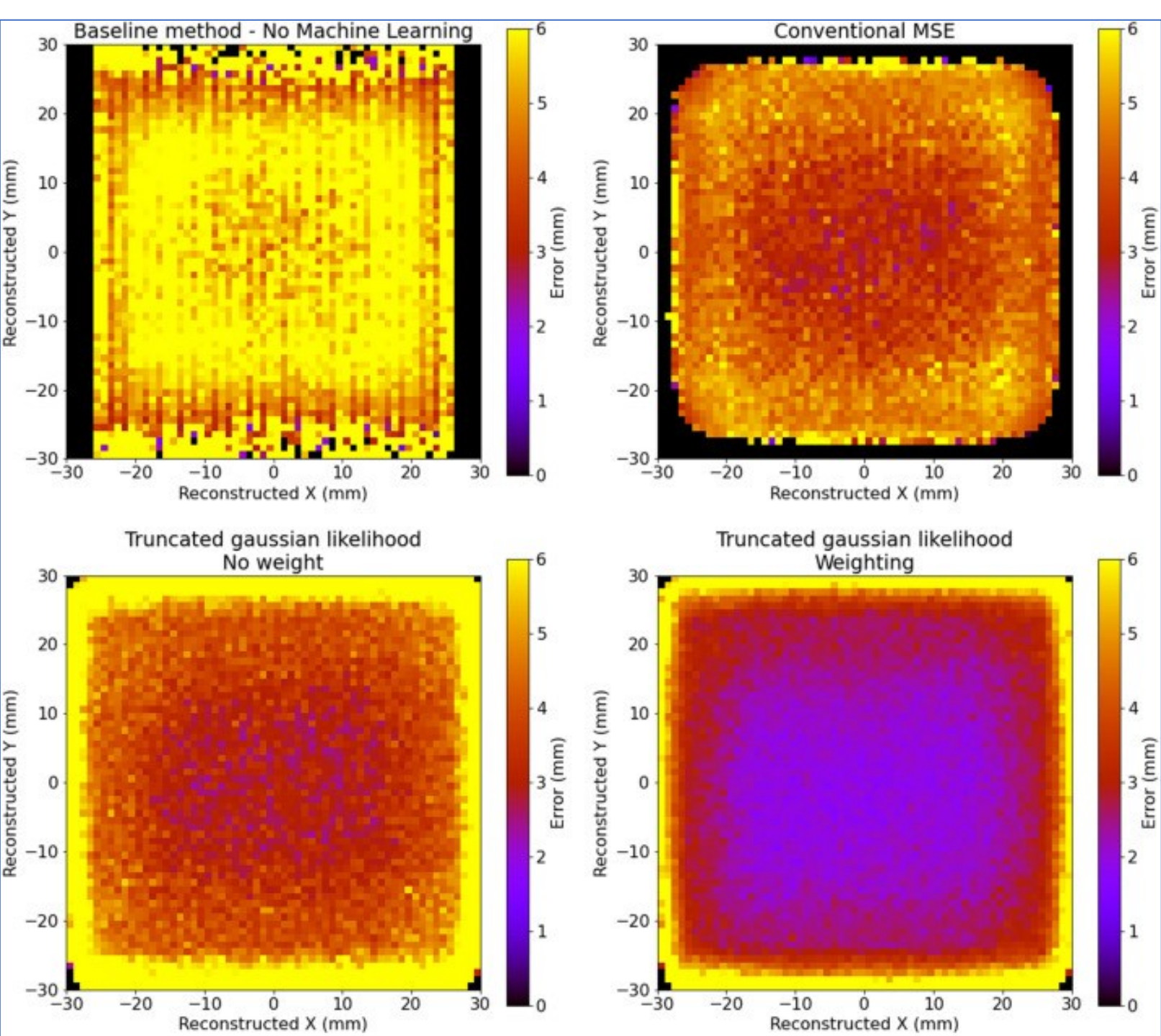
Yvon, D., Sharry, V., Follin, M., Bard, J.P., Breton, D., Maalmi, J., Morel, C. and Delagnes, E., 2020. [Design study of a “scintrinsic” crystal targeting tens of picoseconds time resolution for gamma ray imaging: the ClearMind detector](#). *Journal of Instrumentation*, 15(07), p.P07029.

Fig. 7. 2D error reconstruction according to the true position, corresponding to the spread of the reconstruction — The color scale has been threshold at 6 mm for visualization purpose.

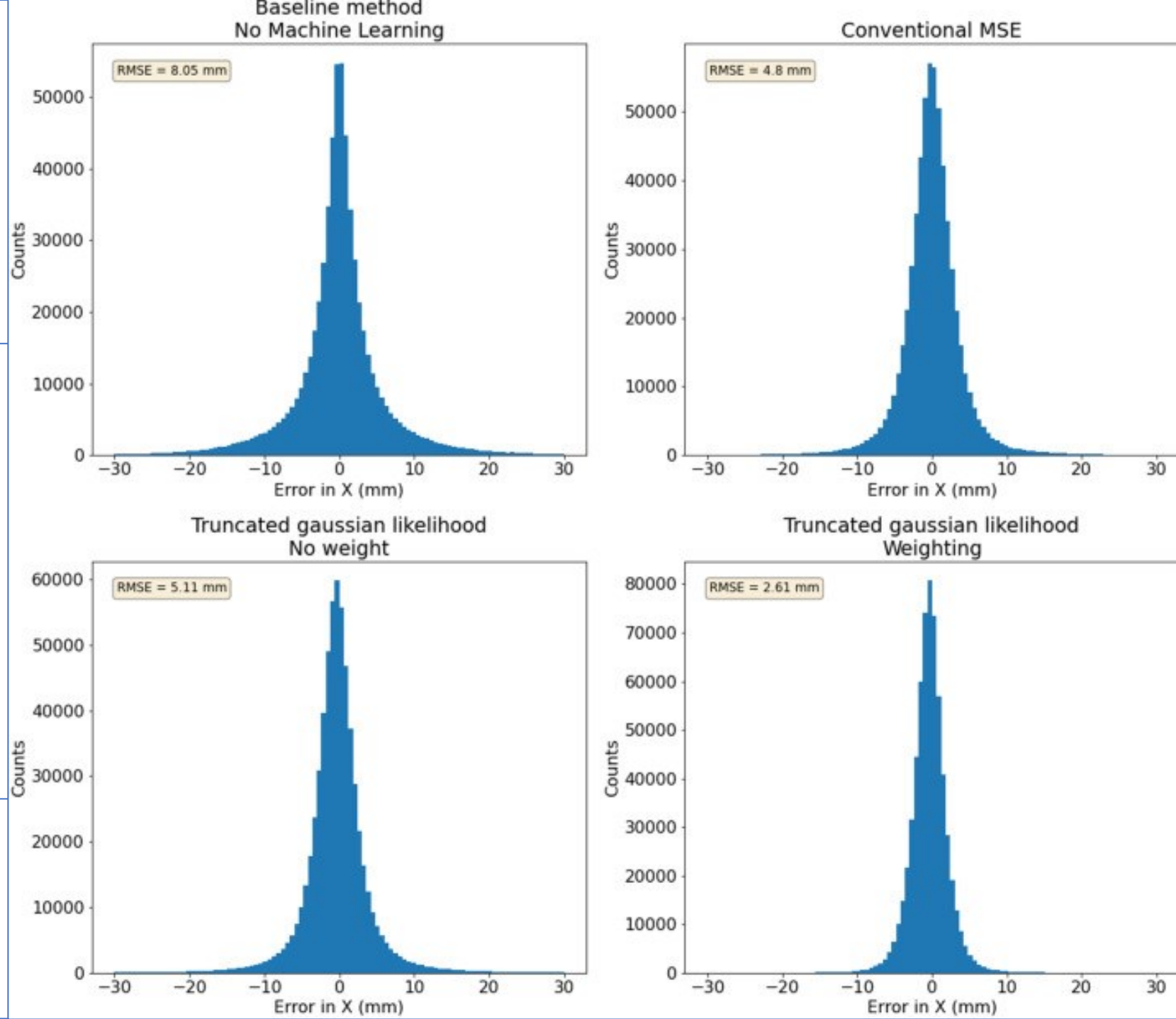


Yvon, D., Sharyy, V., Follin, M., Bard, J.P., Breton, D., Maalmi, J., Morel, C. and Delagnes, E., 2020. [Design study of a “scintrinsic” crystal targeting tens of picoseconds time resolution for gamma ray imaging: the ClearMind detector](#). *Journal of Instrumentation*, 15(07), p.P07029.

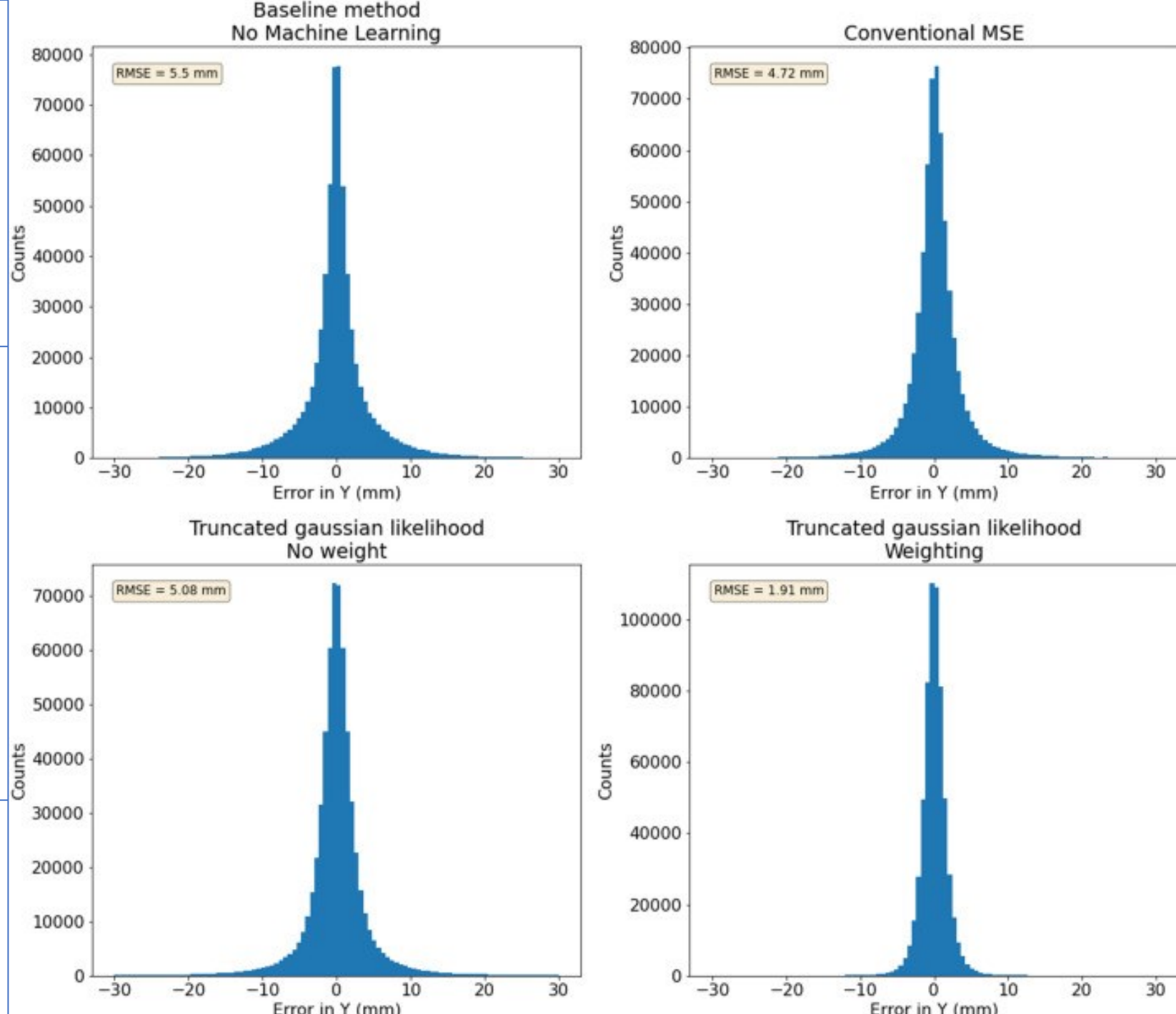
Fig. 8. 2D error reconstruction according to the predicted position, corresponding to the precision of the reconstruction — The color scale has been threshold at 6 mm for visualization purpose.



Yvon, D., Sharyy, V., Follin, M., Bard, J.P., Breton, D., Maalmi, J., Morel, C. and Delagnes, E., 2020. [Design study of a “scintrinsic” crystal targeting tens of picoseconds time resolution for gamma ray imaging: the ClearMind detector](#). *Journal of Instrumentation*, 15(07), p.P07029.



Yvon, D., Sharyy, V., Follin, M., Bard, J.P., Breton, D., Maalmi, J., Morel, C. and Delagnes, E., 2020. [Design study of a “scintrinsic” crystal targeting tens of picoseconds time resolution for gamma ray imaging: the ClearMind detector](#). *Journal of Instrumentation*, 15(07), p.P07029.



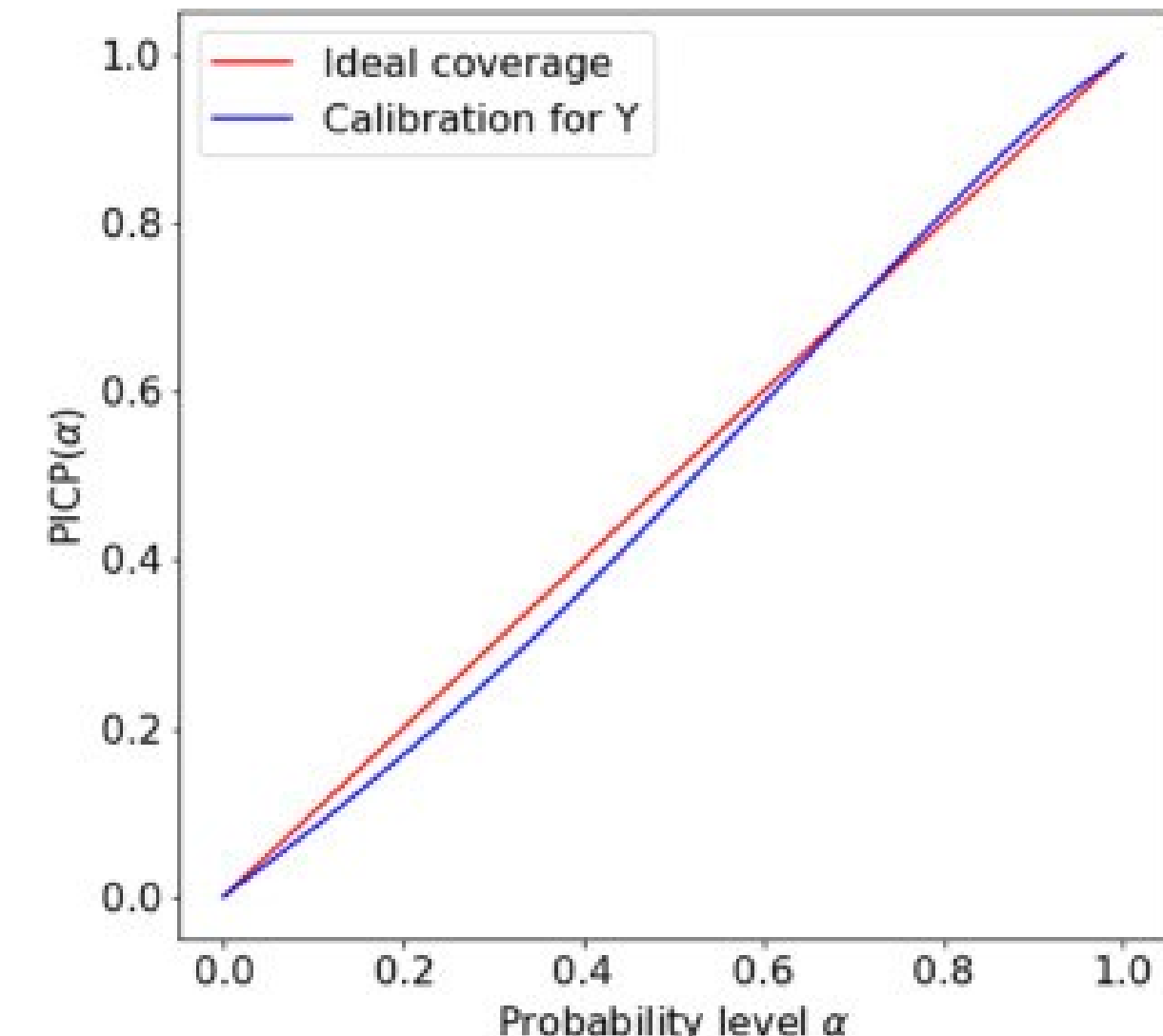
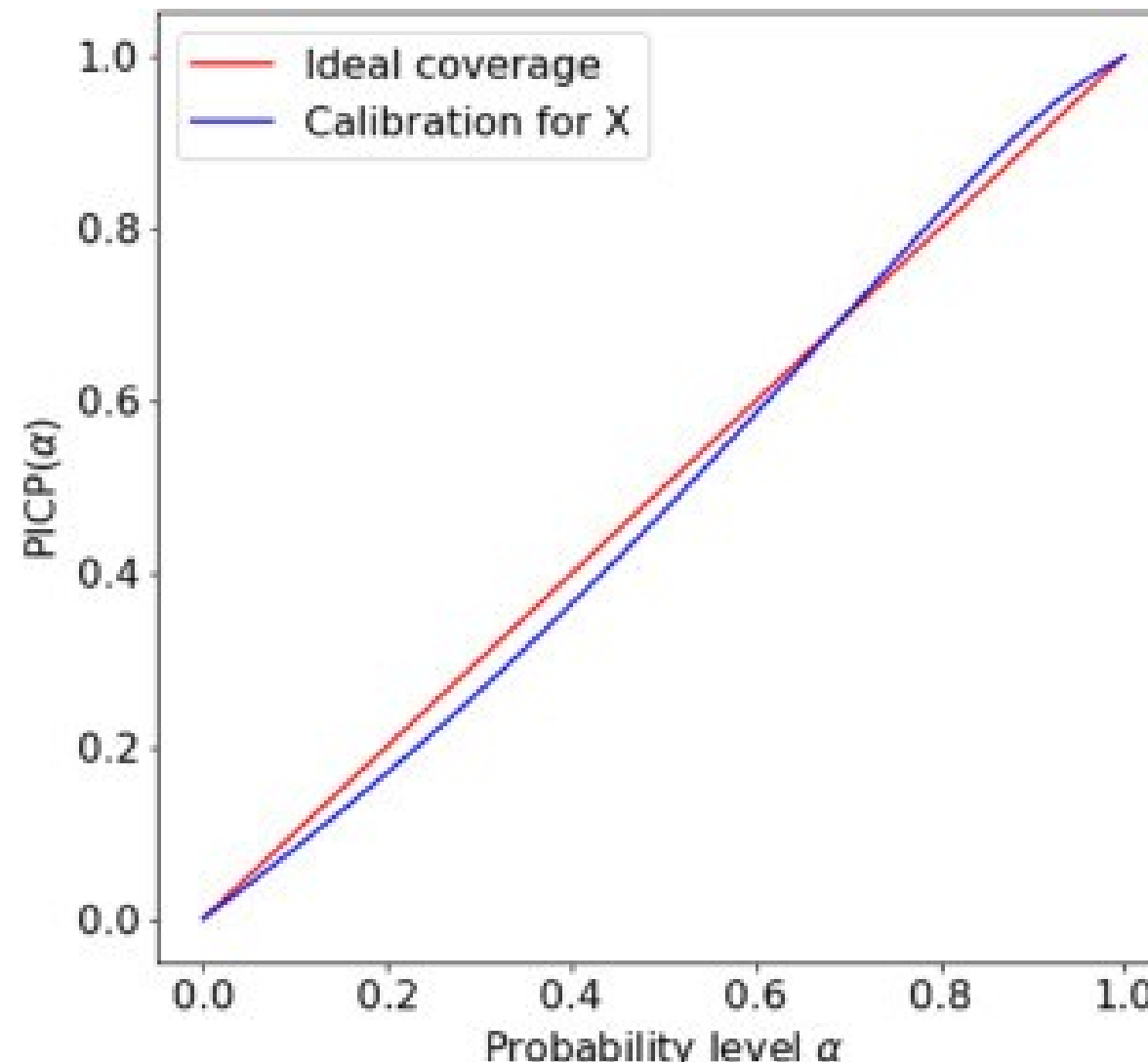


Fig. 11. Coverage plots — The models are slightly too confident for probability levels lower than 75% and slightly too conservative for probability levels higher than 75%.

Daniel, G., Yahiaoui, M.B., Comtat, C., Jan, S., Kochebina, O., Martinez, J.M., Sergeyeva, V., Sharyy, V., Sung, C.H. and Yvon, D., 2024. [Deep Learning reconstruction with uncertainty estimation for \$\gamma\$ photon interaction in fast scintillator detectors](#). *Engineering Applications of Artificial Intelligence*, 131, p.107876.

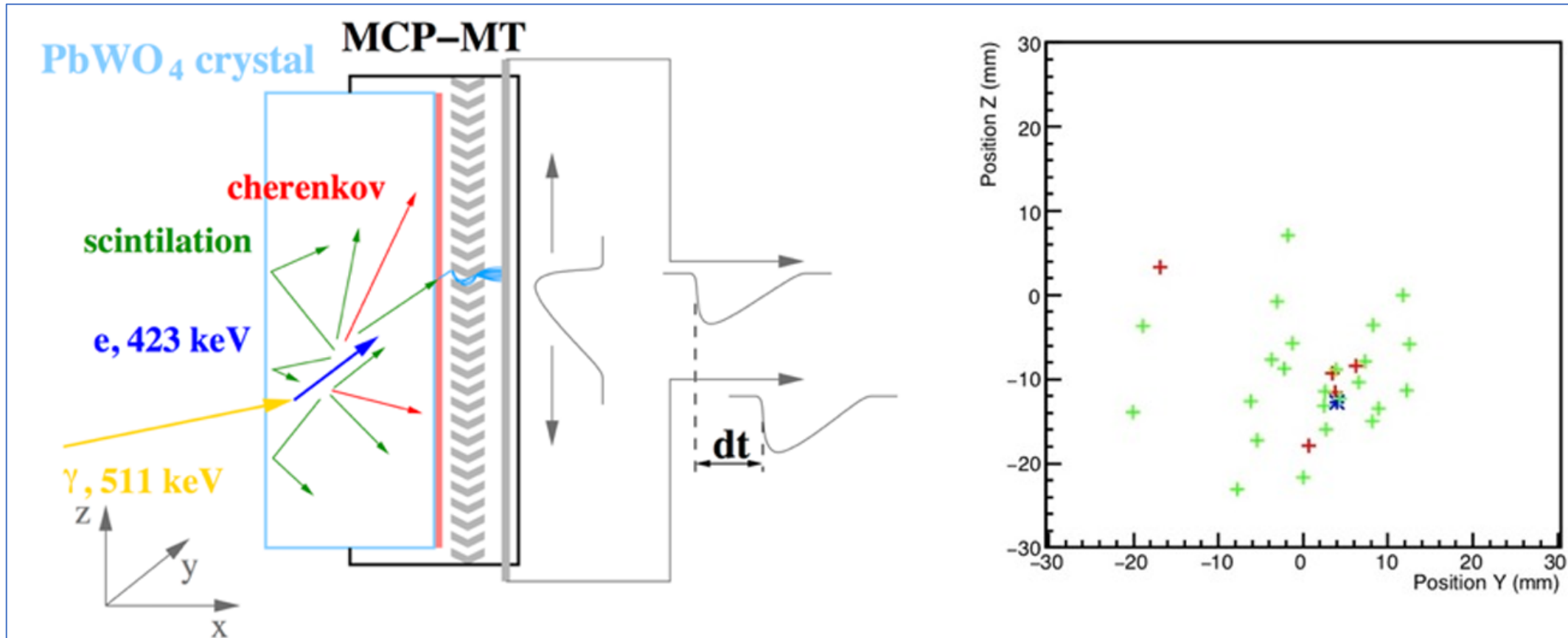


Figure 1: (Left) “Scintrinsic” crystal encapsulated within a MCP-MT. The photocathode is deposited directly on the scintillating crystal. The generated photoelectrons are amplified by a micro-channel plate. The amplified signals are collected on a densely pixelated anode plane read out by transmission lines and fast electronics [Kim, 2012]. (Right) Example of a photoelectron map produced on the photocathode by 511 keV gamma ray interactions within the crystal. The blue crosses mark energy deposits in the crystal, the red ones 5 correspond to the photons detected during the first 500 ps (mainly produced by Cherenkov effect) and the green ones mark scintillation photons detected between 500 ps and 20 ns

Daniel, G., Yahiaoui, M.B., Comtat, C., Jan, S., Kochebina, O., Martinez, J.M., Sergeyeva, V., Sharyy, V., Sung, C.H. and Yvon, D., 2024. [Deep Learning reconstruction with uncertainty estimation for \$\gamma\$ photon interaction in fast scintillator detectors](#). *Engineering Applications of Artificial Intelligence*, 131, p.107876.

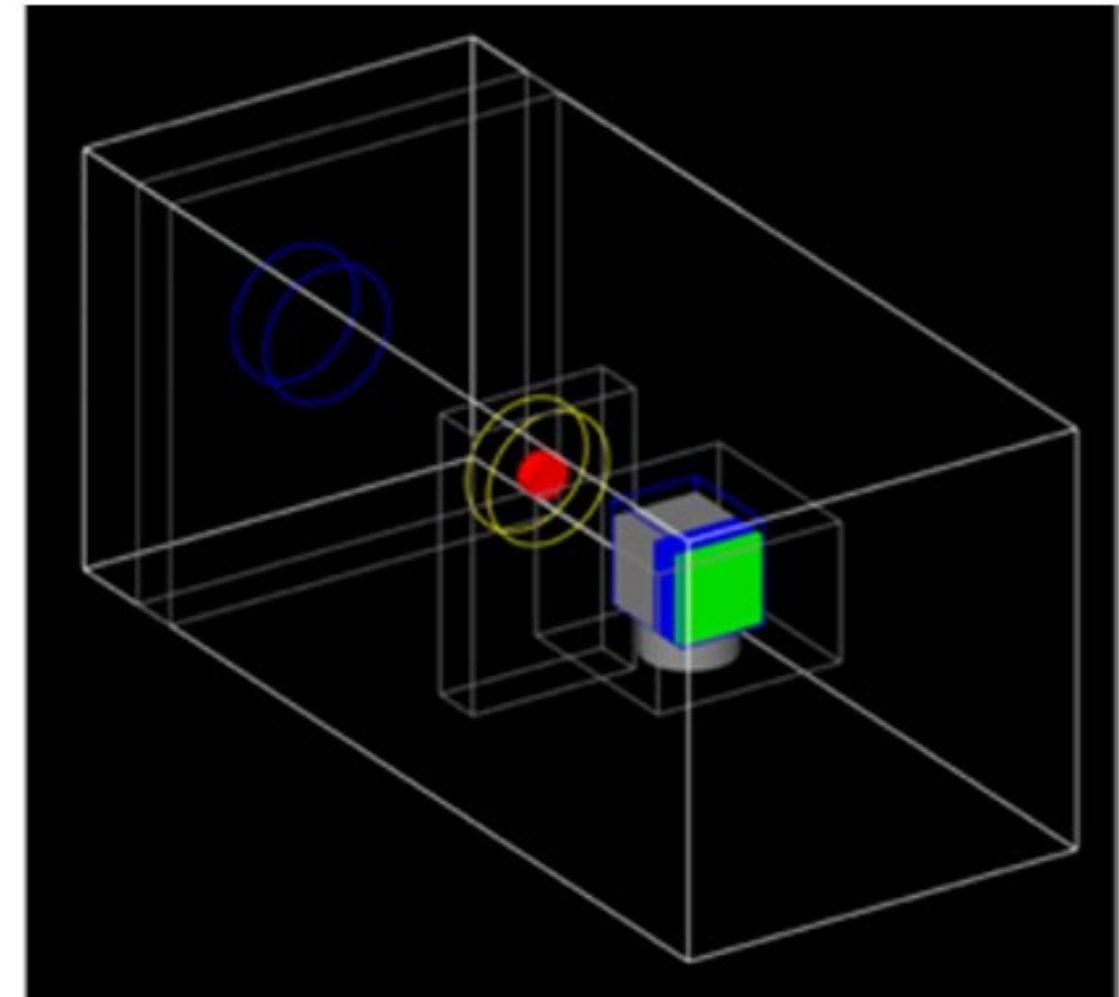
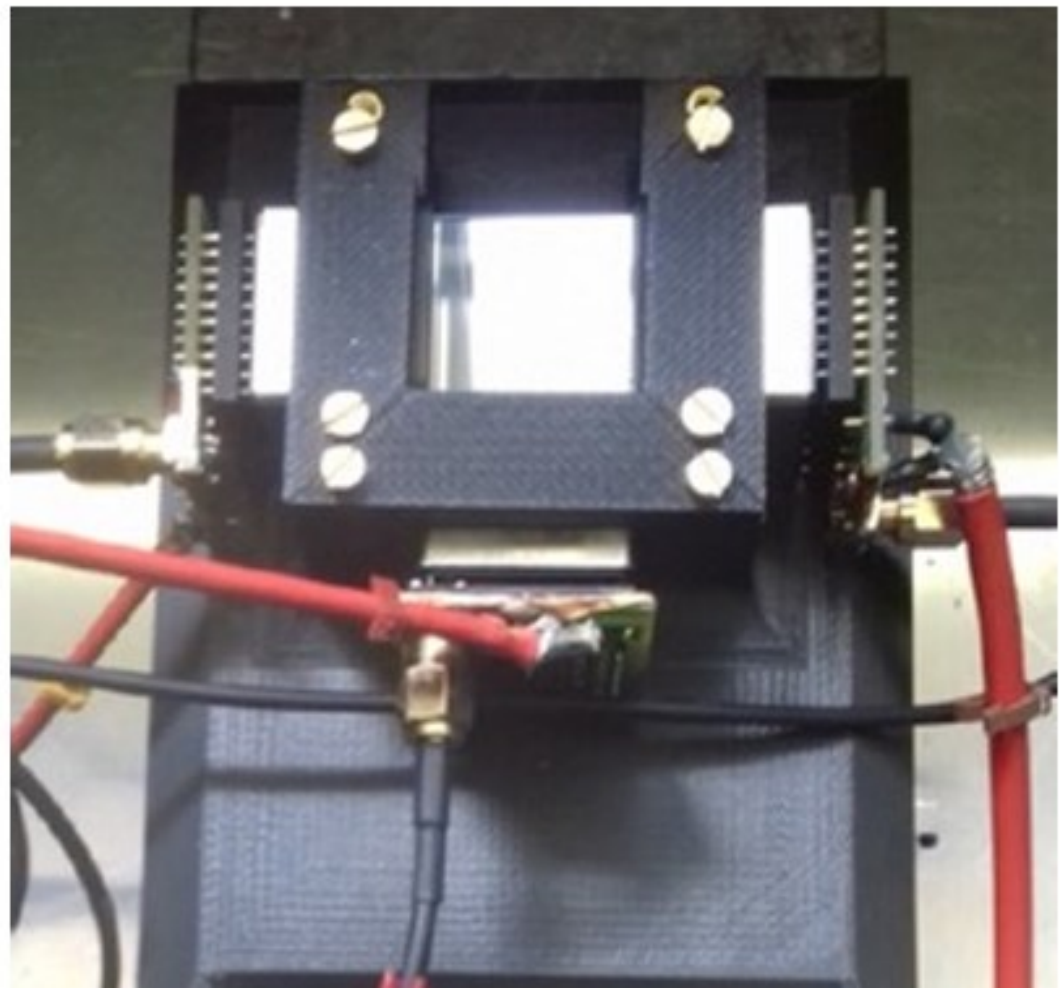


Figure 2: Crystal scintillation properties measurements. (Left) Picture of a cubic PbWO₄ crystal coupled with 3 Hamamatsu R11256-100 photomultipliers using optical gel. (Right) Simplified Monte Carlo simulation layout of the light yield measurement setup. We have used a 25 ' 25 ' 10 mm² PbWO₄ crystal grounded on all its faces, but the one coupled to the photomultiplier. We used a ²²Na radioactive source and an additional YAP detector to tag the 511 keV photons from positron annihilations.

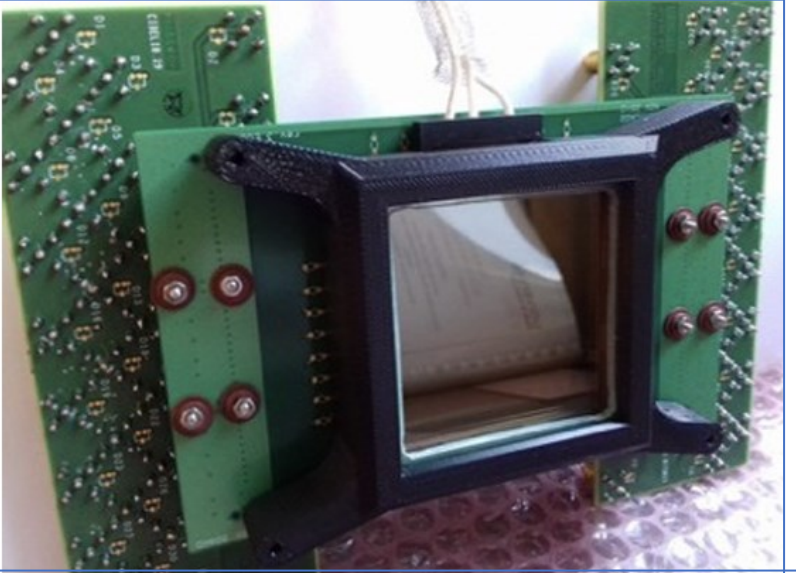


Figure 3: Picture of the MCP-PMT photodetector used for these developments.

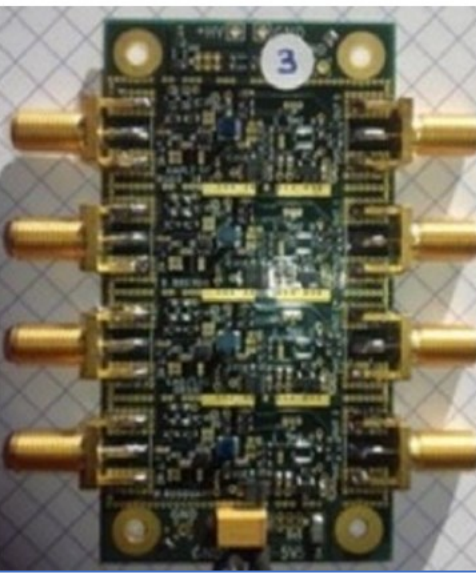


Figure 4: (Left) 4-channels fast amplifier prototype with a 700 MHz bandwidth and a gain of 100 used for the tests described in this work. (Right) 32-channels SAMPIC waveform recorder, which is currently used on many test benches all around the world [SAMPIC Workshop].

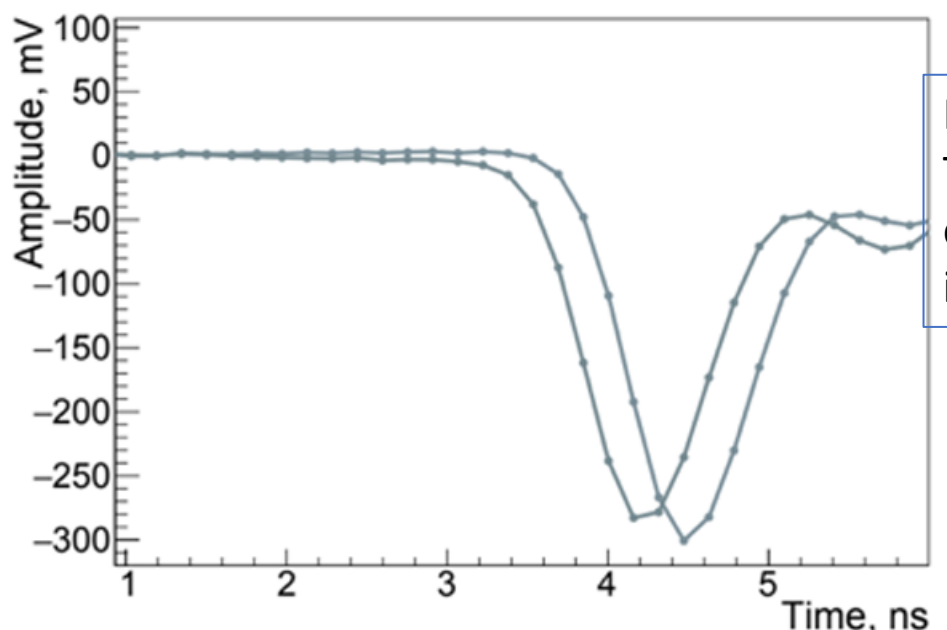


Figure 5: Single photoelectron as detected by the XP-85122 MCP-PMT. The pulses are registered by the SAMPIC Waveform recorder at both ends of a readout transmission line. Before the pulse, the signal shape is very flat, showing that the readout noise is minimal.

Daniel, G., Yahiaoui, M.B., Comtat, C., Jan, S., Kochebina, O., Martinez, J.M., Sergeyeva, V., Sharyy, V., Sung, C.H. and Yvon, D., 2024. [Deep Learning reconstruction with uncertainty estimation for \$\gamma\$ photon interaction in fast scintillator detectors](#). *Engineering Applications of Artificial Intelligence*, 131, p.107876.

Daniel, G., Yahiaoui, M.B., Comtat, C., Jan, S., Kochebina, O., Martinez, J.M., Sergeyeva, V., Sharyy, V., Sung, C.H. and Yvon, D., 2024. [Deep Learning reconstruction with uncertainty estimation for \$\gamma\$ photon interaction in fast scintillator detectors](#). *Engineering Applications of Artificial Intelligence*, 131, p.107876.

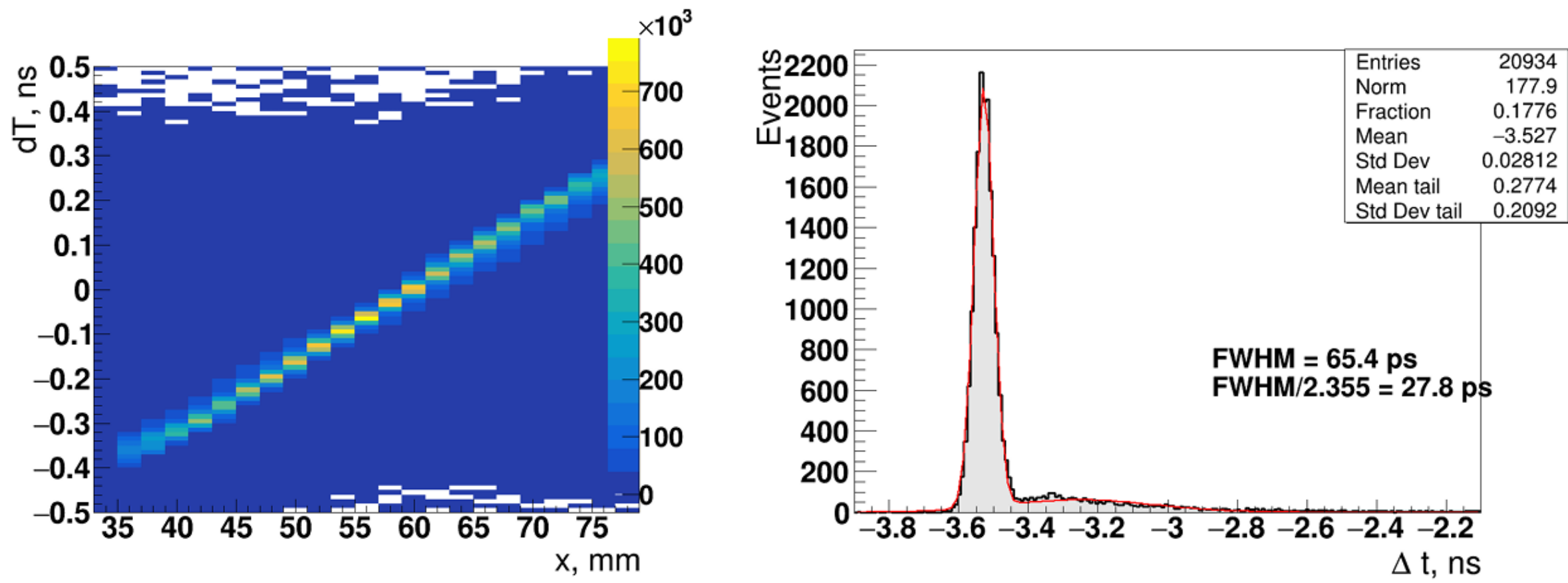


Figure 6: (Left) Histogram of position of the pinhole along the line versus time difference between signals registered at both ends of the targeted transmission line. (Right) Histogram of the time difference between the laser pulse and the average of the pulse times measured at both ends of the transmission lines.

Daniel, G., Yahiaoui, M.B.,
Comtat, C., Jan, S.,
Kochebina, O., Martinez,
J.M., Sergeyeva, V.,
Sharyy, V., Sung, C.H. and
Yvon, D., 2024. [Deep Learning reconstruction with uncertainty estimation for \$\gamma\$ photon interaction in fast scintillator detectors](#). *Engineering Applications of Artificial Intelligence*, 131, p.107876.

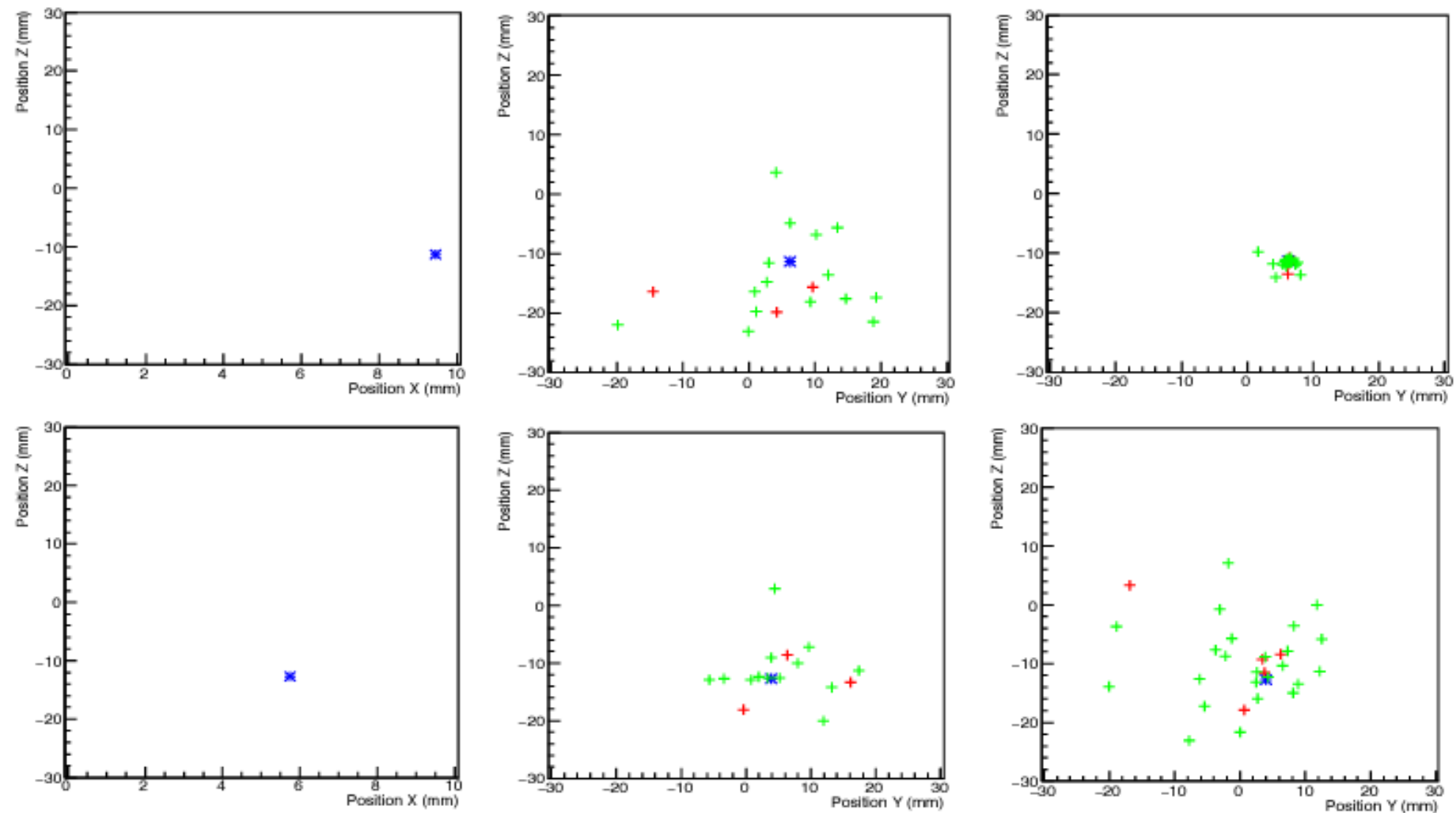


Figure 7: Simulated data for a 10 mm thick “scintrinsic” crystal instrumented on two sides by a bialkali photocathode. 511 keV gamma rays impinge on the detector from the left and propagate along the X axis. The upper and lower rows correspond to the photoelectric interaction of gamma rays close to the surface of the crystal and at mid-crystal depth, respectively. Notice the coordinates axis of each of the figures.

(left) Blue crosses denote gamma ray interactions within the crystal. **(centre and right)** show photoelectrons produced on the two photocathodes. Red and green crosses mark photoelectrons produced at $X = 0$ mm (center) and $X = 10$ mm (right) during the first 500 ps and the following 20 ns, respectively.

Daniel, G., Yahiaoui, M.B., Comtat, C., Jan, S., Kochebina, O., Martinez, J.M., Sergeyeva, V., Sharyy, V., Sung, C.H. and Yvon, D., 2024. [Deep Learning reconstruction with uncertainty estimation for \$\gamma\$ photon interaction in fast scintillator detectors](#). *Engineering Applications of Artificial Intelligence*, 131, p.107876.

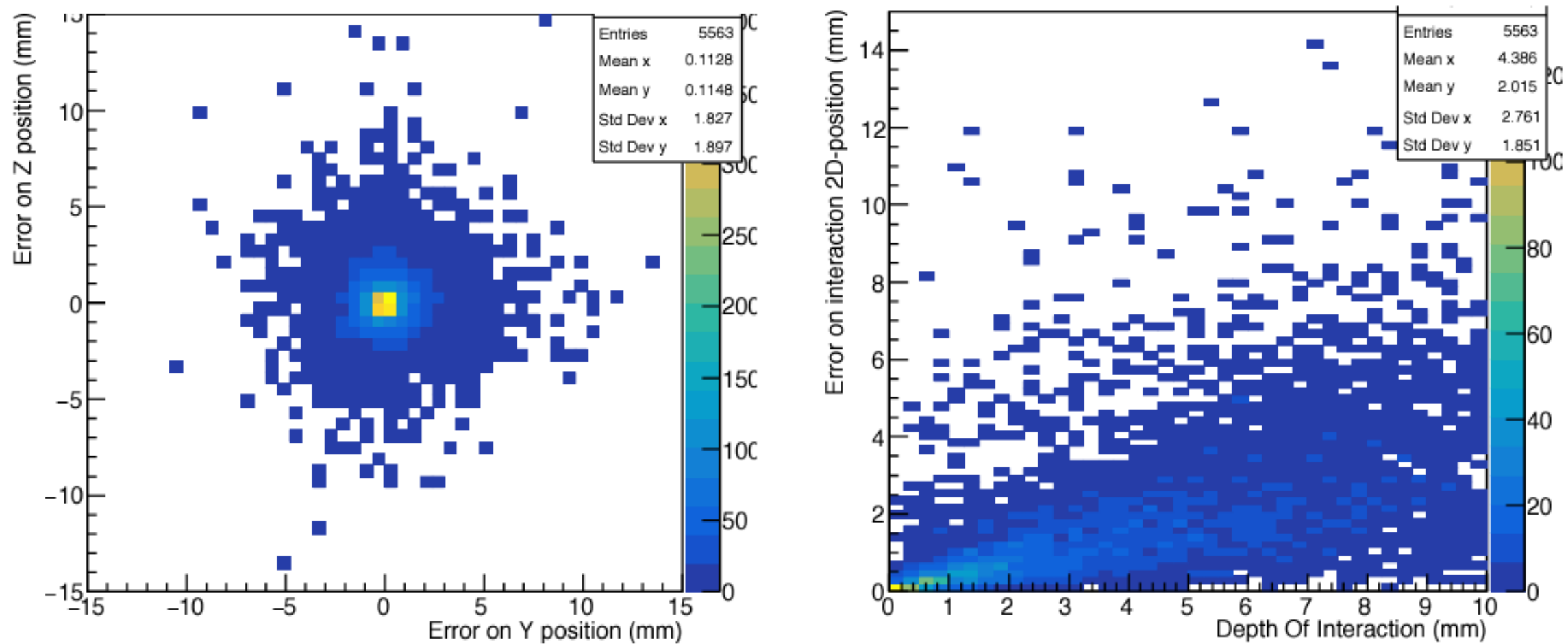


Figure 8: (Left) 2D histogram of the difference of computed Y and Z coordinates of the PE barycenter and the gamma ray position, using robust statistics. (Right) 2D histogram of $\text{Dist}_{\text{baryPE}}$ (see text for the definition) versus DOI. In these figures, we have used data from the front photocathode only. No selections were applied on the energy deposited in the PbWO₄ crystal.

Daniel, G., Yahiaoui, M.B., Comtat, C., Jan, S., Kochebina, O., Martinez, J.M., Sergeyeva, V., Sharyy, V., Sung, C.H. and Yvon, D., 2024. [Deep Learning reconstruction with uncertainty estimation for \$\gamma\$ photon interaction in fast scintillator detectors](#). *Engineering Applications of Artificial Intelligence*, 131, p.107876.

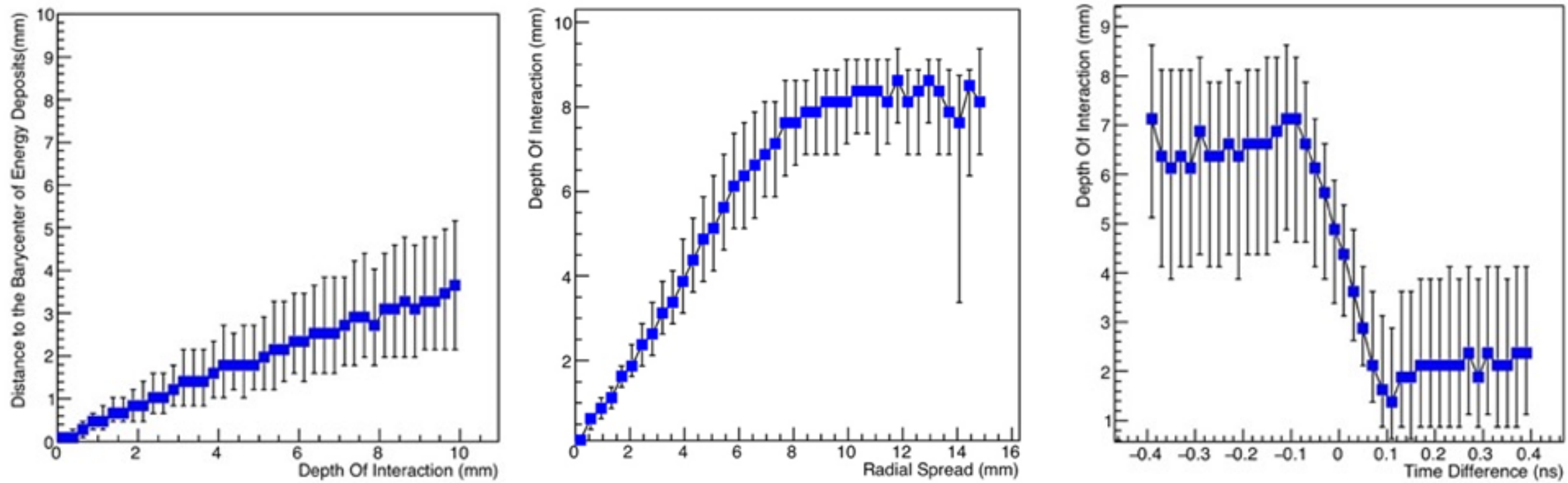


Figure 9: (Left) $\text{Dist}_{\text{BaryPE}}$ versus DOI. (Center) DOI as function of hit-map radial spread. (Right) DOI as function of time difference between the first photoelectron detected on the front and the rear photocathodes. For these three graphs, points show the mean values, bars on points correspond to the quartile value of the distribution statistics. No selections on energy deposited in the crystal were made.

Daniel, G., Yahiaoui, M.B., Comtat, C., Jan, S., Kochebina, O., Martinez, J.M., Sergeyeva, V., Sharyy, V., Sung, C.H. and Yvon, D., 2024. [Deep Learning reconstruction with uncertainty estimation for \$\gamma\$ photon interaction in fast scintillator detectors](#). *Engineering Applications of Artificial Intelligence*, 131, p.107876.

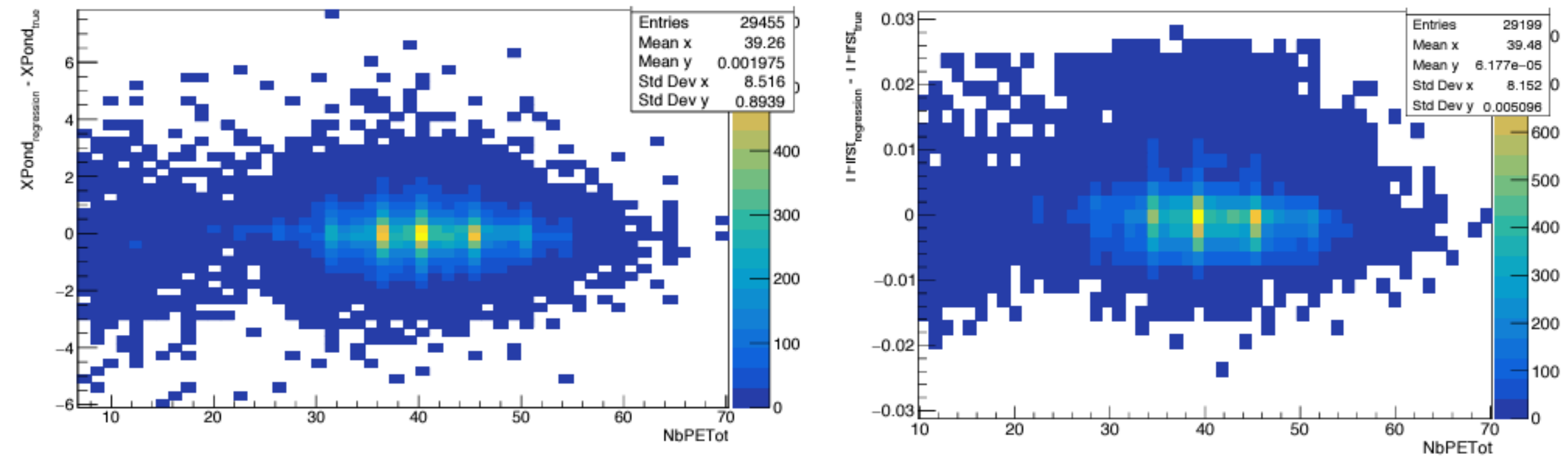


Figure 10: Evaluation of the performances of the MLP algorithms to reconstruct DOI and gamma ray interaction time within the PbWO₄ crystal from hit-map data. (Left) 2D histogram of the number of detected photoelectron versus the difference between reconstructed and simulated DOI (mm). (Right) 2D histogram of the number of detected photoelectron versus the difference between reconstructed and simulated time of the first gamma ray interaction (ns) within the crystal. No selection cuts were applied on simulated data.

Abstract

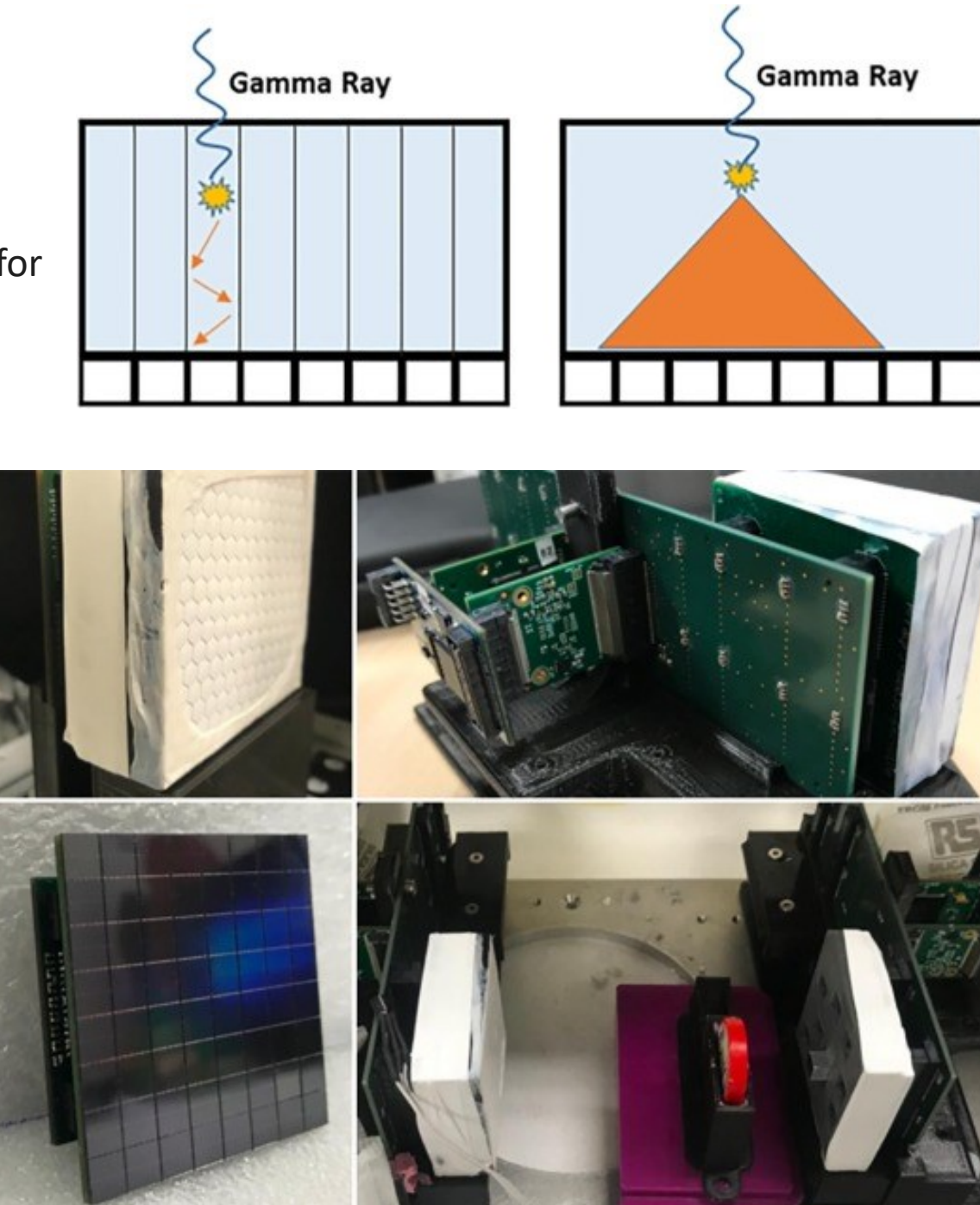
Objective. The high production cost of commonly used lutetium-based fast scintillators and the development of silicon photomultipliers technology have made bismuth germanate (BGO) a promising candidate for time-of-flight positron emission tomography (TOF PET) detectors owing to its generation of prompt Cherenkov photons. However, using BGO as a hybrid scintillator is disadvantageous owing to its low photon statistics and distribution that does not conform well to a single Gaussian. To mitigate this, a proposal was made to increase the likelihood of detecting the first Cherenkov photons by positioning two photosensors in opposition at the entrance and exit faces of the scintillator and subsequently selectively picking an earlier timestamp. Nonetheless, the timing variation arising from the photon transit time remains affected by the entire length of the crystal, thereby presenting a possibility for further enhancement. **Approach.** In this study, we aimed to improve the timing performance of the dual-ended BGO Cherenkov TOF PET detector by capitalizing on the synergistic advantages of applying depth-of-interaction (DOI) information and crystal surface finishes or reflector properties. A dual-ended BGO detector was implemented using a $3 \times 3 \times 15$ mm³ BGO crystal. Coincidence events were acquired against a $3 \times 3 \times 3$ mm³ LYSO:Ce:Mg reference detector. The timing performance of the dual-ended BGO detectors was analyzed using conventionally proposed timestamp methods before and after DOI correction. **Results.** Through a DOI-based correction of photon transit time spread, we demonstrated a further improvement in the timing resolution of the BGO-based Cherenkov TOF PET detector utilizing a dual-ended detector configuration and adaptive arrival time pickoff. We achieved further improvements in timing resolution by correcting the offset spread induced by the fluctuation of timing signal rise time in the dual-ended detector. **Significance.** Although polishing the crystal surface was still favorable in terms of full-width-half-maximum value, incorporating DOI information from the unpolished crystal to compensate for photon travel time facilitated additional enhancement in the overall timing performance, thereby surpassing that achieved with the polished crystal.

Lamprou, E., Gonzalez, A.J., Sanchez, F. and Benlloch, J.M., 2020. [Exploring TOF capabilities of PET detector blocks based on large monolithic crystals and analog SiPMs](#). *Physica Medica*, 70, pp.10-18.

Fig. 1. Representation of the scintillation light distribution for one gamma event inside a pixelated crystal (left) and a monolithic block (right).

Fig. 2. Top-left, monolithic block ($50 \times 50 \times 15 \text{ mm}^3$) with a RR layer at the entrance. Top-right, TOFPET2 ASIC Front-End-Module. Bottom-left, [SiPM](#) 8×8 array with $6 \times 6 \text{ mm}^2$ each [photosensor](#) element. Bottom-right, experimental set-up based on a monolithic block and a reference single pixel detector.

In this work we study the timing behaviour of detectors composed by monolithic crystals and analog SiPMs read out by an ASIC. The scintillation light spreads across the crystal towards the photosensors, resulting in a high number of SiPMs and ASIC channels fired. This has been studied in relation with the Coincidence Timing Resolution (CTR). We have used LYSO monolithic blocks with dimensions of $50 \times 50 \times 15 \text{ mm}^3$ coupled to [SiPM](#) arrays (8×8 elements with $6 \times 6 \text{ mm}^2$ area) which compose detectors suitable for clinical applications.



Lamprou, E., Gonzalez, A.J., Sanchez, F. and Benlloch, J.M., 2020. [Exploring TOF capabilities of PET detector blocks based on large monolithic crystals and analog SiPMs](#). *Physica Medica*, 70, pp.10-18.

3.1. Pixelated crystals: one-to-one coupling

The experiments with the KETEK PA3325 SiPMs and the small crystal pixels showed a CTR of 186 ps FWHM using default ASIC thresholds. Both detectors showed an energy resolution near 10.8% after correction for the SiPM saturation. [Fig. 3](#) top shows both the energy plot and CTR histogram. The measurement was carried out at 19 °C. The tests were repeated using the $6 \times 6 \text{ mm}^2$ photosensors and LYSO pixels of $6 \times 6 \times 15 \text{ mm}^3$. Despite the larger active area of the photosensors that might introduce signal jitter due to larger capacitances, and the thickness of 15 mm of the LYSO pixels, a timing resolution of 330 ps FWHM was obtained ([Fig. 3](#) bottom). For this set-up, the energy resolution was found to be 13.7% after again applying an energy calibration.

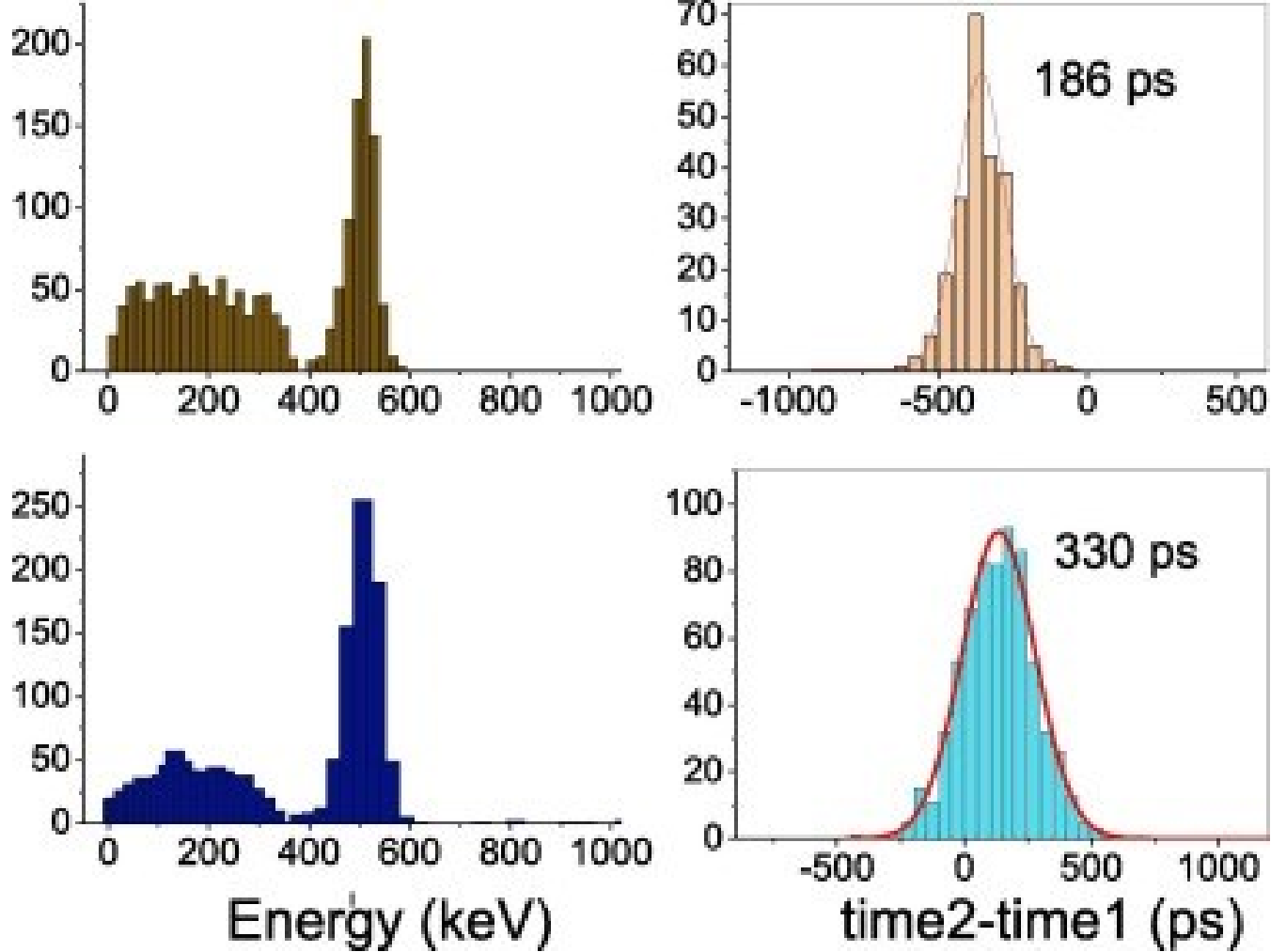


Fig. 3. Top, [energy spectrum](#) after energy calibration of one detector and time distribution obtained with 3 mm SiPMs and LYSO crystals of $3 \times 3 \times 5 \text{ mm}^3$. Bottom, energy spectrum (after calibration) of one detector and time distribution obtained with 6 mm SiPMs and LYSO crystals of $6 \times 6 \times 15 \text{ mm}^3$.

Lamprou, E., Gonzalez, A.J., Sanchez, F. and Benlloch, J.M., 2020. [Exploring TOF capabilities of PET detector blocks based on large monolithic crystals and analog SiPMs](#). *Physica Medica*, 70, pp.10-18.

3.2. Monolithic blocks, light sharing

The small size source was placed right in front of the reference detector and, therefore, the whole area of the monolithic crystal was irradiated during the coincidence measurements. An energy profile of all events in the monolithic crystal is shown in Fig. 4 top-left. Events within the [photopeak](#) (30–48 ADC units) were selected for data analysis. Three different Regions of Interests (ROIs) at the corner, middle and center of the detector block, were selected by applying a position filter, as depicted in Fig. 4 bottom-left. Moreover, for each ROI, the DOI distribution of events was obtained, allowing us to further split the data in three DOI regions (about 5 mm each) depending on the gamma ray impact Z coordinate. They are named as DOI1 for events at the crystal entrance, DOI2 for events occurring at the middle of the scintillator and DOI3 for events impinging at the bottom crystal layer (see Fig. 4 top-right). Therefore, an estimation of the average number of channels that crossed the threshold and, hence, of the SNR per channel could be obtained for each gamma-ray impact. As seen in Fig. 4 bottom-right, we observed that independently of the XY position, a larger spread of the scintillation light was found for events at the upper crystal layers (DOI1). For impacts impinging deeper in the monolithic crystal e.g. DOI2 and DOI3, we can observe a slightly decreased number of channels fired, but still high suggesting a poor SNR per ASIC channel.

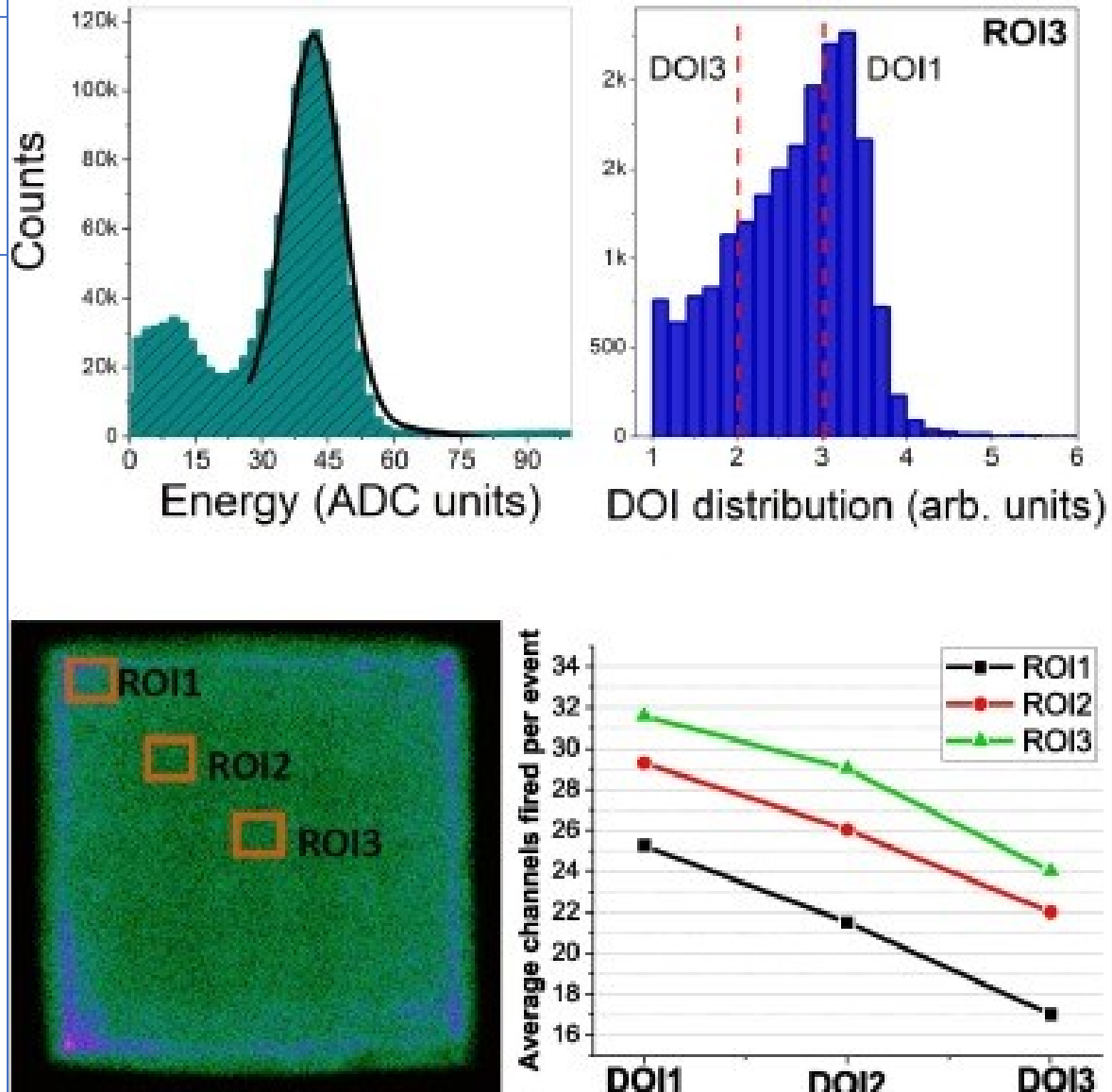


Fig. 4. Top-left, [energy spectrum](#) of the whole monolithic based detector before calibration. The black line shows a fit to the distribution using a Guassian profile plus a line. Top-right, DOI distribution of the events recorded at the center of the monolithic crystal (ROI3). Bottom-left, flood map of events, showing the three ROI selected for analysis. Bottom-right, average number of channels fired per event, as a function of the DOI and for the three ROIs.

Lamprou, E., Gonzalez, A.J., Sanchez, F. and Benlloch, J.M.,
2020. [Exploring TOF capabilities of PET detector blocks based on large monolithic crystals and analog SiPMs](#). *Physica Medica*, 70, pp.10-18.

A significant dependency of the number of fired channels with the gamma-ray impact position is observed. The nearest an event occurred to the edge of the crystal, the more it suffers from light truncation as a high amount of scintillation photons are absorbed by the black painted walls. This fact explains the decreased number of channels fired for ROI1 and ROI2. It should be noticed, that these distributions are in general directly related to the dimensions and thickness of the crystal block as well as to the crystal [treatment](#) and [photosensor geometry](#).

We have shown that the generated SNR per photosensor element strongly depends on the position of each particular event. Since an average of 25 channels are fired for each gamma-ray event, a poor SNR in the ASIC channels is expected. Gamma-ray impacts near the crystal entrance (DOI1), which is the most probable scenario, will fire many photosensors but with a reduced number of collected scintillation photons per photosensor. This statement limits the basic TOF requirements, namely a short and sharp rise time of the signals [\[12\]](#). On the contrary, events near the photosensor show a narrower light spread (DOI3), permitting a faster and a more efficient collection of optical photons. We shorted all impacts based on their timestamps and we used this information to fill the histograms shown in [Fig. 5](#) top. Earliest hit 0 (X-axis of the histogram) means that the first timestamp also collected the maximum number of optical photons. Whereas for instance, hit labelled 10 means that the 10th impact collected the highest energy for this given gamma-ray event. Therefore, for gamma-ray impacts near the photosensor (DOI3), the channels collecting the highest amount of energy also correspond to the fastest ones (first hits). That is, we observe the hits with highest energy being the earliest collected. However, impacts at the crystal entrance exhibit a wider distribution of energy hits and time. This fact, was found to be directly related with the timing resolution.

Lamprou, E., Gonzalez, A.J., Sanchez, F. and Benlloch, J.M., 2020. [Exploring TOF capabilities of PET detector blocks based on large monolithic crystals and analog SiPMs](#). *Physica Medica*, 70, pp.10-18.

Also interesting is the analysis of the energy ranges of the earliest channel triggered (earliest timestamp recorded) which complements the previously described behavior. By averaging the energies of the eight earliest hits for all events, it was clearly shown that the first recorded hit shows much higher energy ranges compared with the later recorded ones for the case of deep [DOIs](#), while at the higher DOI1, the energy ranges for all 8 first hits are all comparable ([Fig. 5](#) bottom). It should be noted, that these plots were obtained for the whole scintillator volume without using the previously described position filter. No significant variations are expected in these distributions for independent ROIs. The variations in the spread of the scintillation light depending on the DOI of each gamma event lead to explore the optimal event timestamp assignment method [\[23\]](#). When that many hits occurred for each event, it is critical to study if the optimal time resolution is given when using the first timestamp recorded of each event or an alternative approach is may needed.

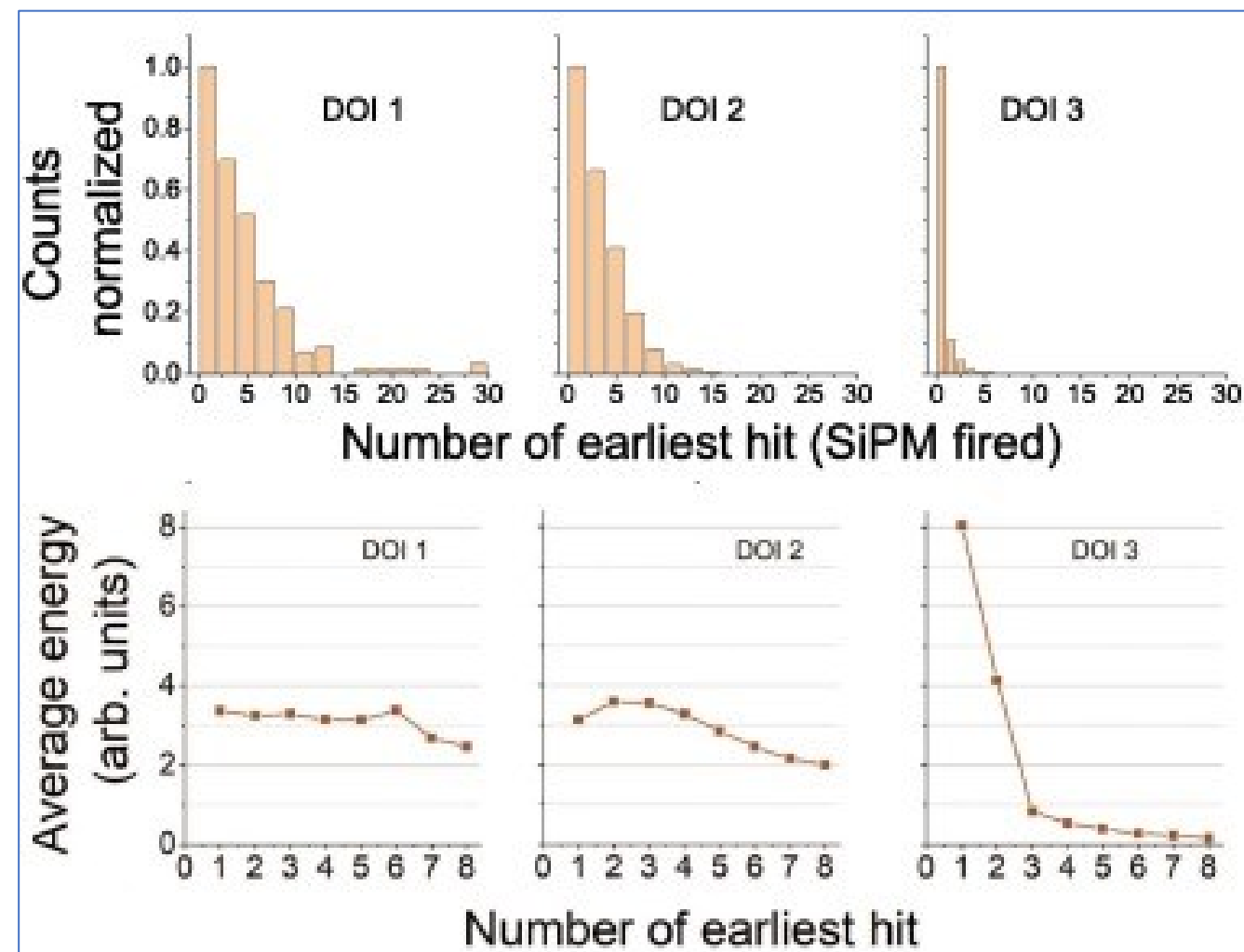


Fig. 5. Top, histograms showing which of hits collected the highest amount of energy for the three DOI regions for the whole [scintillator](#). Bottom, average energy of each hit for all events recorded at the three DOI layers (no filter in position).

3.3. Monolithic detectors, time analysis

When using the monolithic crystal and the reference pixel, the assembly was placed at a stable temperature environment of 7 °C, minimizing dark count rates and increasing the Photon Detection Efficiency (PDE) of the photosensors. Coincidences measurements were carried out with the ^{22}Na source attached to the reference detector and data for the whole scintillator volume were obtained.

We first obtained the timing resolution using the timestamp of the channel with the highest energy, resulting on 1.41 ns FWHM. Alternatively, we sorted the data based on the timestamp and we used the earliest one recorded for the timing distribution. By plotting the difference of the timestamps, we observed an additional satellite peak centered at 5000 ps, see [Fig. 6](#) top. The satellite peak is directly related to the overvoltage of the SiPMs as well as with the value of the `vth_t1` discriminator. Detailed analysis of this effect can be found in [\[28\]](#).

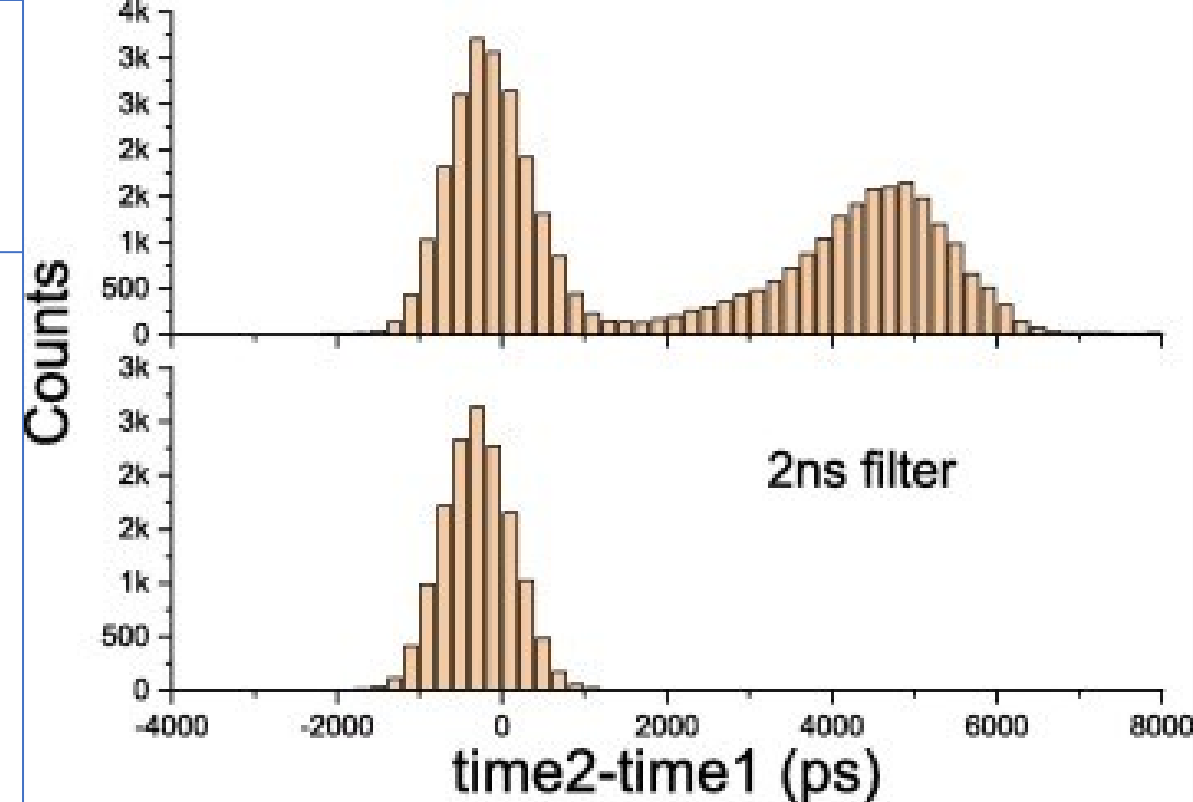


Fig. 6. Top, timing distribution of the measurement between the monolithic block and the reference detector without applying filtering windows. Bottom, timing distribution when applying a 2 ns window for the first six impacts.

Lamprou, E., Gonzalez, A.J., Sanchez, F. and Benlloch, J.M., 2020. [Exploring TOF capabilities of PET detector blocks based on large monolithic crystals and analog SiPMs](#). *Physica Medica*, 70, pp.10-18.

We applied a timing filter window accepting events whose first several hits recorded are within a time frame. In particular six hits were chosen as the optimum number of hits within this window. This filter had as a result an improvement of the CTR and the discard the satellite peak from the timing distribution plots, showing that this effect was a result of false triggering ([Fig. 6 bottom](#)). [Table 1](#) summarizes the measured CTR for different filter timing windows. As it can be seen, narrower time windows significantly improve the CTR but also affect the statistics. Therefore, a window of 2 ns was selected and applied to all following measurements. This filter improved the measured time resolution to 996 ps FWHM

Table 1. Table representing the CTR values as well as the statistics of the total event accepted for different filtering windows of the first 6 hits.

Some authors have showed a significant CTR improvement when instead of the timestamp of the first hit, the timestamps of secondary hits are considered together with a low threshold at the level of the first photo-electron [\[29\]](#), [\[30\]](#). [Fig. 7](#) shows experimentally the same behavior. When using the timestamp of the fourth recorded hit in time, the time resolution was improved. Herein, using this approach and the fourth arrived timestamp, we were able to reach to an improved CTR from 996 ps (RAW data) to 883 ps FWHM.

Filtering Window (ps)	CTR (FWHM, ps)
5000	1156
4000	1133
3000	1100
2000	996
1000	817

Lamprou, E., Gonzalez, A.J., Sanchez, F. and Benlloch, J.M., 2020. [Exploring TOF capabilities of PET detector blocks based on large monolithic crystals and analog SiPMs](#). *Physica Medica*, 70, pp.10-18.

The timing resolution measured for this set-up is still influenced by the time-skew among the ASIC channels. Moreover, the time-walk also affects the CTR due to the poor collection of photons per photosensor element. Thus, a slower rising time is observed as a consequence of the scintillation light sharing effect.

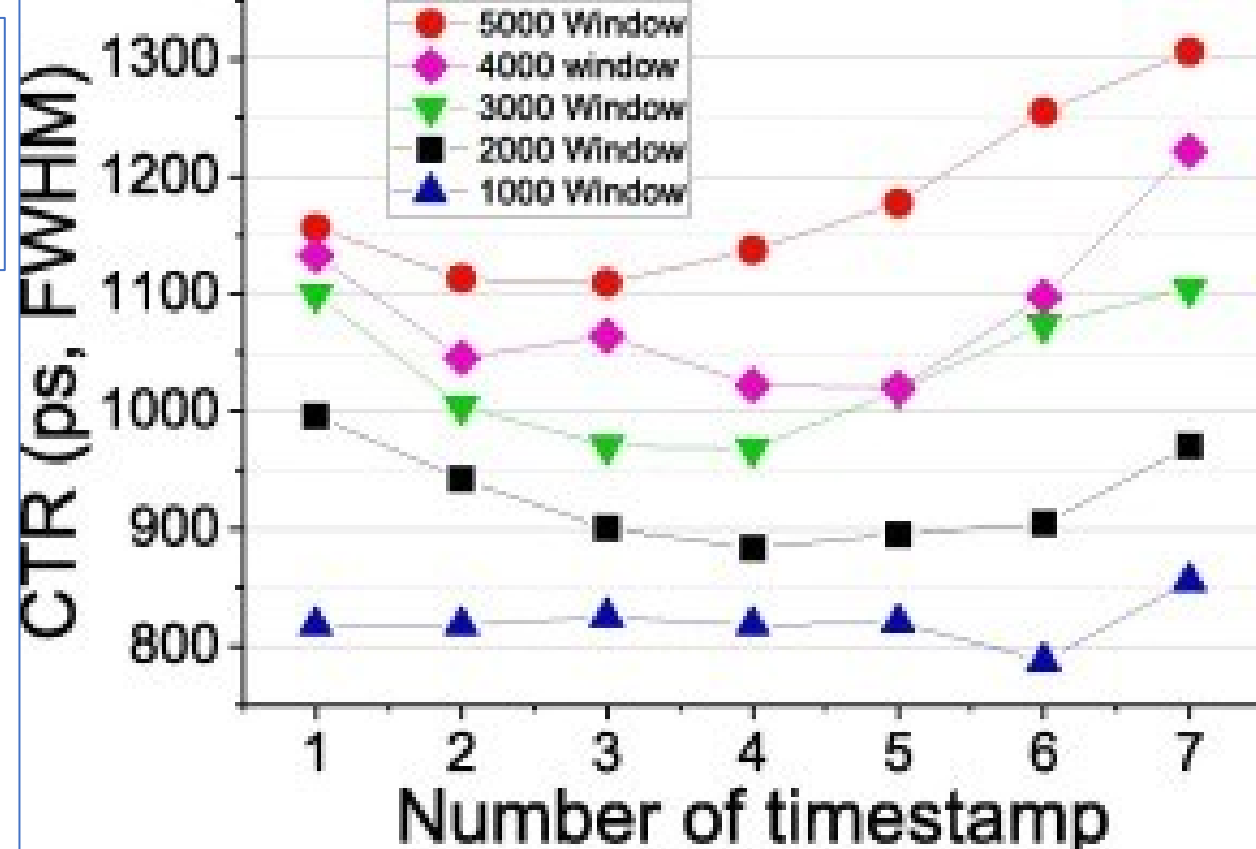


Fig. 7. Experimental results showing CTR measured as a function of the number of earliest timestamp used for different filtering windows.

Some authors have showed a significant CTR improvement when instead of the timestamp of the first hit, the timestamps of secondary hits are considered together with a low threshold at the level of the first photo-electron [\[29\]](#), [\[30\]](#). [Fig. 7](#) shows experimentally the same behavior. When using the timestamp of the fourth recorded hit in time, the time resolution was improved. Herein, using this approach and the fourth arrived timestamp, we were able to reach to an improved CTR from 996 ps (RAW data) to 883 ps FWHM.

We have evaluated the TOFPET2 ASIC showing its capability to achieve sub-200 ps FWHM time resolution using crystal pixels.

A thick and wide monolithic block was selected to be tested and explored in terms of timing resolution. The volume of the selected scintillation block exhibited several challenges in the determination of an accurate impact time resolution. The light sharing effect, and the resulting poor SNR per ASIC channel, is related to the size of the monolithic block. In addition to this, **the selected treatment (black lateral paint and retroreflector layer at the entrance), on one hand enhances the determination of the impact coordinates, but on the other hand significantly degrades the timing resolution due to the scintillation light absorption at the lateral walls**. We are aware these components somehow constrained the achieved performance, and that better absolute values could be obtained using smaller monolithic blocks, with white or reflecting painting, as well as when combined with photosensor arrays with smaller SiPM area. However, the analysis shown in this work is still useful to understand the overall limits and corrections to be applied when using monolithic blocks read out using analog SiPMs and ASICs. We have added especial focus in this work to the time-walk and the time-skew corrections.

The time-skew can be addressed through the independent processing of channel pairs but in the case of the monolithic block, the presence of time-walk uncertainties produces additional difficulties when aiming for an accurate calibration. Nonetheless, the [calibration method](#) described in this work provides good results. The time-skew was successfully corrected, permitting the exploitation of the timing information during future reconstruction processes. In addition, the time-walk has also been partially compensated, a fact that permits and motivates a follow up research work towards the development of TOF-PET detectors using other types and treatments of monolithic blocks.

Lamprou, E., Gonzalez, A.J., Sanchez, F. and Benlloch, J.M., 2020. [Exploring TOF capabilities of PET detector blocks based on large monolithic crystals and analog SiPMs](#). *Physica Medica*, 70, pp.10-18.

Summarizing, RAW timing resolutions were found to be well above 1 ns for a large $50 \times 50 \times 15$ mm³ LYSO block when tested in coincidence against a reference pixel-based detector. Techniques to discard a fraction of noisy events and decrease the time uncertainty were applied, reaching a significant improvement in terms of CTR of 550 ps FWHM for the whole scintillation volume, without subtracting the reference detector contribution which is estimated at 230 ps FWHM. As shown in the analysis of the CTR and event position dependency, an improved timing resolution can be achieved for events at the center of the crystal and deep [DOIs](#) layers of 440 ps FWHM (again without subtracting the reference detector contribution). When two identical detectors were tested, CTR values of 660 ps FWHM were found. This timing resolution clearly cannot permit the use of timing information in the lines of response for small or organ dedicated systems [31], but will permit the reduction of noise as well as the improvement of the SNR in the reconstructed images. Moreover, recent pilot studies in our lab have shown to improve these results up to a factor of 2 if smaller crystals (1×1 in.), [Teflon](#) wrapped, and coupled to 8×8 SiPM arrays (3×3 mm²) are used.

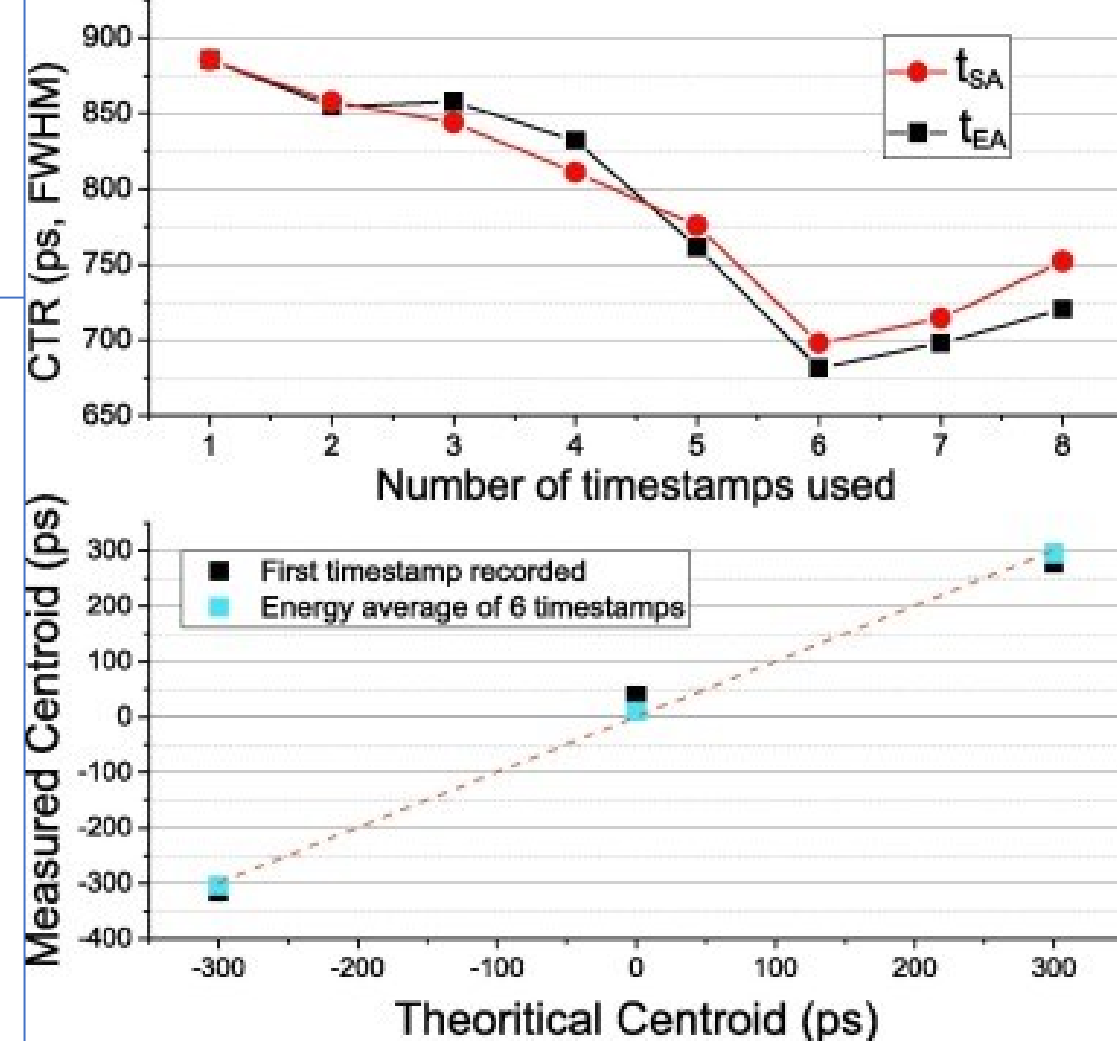


Fig. 12. Top, timing resolution of the coincidence measurement between the two monolithic detectors using simple timestamps average (red circles) and energy weighted timestamps average (black squares).

Shin, S., Aviles, M., Clarke, S., Cwik, S., Foley, M., Hamel, C., Lyashenko, A., Mensah, D., Minot, M., Popecki, M. and Stochaj, M., 2022. Advances in the Large Area Picosecond Photo-Detector (LAPPD): 8" x 8" MCP-PMT with Capacitively Coupled Readout. arXiv preprint arXiv:2212.03208.

3.1 High QE Photocathode Characterization

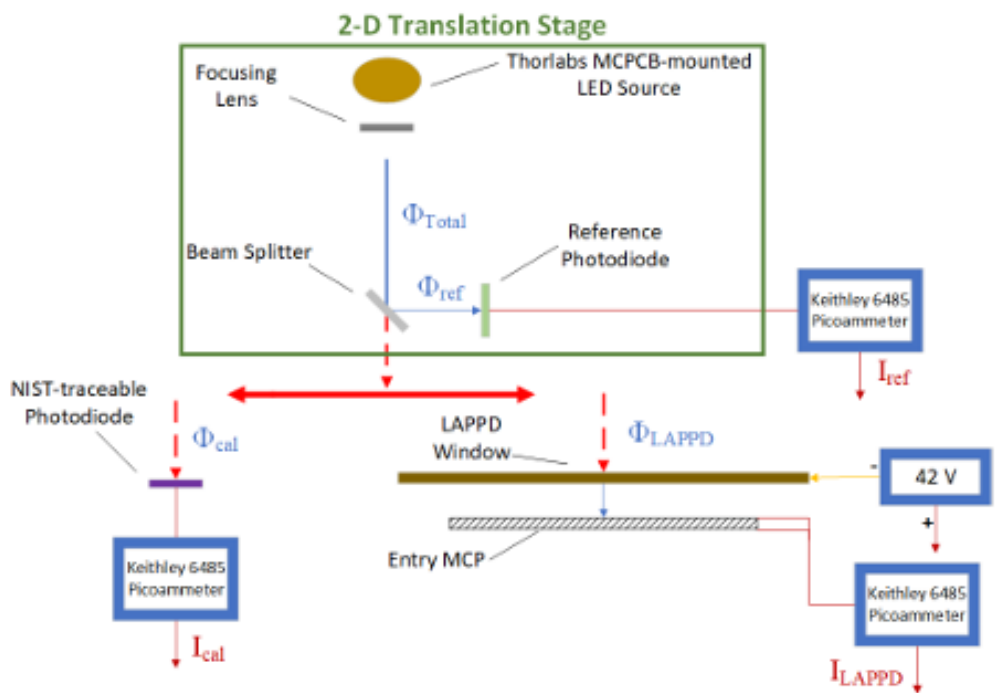


Figure 4: QE measurement setup in the dark box shown in Figure 3. The LED source, beam splitter, and reference photodiode can translate laterally between the NIST-traceable photodiode and the LAPPD window. A similar setup shown in Figure 5, without the 2-D translation stage, is used to test the spectral response of an LAPPD.

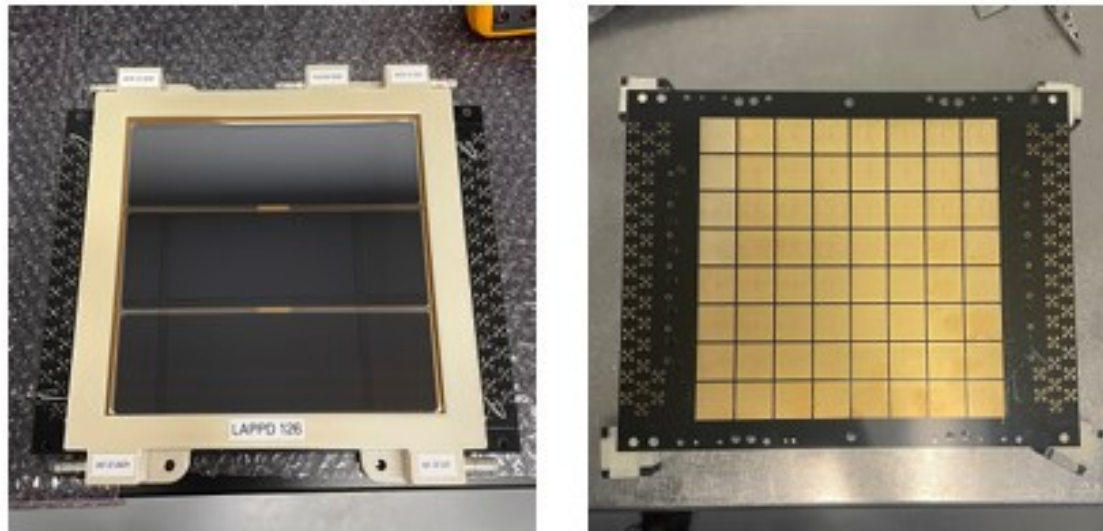
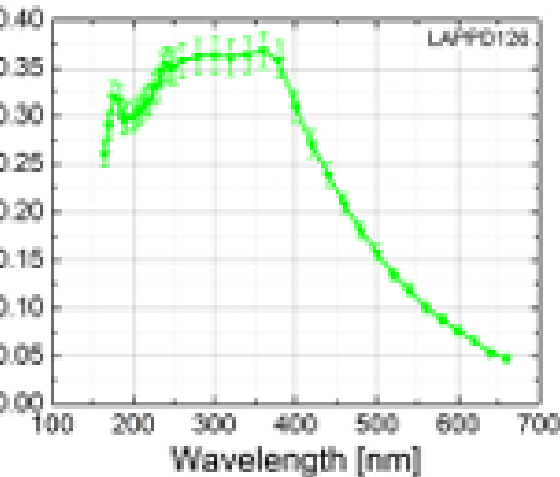


Figure 1: LAPPD126 in Ultem housing with independent high voltage connections labeled accordingly (left). Newly designed internal stack components (Rib-spacers) open up the central area of the LAPPD for active detection. 8 × 8 pixelated readout board with 25 mm pitch pixels that capacitively couple to the internal resistive anode of the LAPPD (right)

QE as a function of wavelength measured for LAPPD126



Maebe, J., and Vandenberghe, S. (2023). [Effect of detector geometry and surface finish on Cerenkov based time estimation in monolithic BGO detectors](#). Physics in Medicine & Biology, 68(2), p.025009...

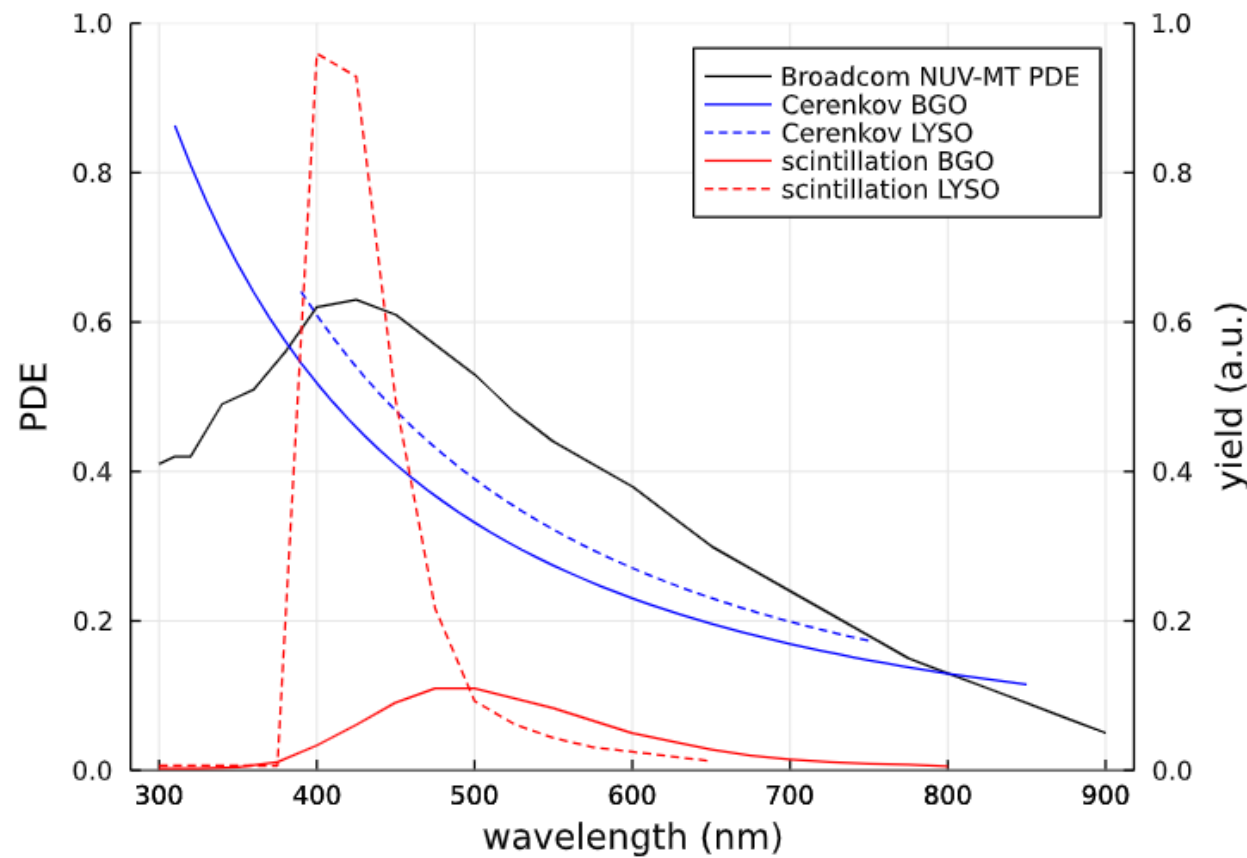
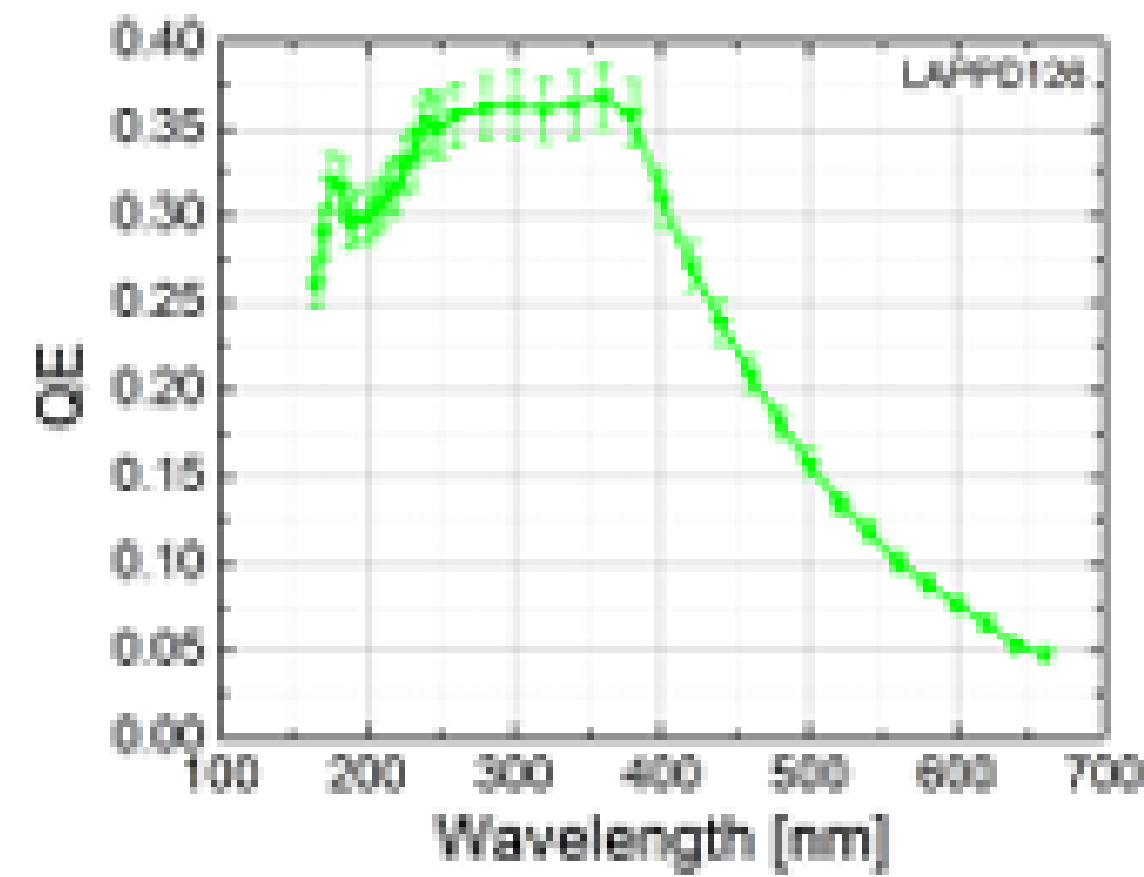


Figure 2: Photon detection efficiency (PDE) wavelength dependency of Broadcom NUV-MT SiPMs and Cerenkov/scintillation spectra of BGO and LYSO.

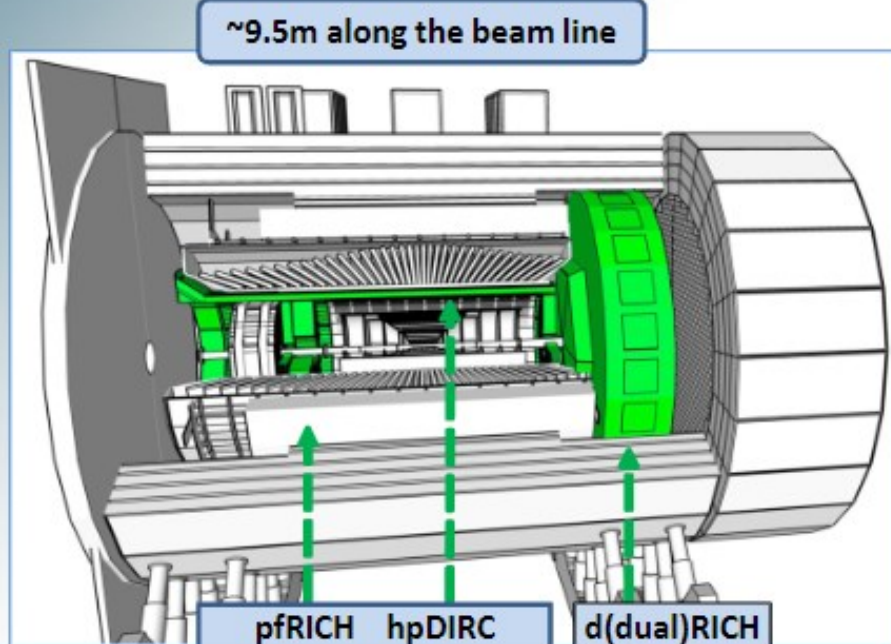


Shin, S., Aviles, M., Clarke, S., Cwik, S., Foley, M., Hamel, C., Lyashenko, A., Mensah, D., Minot, M., Popecki, M. and Stochaj, M., 2022. [Advances in the Large Area Picosecond Photo-Detector \(LAPPD\): 8" x 8" MCP-PMT with Capacitively Coupled Readout](#). arXiv preprint arXiv:2212.03208.

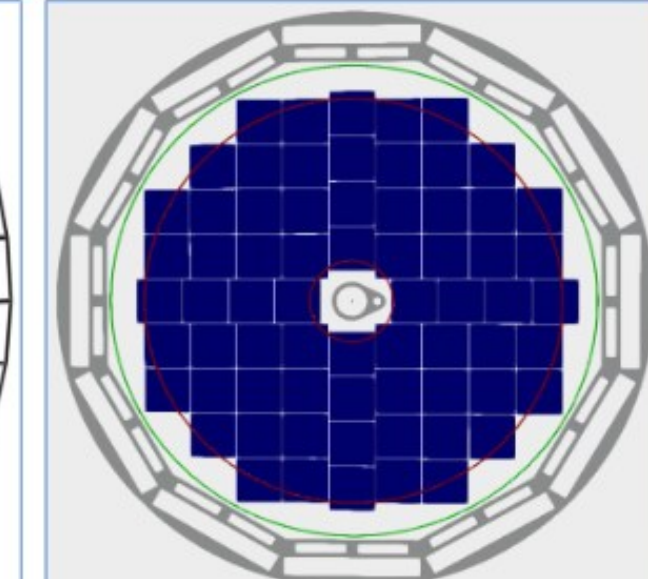
HRPPD applications for the EIC (courtesy of A.Y. Kiselev)

HRPPD benefits:

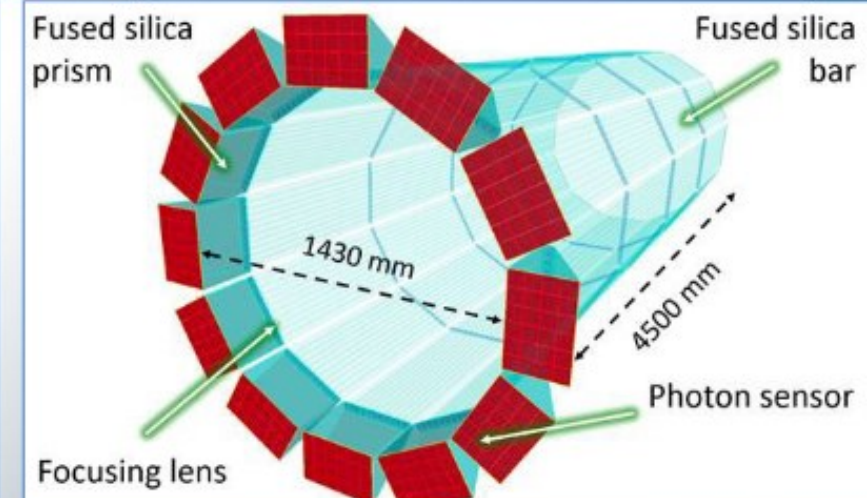
- pfRICH: low dark noise, ToF capability (vs SiPMs)
- hpDIRC: expected to be more cost-efficient (vs other MCP-PMTs)
- dRICH: problematic, because of the magnetic field orientation
- HRPPDs can supply up to (68 plus 72 for total of 140+ tiles + spares)



pfRICH = (proximity focusing)
Ring Imaging Cherenkov



hpDIRC = (high performance)
Detector of Internally Reflected Cherenkov

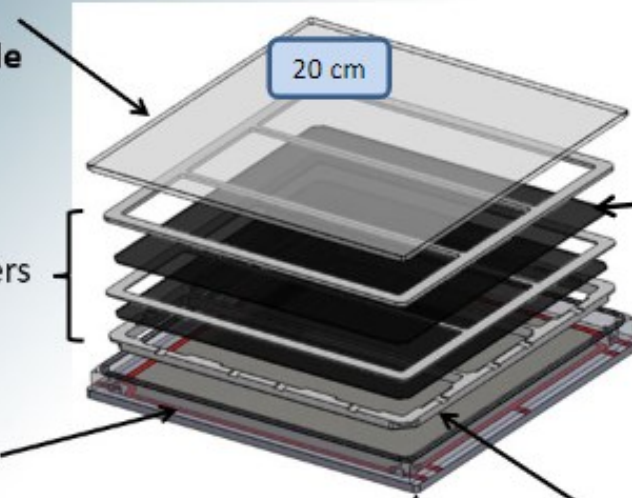


hpDIRC: 12 arrays of 3x2 devices
= 72 HRPPDs total

ALD-MCP-PMT Device design – How do they work?

Fused Silica window
(Photocathode inside)

LAPPD - Large Area Picosecond Photo Detector

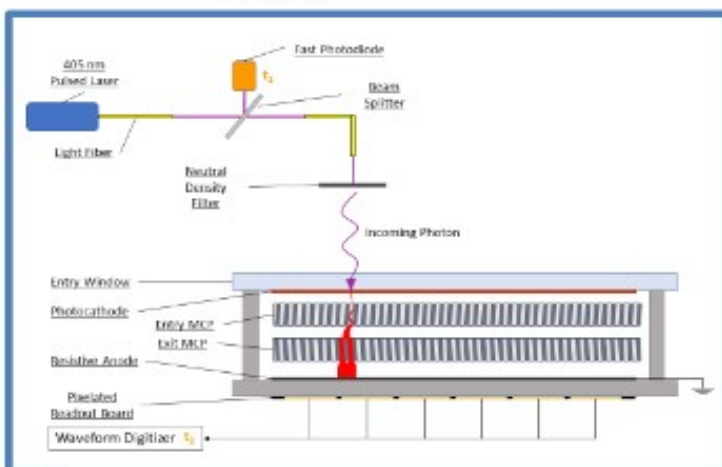


MCPs + Spacers

Sidewall frit bonded to Anode plate

HV tabs at each corner
(Independently power MCPs)

- No wall or anode penetrations
- Active area: 195 mm x 195 mm
 - 373 cm² (97%)



HRPPD - High Rate Picosecond Photo Detector

UV Grade Fused Silica Window

B33 Bottom Spacer

Alumina Sidewall

Directly coupled (DC) Anode

INC

10 cm

DC = Direct Coupled

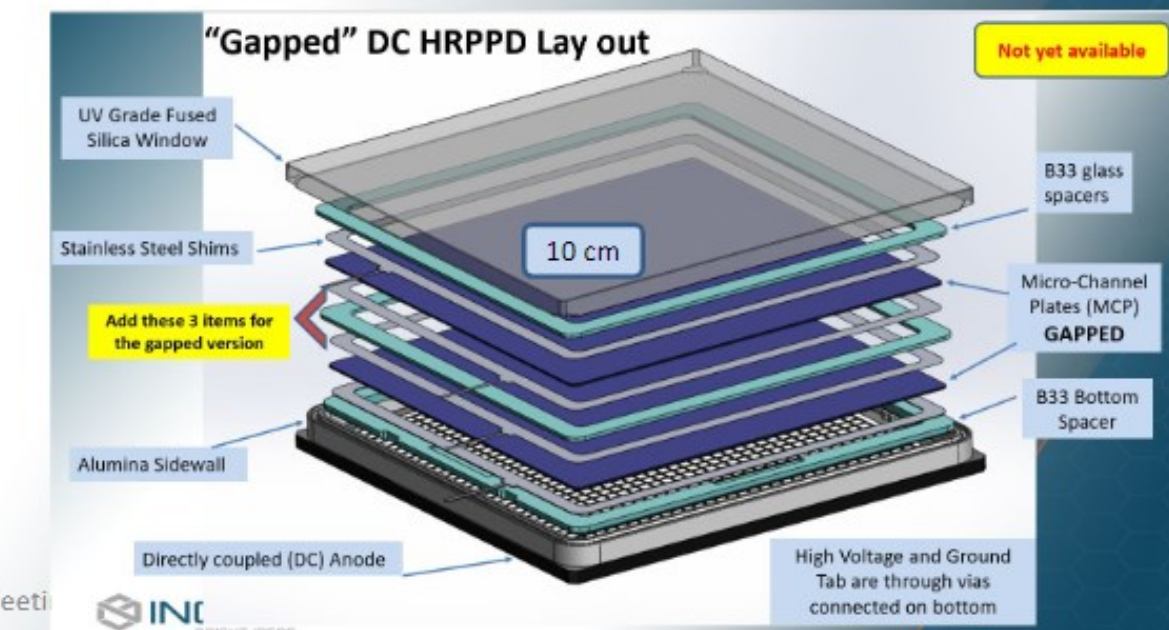
HRPPD Lay out

B33 glass spacers

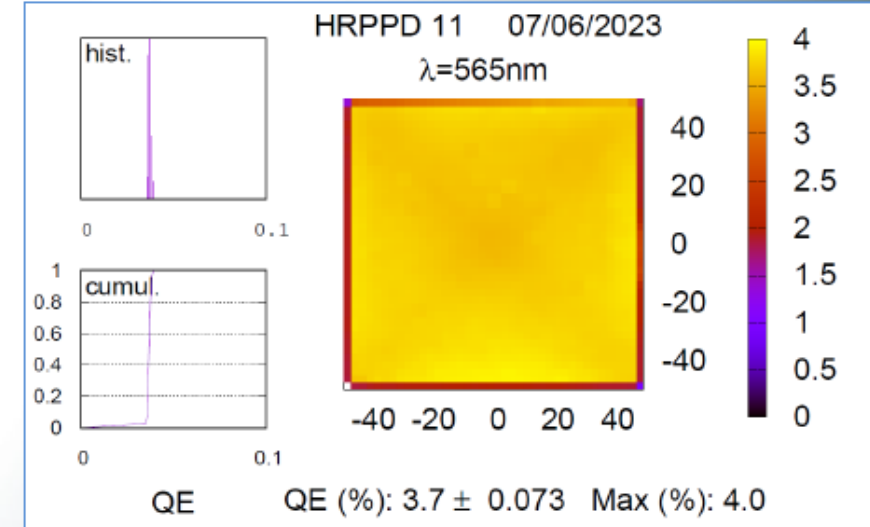
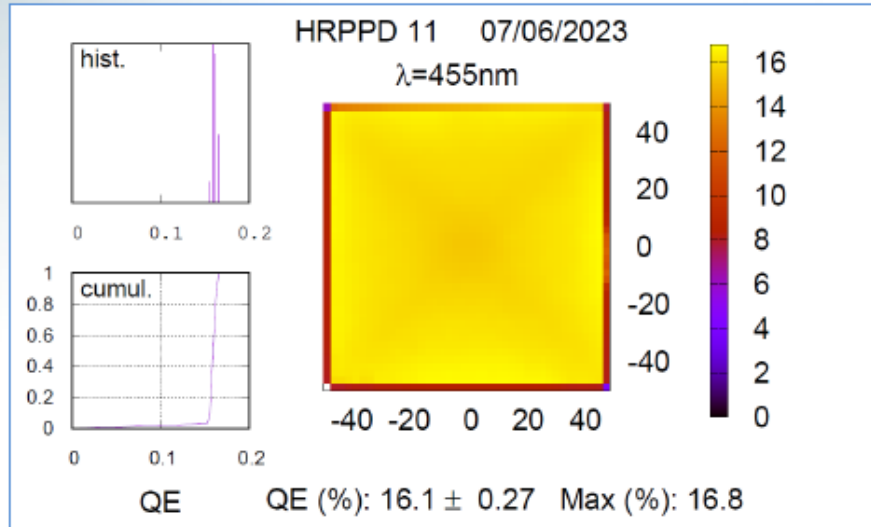
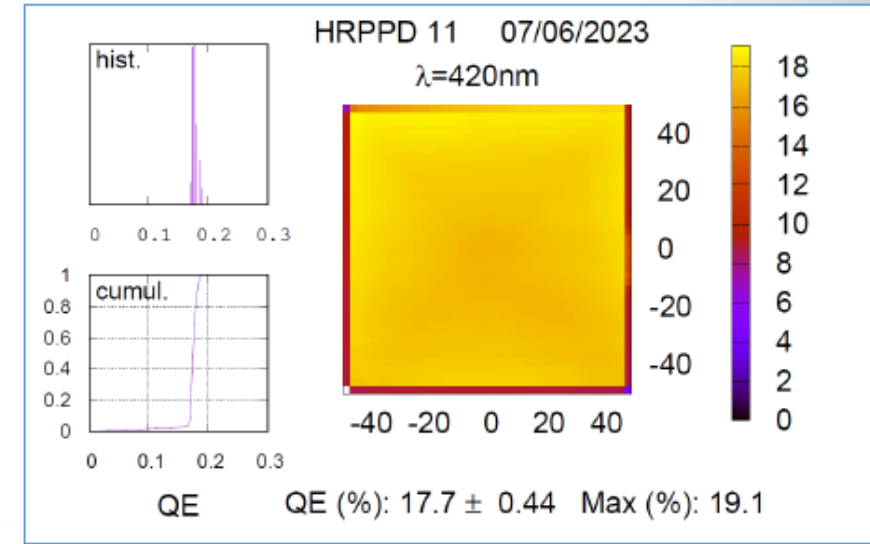
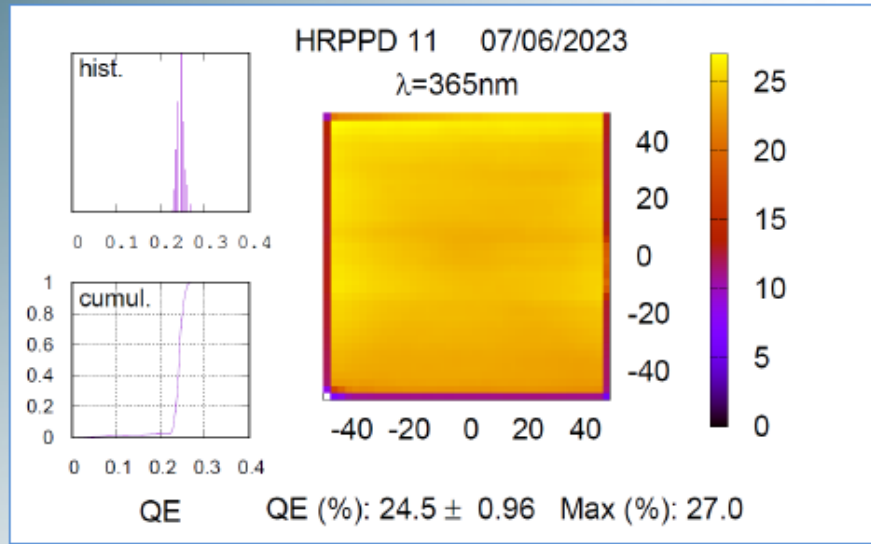
Micro-Channel Plates (MCP)
STACKED

Stainless Steel Shims

High Voltage and Ground Tab are through vias connected on bottom



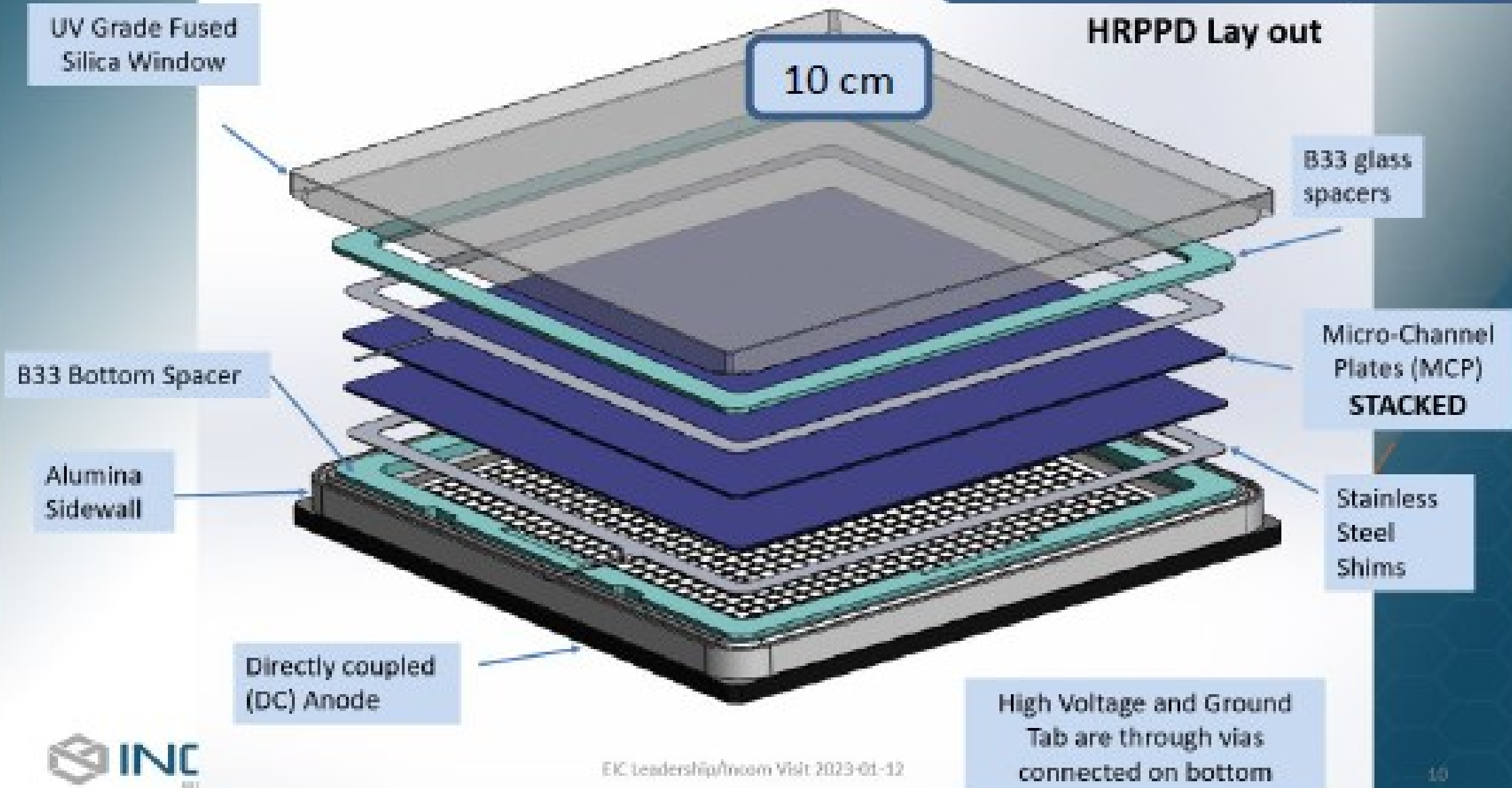
HRPPD 11 QE Scans



HRPPD - High Rate Picosecond Photo Detector

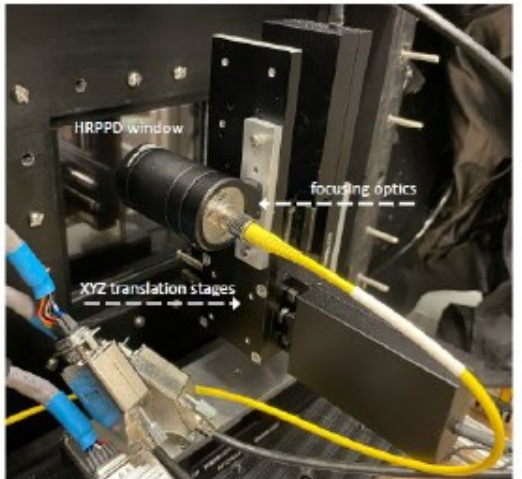
DC = Direct Coupled

HRPPD Lay out

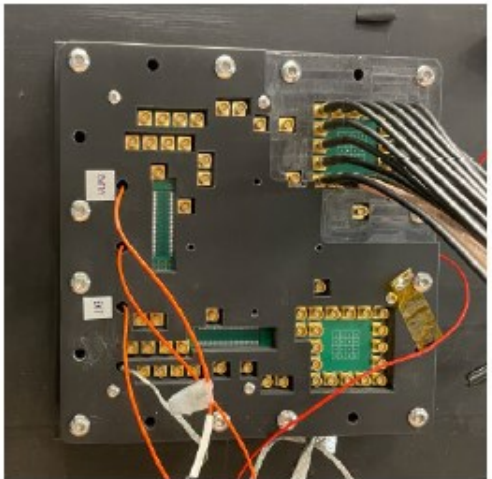




HRPPD 6



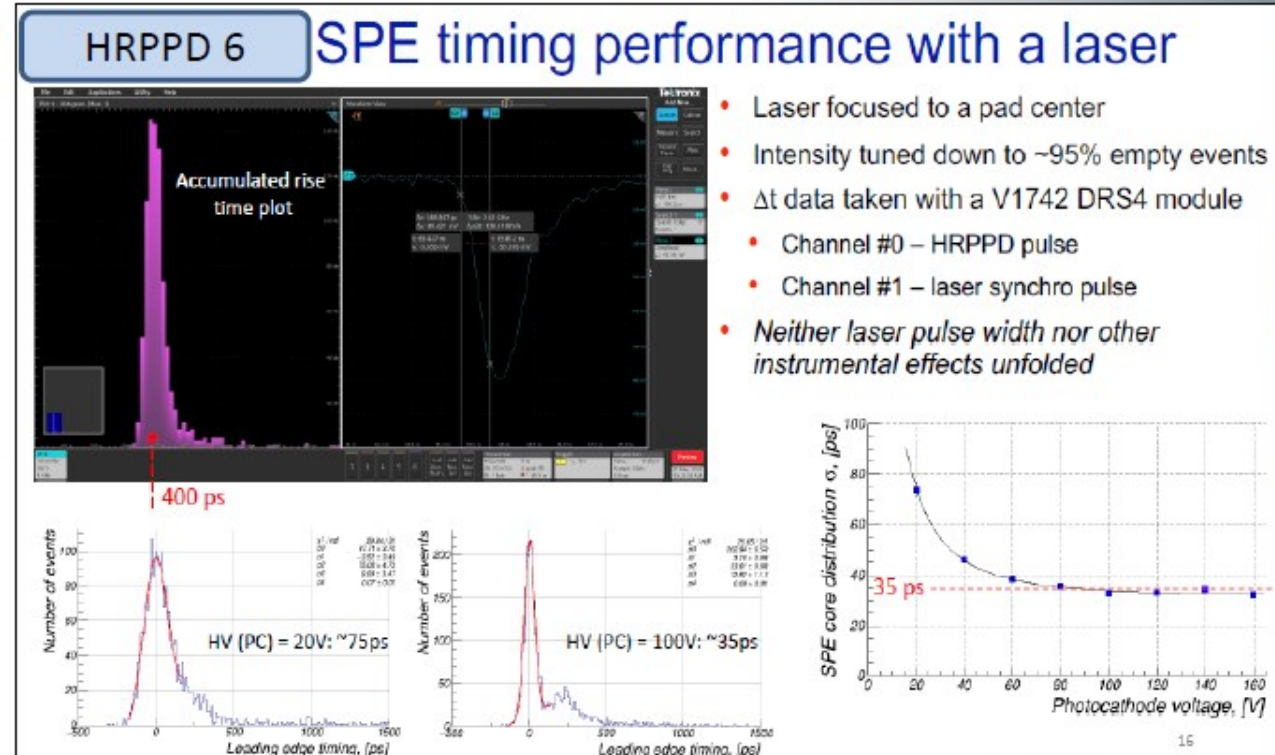
Light tight enclosure

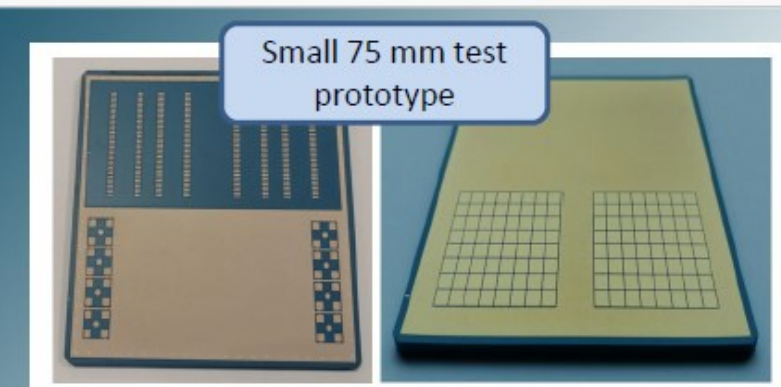


Pogo pin interface board side

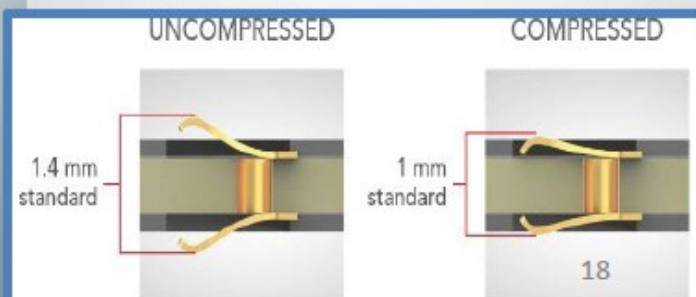
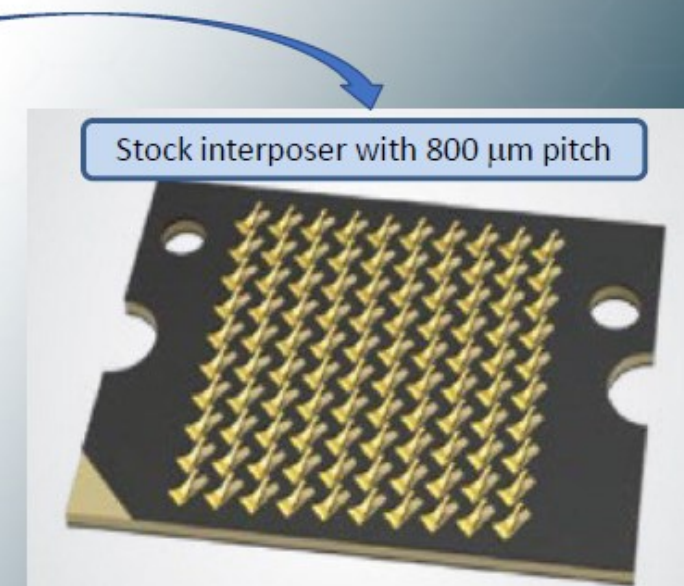
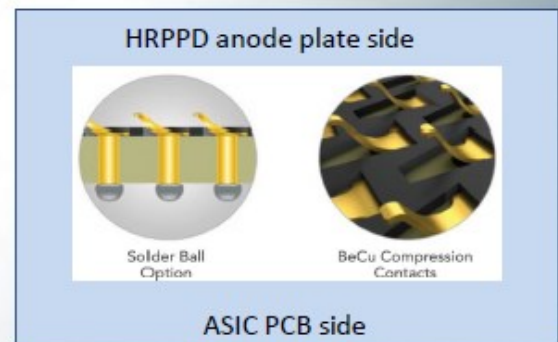
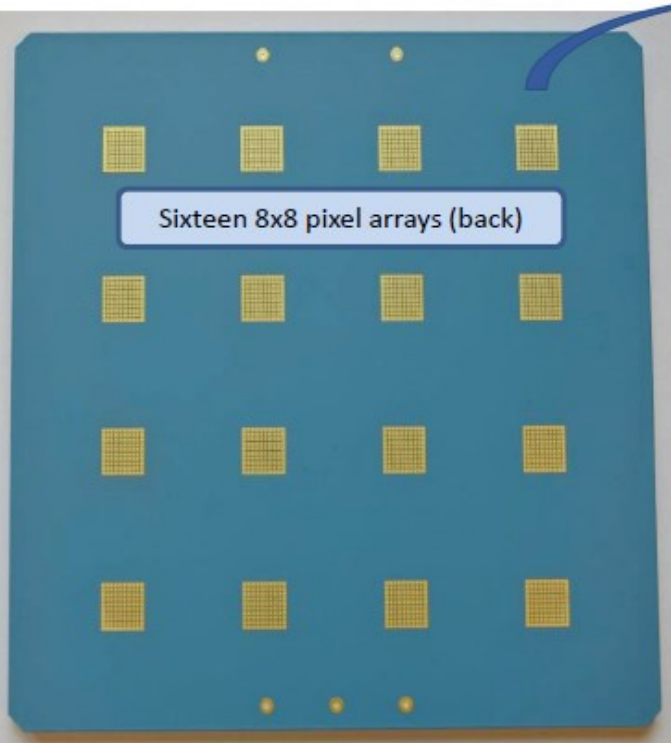
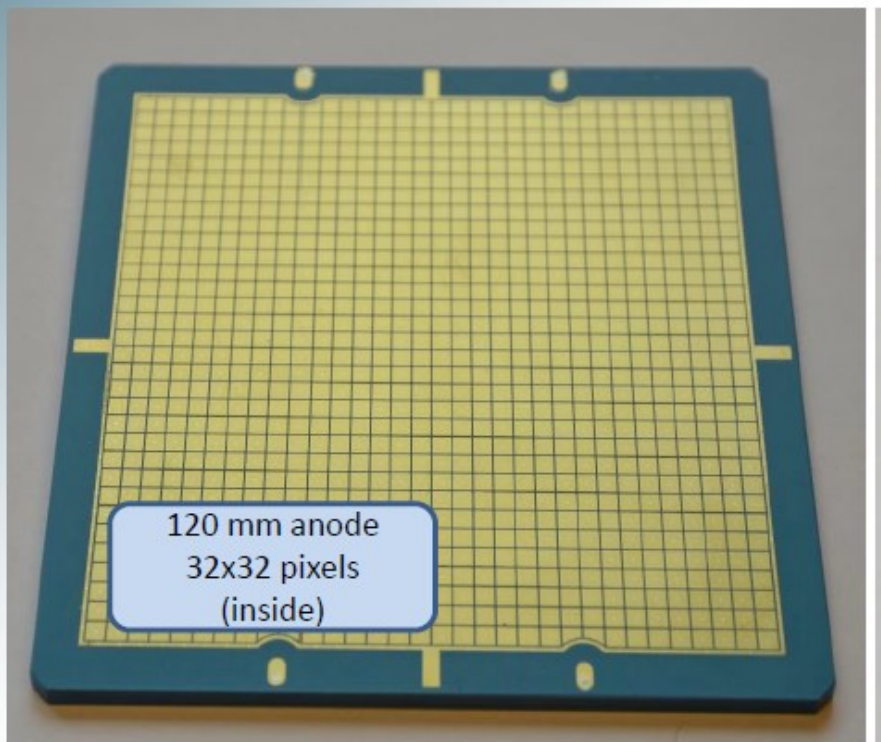
Testing @ Brookhaven National Laboratory

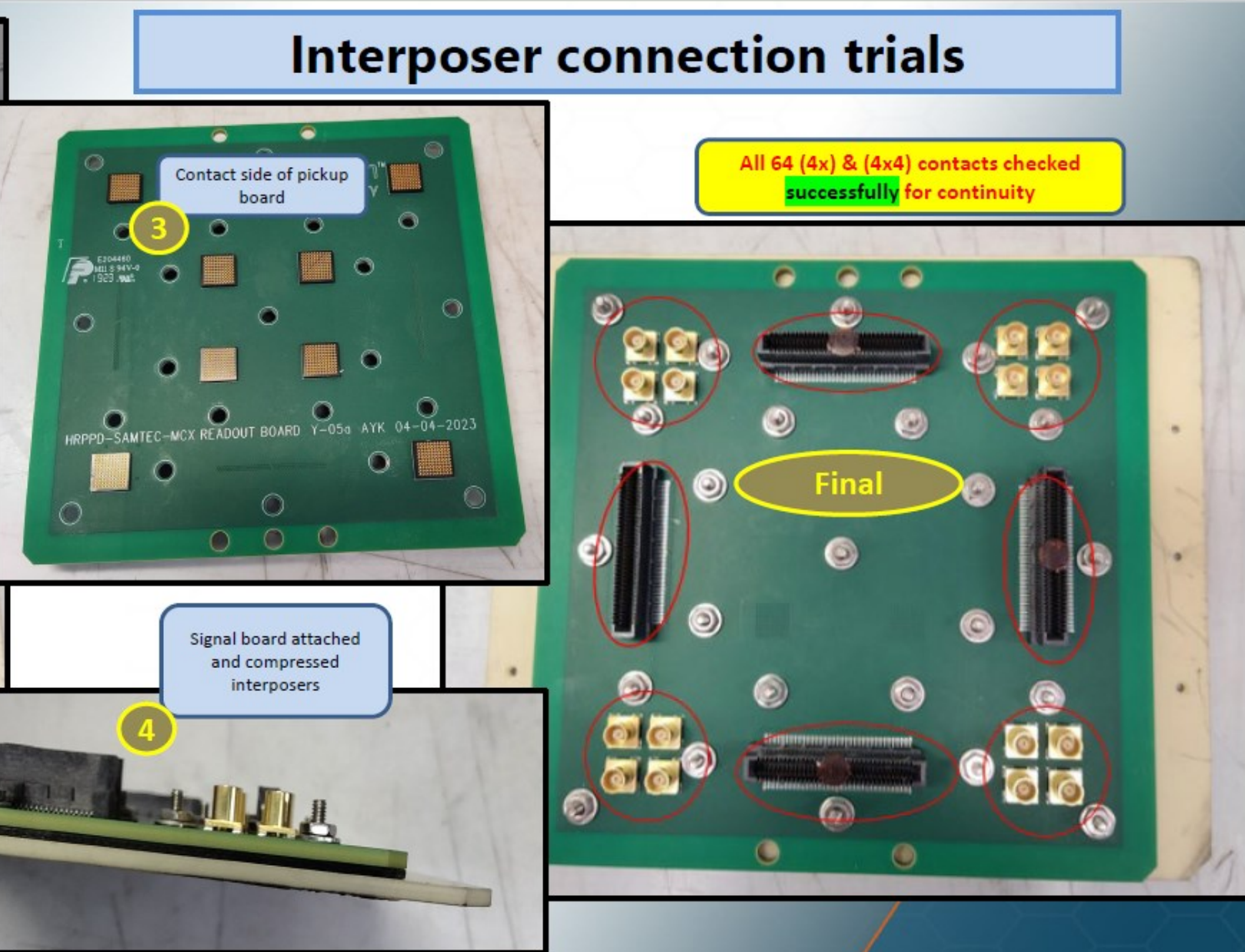
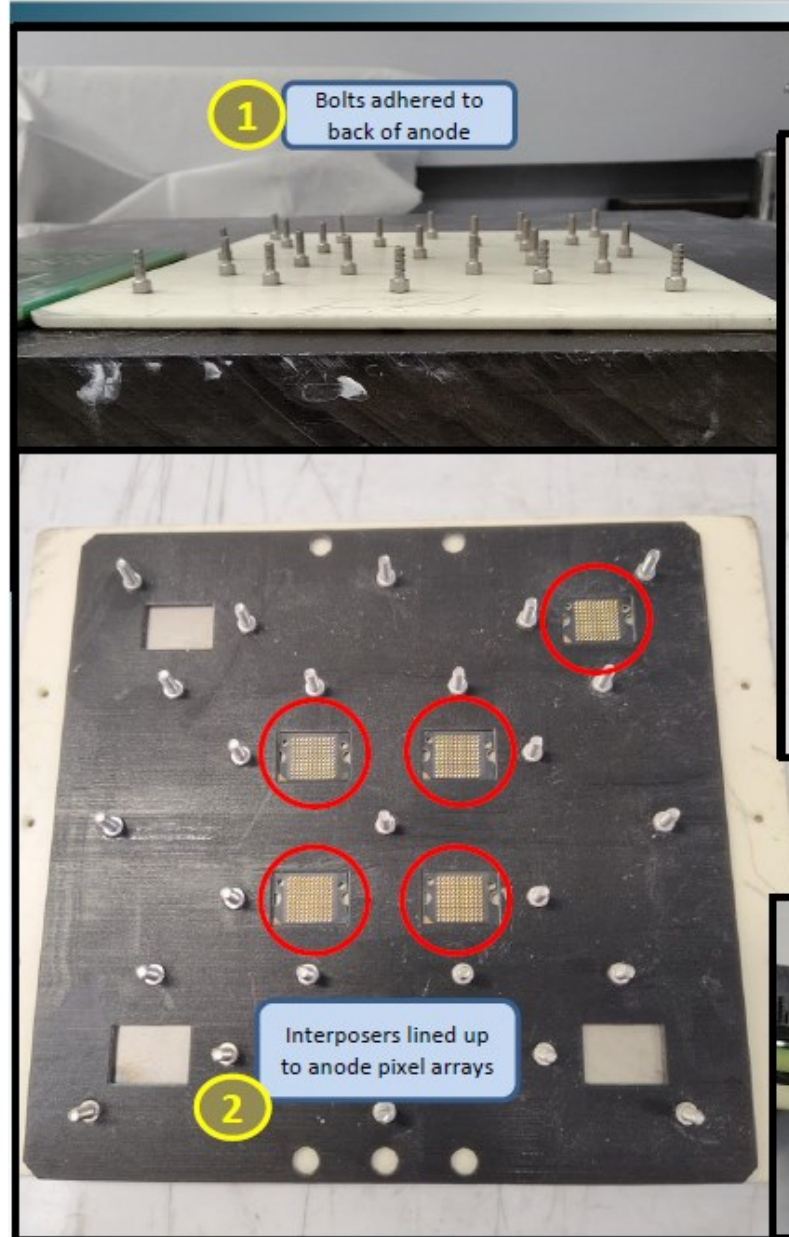
(courtesy of A. Y. Kiselev)





First iteration: (Vendor 2) anode base plate





(1) The reflective and semi-transparent CsI photoemission theory, we have shown that films thinner than the electron escape length are characterized by a higher quantum efficiency with respect to thin films operating only in semitransparent mode, or thick films operating in reflective mode.

(2) Photocathode CsI on optical input window substrates only operate in STM; but on MCP substrates can operate in both STM and RFM, in contrast, quantum efficiency of RFM is higher than STM.

(3) The thickness of CsI layers is adequate to one MCP model, it depend on the shape and size of MCP channel.

C. Lu, K.T. McDonald / Nucl. Instr. and Meth. in Phys. Res. A 343 (1994) 135–151

137

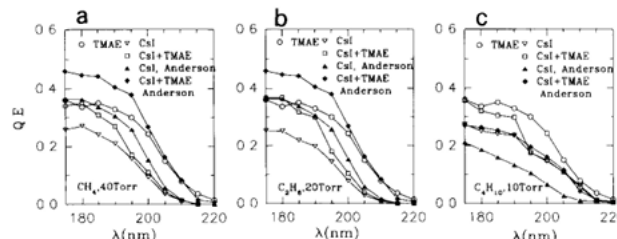


Fig. 3. The quantum efficiency of CsI (a) in CH_4 , (b) in C_2H_6 , and (c) in C_4H_{10} . Also shown are data points from Anderson et al. [14].

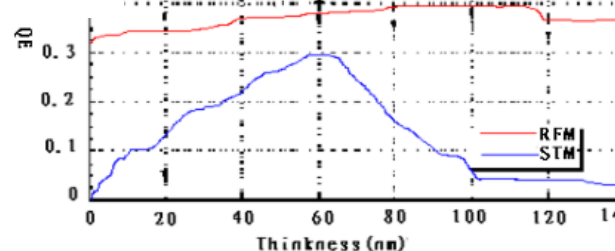


Fig. 2. The quantum efficiency variation with CsI film thickness

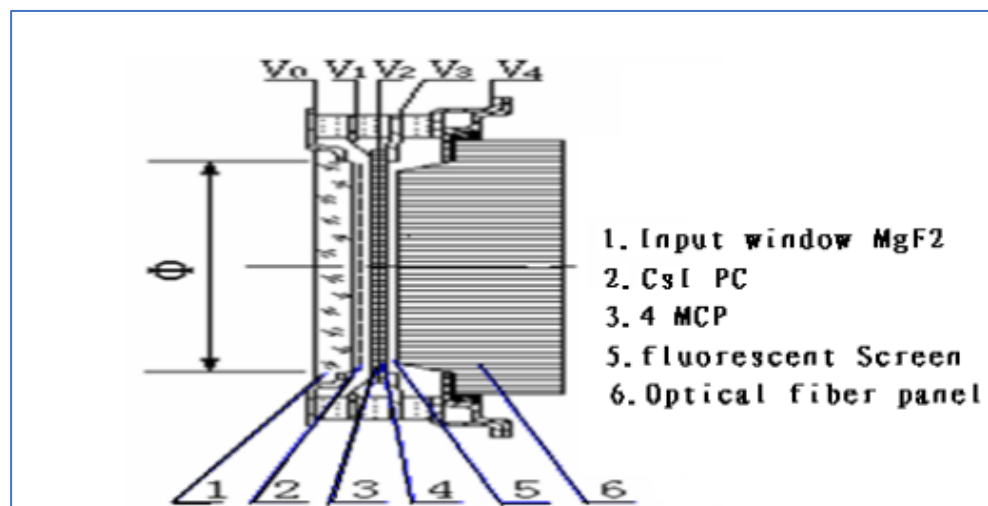


Fig. 1. Structure schematic diagram of double proximity focusing image intensifier tube

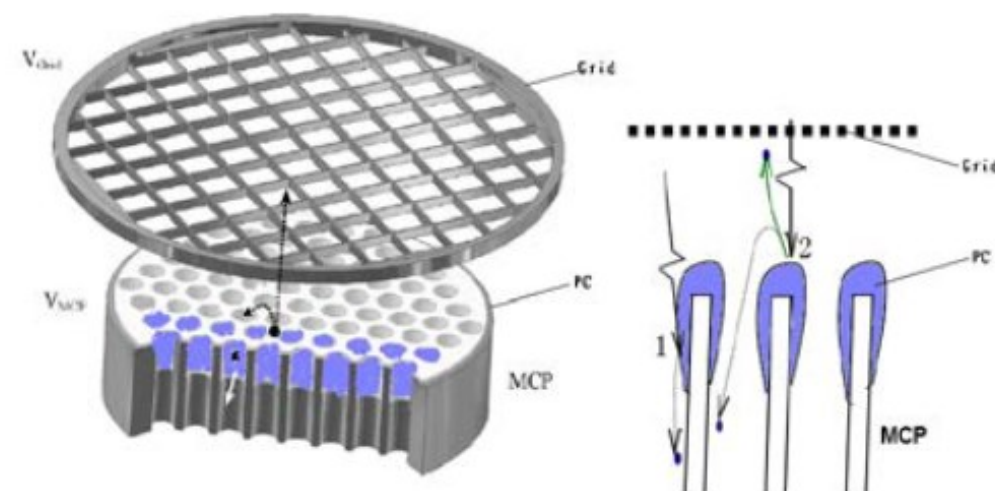
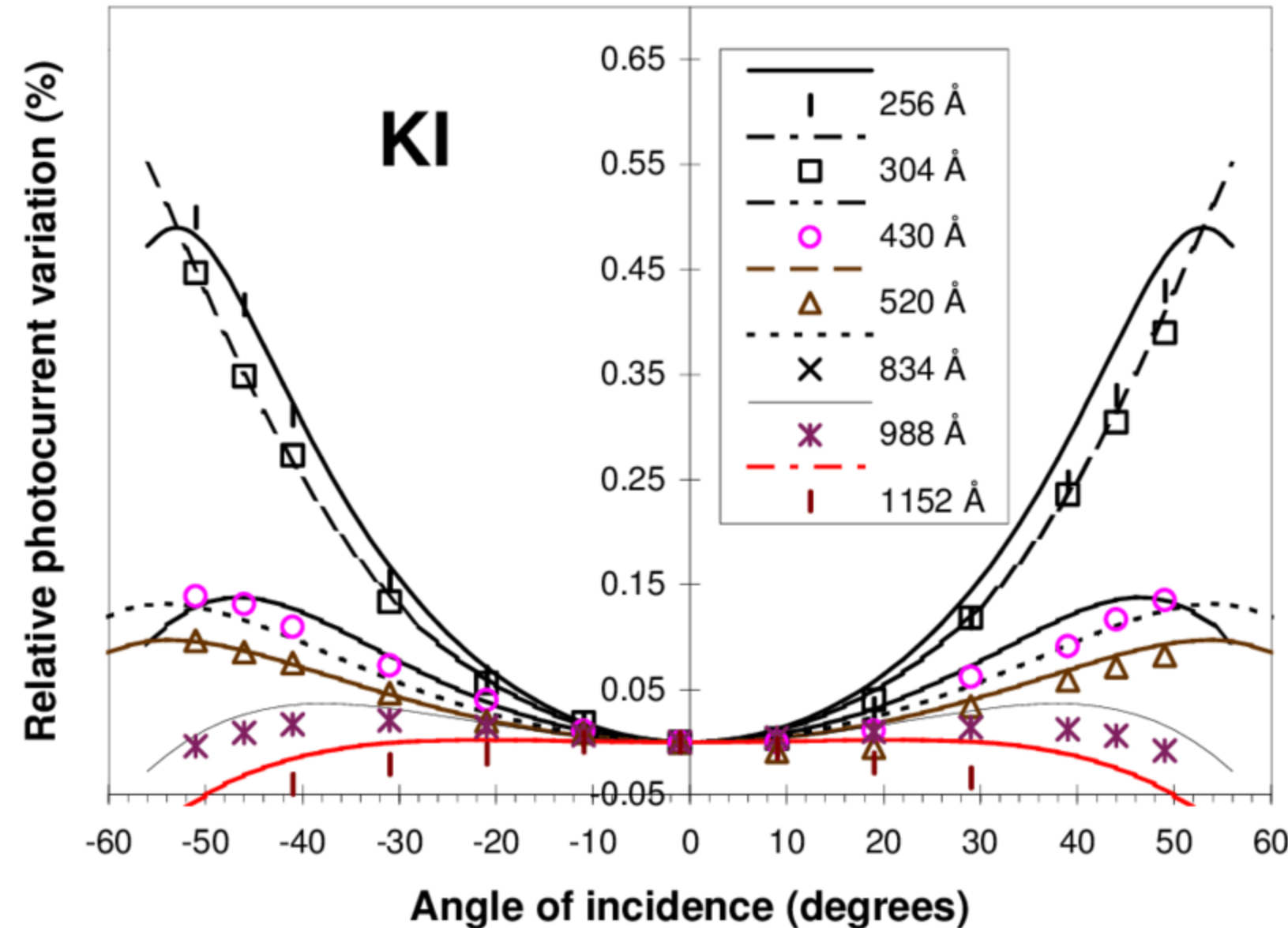
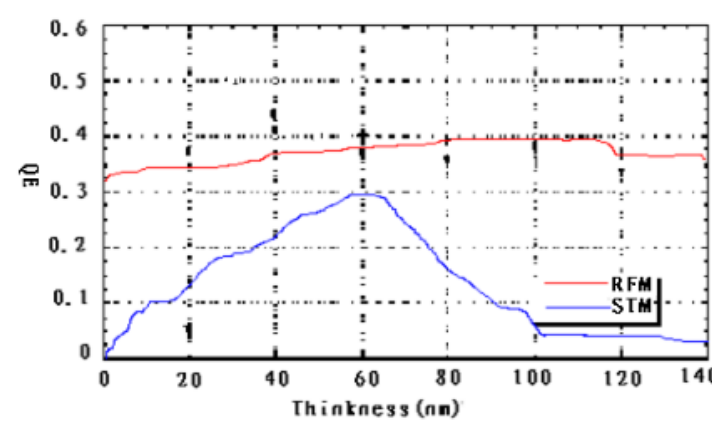
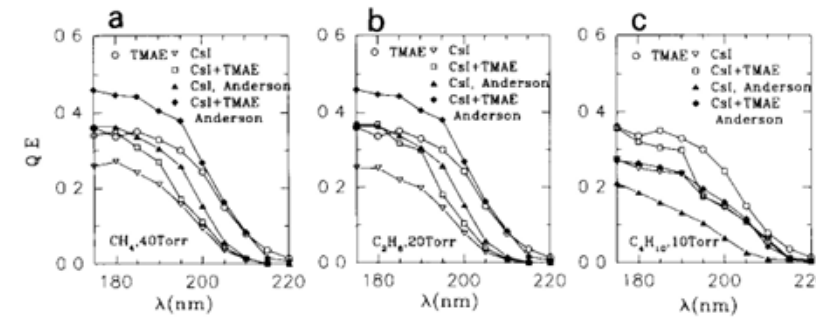


Fig. 3. The Schematic of photoelectron transmission on MCP substrates

Tremsin, A.S. and Siegmund, O.H., 1999, October. Dependence of quantum efficiency of alkali halide photocathodes on the radiation incidence angle. In *EUV, X-Ray, and Gamma-Ray Instrumentation for Astronomy X* (Vol. 3765, pp. 441-451). SPIE.

C. Lu, K.T. McDonald / Nucl. Instr. and Meth. in Phys. Res. A 343 (1994) 135–151



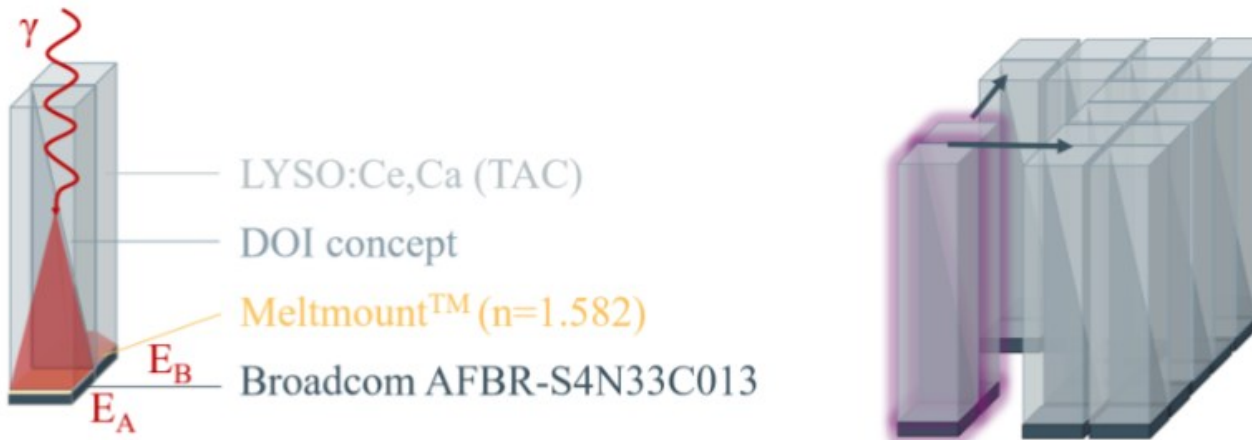


Fig. 2. Design concept of the investigated TOF-DOI detector units. A unit consists of two analog SiPMs coupled to two LYSO:Ce,Ca crystals (left), which can be scaled to any desired matrix geometry, e.g., a four-by-four pixel matrix (right).

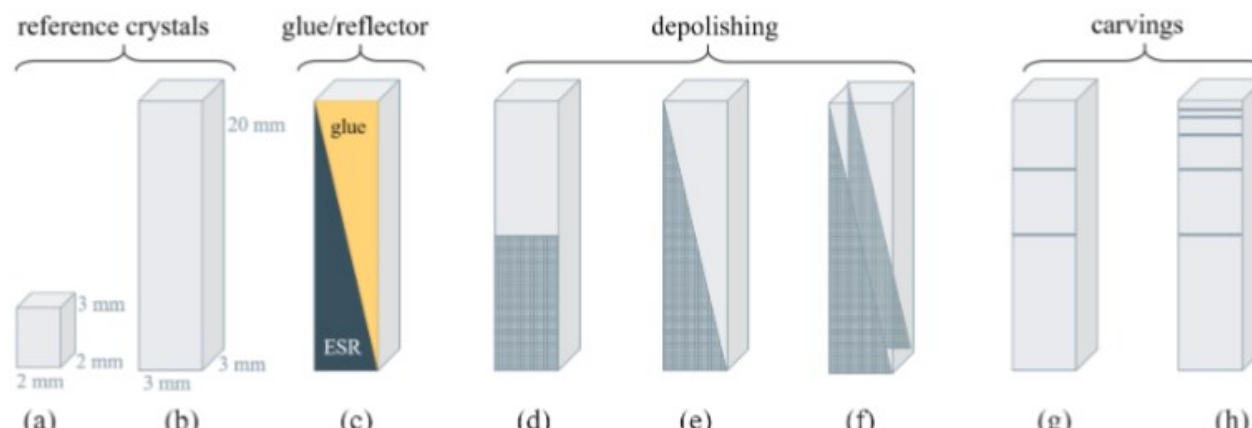


Fig. 3. Schematic drawing of the different DOI concepts investigated in this study. All crystal pixels were cut out of LYSO:Ce,Ca ingots and manufactured at Taiwan Applied Crystal Co. Ltd. In addition to reference crystals with sizes $2 \times 2 \times 3 \text{ mm}^3$ (a) and $3 \times 3 \times 20 \text{ mm}^3$ (b) and reflectors and glue layers mounted by the authors (c). The manufacturer realized the depolished rectangular (d) and triangular (e) and (f) crystal faces and carvings at different heights and of 1-mm depth (g) and (h).

Scintillation and cherenkov photon counting detectors with analog silicon photomultipliers for TOF-PET. Physics in Medicine & Biology, 69(4), p.045025.

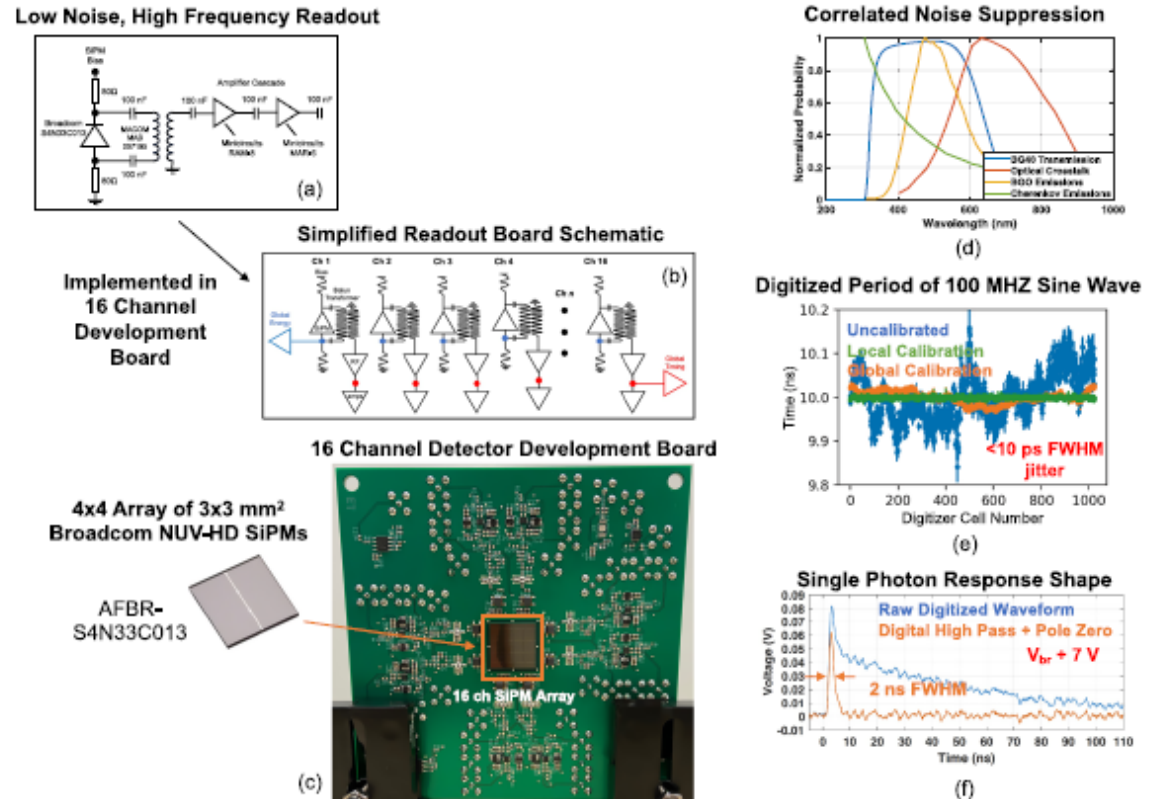


Figure 2. Key aspects of a prototype demonstration setup for a scintillation photon counting detector concept are shown. In (a), a simplified, single channel schematic is shown for a sixteen-channel prototype detector readout board. A simplified schematic of the prototype readout board is shown in (b), including multiplexed channels for data acquisition triggering. The sixteen-channel electronics board is shown in (c). Transmission plot for a Schott BG40 optical glass filter used for dramatically reducing external crosstalk from the SiPM array is shown in (d), along with the BGO, Cherenkov, and optical crosstalk emissions spectra. Each channel of data acquisition was custom calibrated to optimize digitization accuracy and intrinsic jitter of the experimental setup. In (e), the measured period of a 100 MHz sine wave, randomly phased between cells of a DRS4 chip channel is shown without and with calibrations applied. When calibrations are applied, the period is accurately quantified to <10 ps FWHM accuracy across the entire 200 ns time range. A measured single photon pulse from the prototype setup is shown in (f) with and without digital shaping applied (high pass filter with pole-zero compensation), achieving 2 ns FWHM pulse width.

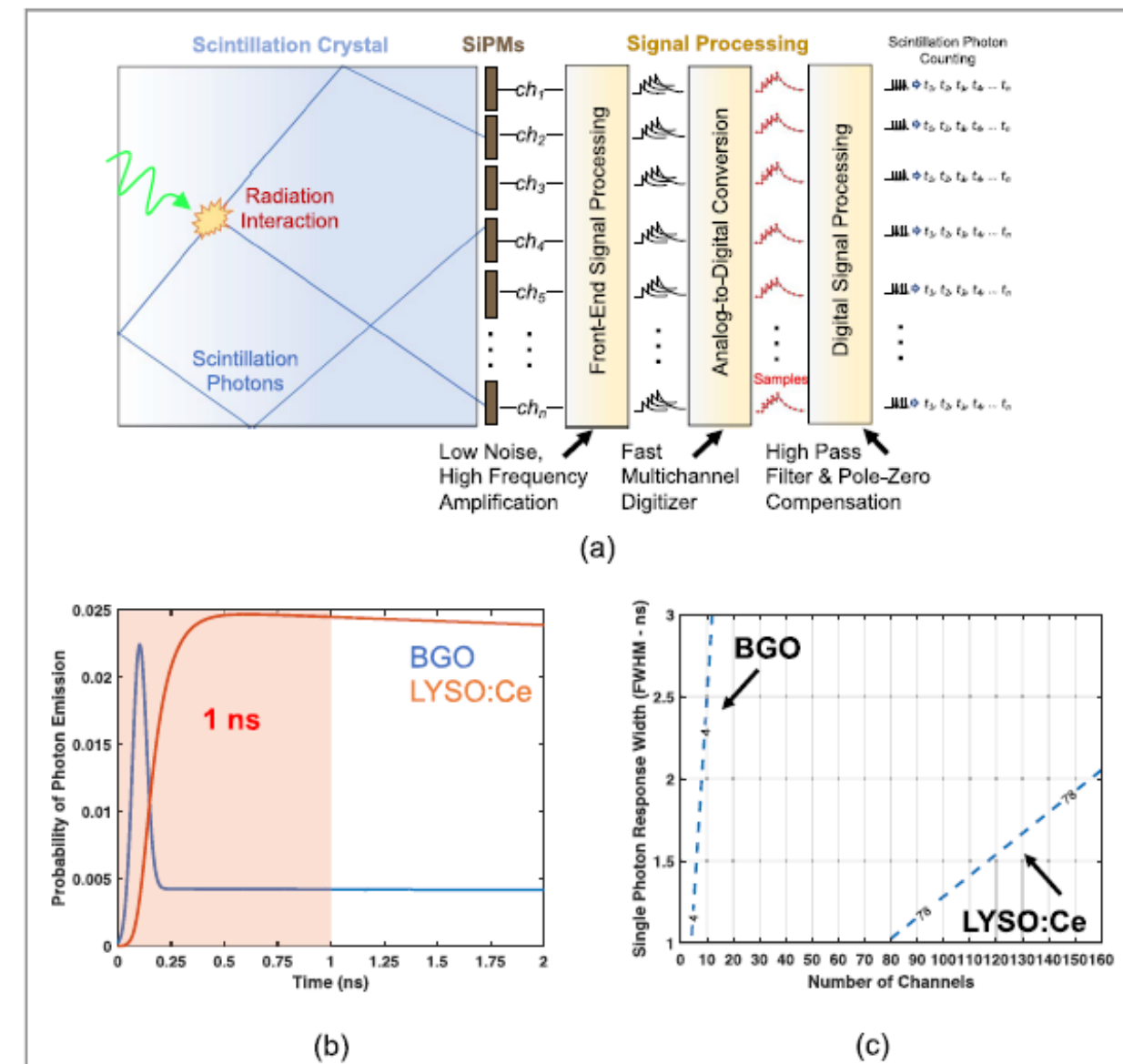


Figure 1. An illustration of a detector concept for counting photons from a scintillation detector with analog SiPMs is shown in (a). In (b), photon detection time profiles for BGO and LYSO:Ce scintillators are shown, highlighting that the highest temporal emission density occurs within the first nanosecond of excitation. An approximate calculation of single photon response shape width and number of channels required to count scintillation photons for BGO and LYSO:Ce with the detector concept (a) is shown in (c).